

**Investigation of the
Mountain River Beryl (Emerald Variety) Occurrence,
Mackenzie Mountains, Northwest Territories**

by

Meghan Leona Hewton

B.Sc. (Hons.), University of Western Ontario, 2010

Thesis Submitted In Partial Fulfillment of the
Requirements for the Degree of
Master of Science

in the
Department of Earth Sciences
Faculty of Science

© Meghan Leona Hewton 2012

SIMON FRASER UNIVERSITY

Fall 2012

All rights reserved.

However, in accordance with the *Copyright Act of Canada*, this work may be reproduced, without authorization, under the conditions for "Fair Dealing." Therefore, limited reproduction of this work for the purposes of private study, research, criticism, review and news reporting is likely to be in accordance with the law, particularly if cited appropriately.

Approval

Name: Meghan Leona Hewton
Degree: Master of Science (Earth Sciences)
Title of Thesis: *Investigation of the Mountain River Beryl (Emerald Variety), Mackenzie Mountains, Northwest Territories*
Examining Committee: Chair: Daniel Gibson
Associate Professor

Dr. Dan Marshall
Senior Supervisor
Professor

Dr. Derek Thorkelson
Supervisor
Professor

Dr. Lee Groat
External Examiner
Professor, Department of
Earth and Ocean Sciences
University of British Columbia

Date Defended/Approved: December 17, 2012

Partial Copyright License



The author, whose copyright is declared on the title page of this work, has granted to Simon Fraser University the right to lend this thesis, project or extended essay to users of the Simon Fraser University Library, and to make partial or single copies only for such users or in response to a request from the library of any other university, or other educational institution, on its own behalf or for one of its users.

The author has further granted permission to Simon Fraser University to keep or make a digital copy for use in its circulating collection (currently available to the public at the "Institutional Repository" link of the SFU Library website (www.lib.sfu.ca) at <http://summit/sfu.ca> and, without changing the content, to translate the thesis/project or extended essays, if technically possible, to any medium or format for the purpose of preservation of the digital work.

The author has further agreed that permission for multiple copying of this work for scholarly purposes may be granted by either the author or the Dean of Graduate Studies.

It is understood that copying or publication of this work for financial gain shall not be allowed without the author's written permission.

Permission for public performance, or limited permission for private scholarly use, of any multimedia materials forming part of this work, may have been granted by the author. This information may be found on the separately catalogued multimedia material and in the signed Partial Copyright Licence.

While licensing SFU to permit the above uses, the author retains copyright in the thesis, project or extended essays, including the right to change the work for subsequent purposes, including editing and publishing the work in whole or in part, and licensing other parties, as the author may desire.

The original Partial Copyright Licence attesting to these terms, and signed by this author, may be found in the original bound copy of this work, retained in the Simon Fraser University Archive.

Simon Fraser University Library
Burnaby, British Columbia, Canada

revised Fall 2011

Abstract

Emerald at the Mountain River emerald occurrence is milky green and occurs in extensional quartz-carbonate veins hosted within organic-poor siliciclastic rocks. Oxygen isotope mineral pair equilibration thermometry indicates mineralization temperatures of 379 to 415°C. Fluid inclusion analyses indicate CO₂-N₂-bearing brines and homogenization temperatures between 118 and 258°C. Fluid pressures were on the order of 2.4 to 4.0 kbar, corresponding to depths of 9 to 15 km. Pyrite intergrown with emerald yields a 5 point Re-Os model 1 isochron age of 345 ± 20 Ma and an elevated initial ¹⁸⁷Os/¹⁸⁸Os of 3.2, indicating a crustal source. The fluids involved in emerald mineralization were derived from deep-seated hydrothermal brines, and were likely the same fluids involved in producing the Manetoe facies dolomite and extensive carbonate-hosted zinc-lead occurrences throughout the Mackenzie Platform.

The Mountain River emerald occurrence shares many characteristics with Colombian-type emerald deposits. The Colombian emeralds are hosted in organic-rich black shales and formed during compressional deformation via thermochemical sulphate reduction of brines by organic matter. However, the Mountain River occurrence is hosted in organic-poor siliciclastic rocks and formed in an extensional back-arc environment via inorganic sulphate reduction. The Mountain River emerald occurrence thus represents a modification of the Colombian-type deposit model.

Keywords: beryl; emerald; Mackenzie Mountains; fluid inclusion; stable isotope; Re-Os isochron

This thesis is dedicated to my parents, Mary and Brad. Without their unfailing love and support, I could not have done this.

Acknowledgements

I would like to express my sincere gratitude to my supervisor, Prof. Dan Marshall, whose expertise and patience added considerably to my graduate experience. I appreciate his vast knowledge and skill in many areas, and his assistance in writing reports and grant and scholarship applications. A very special thank you goes to Luke Ootes, who has been a constant source of support and knowledge since day one, and I am forever grateful to have been able to work so closely with him. I would like to thank Val Jackson of the NTGO for being an inspiration to me and dozens of other students. Val taught me everything I know about mapping and the Wopmay, and she has inspired me to be the best geologist I can be. Big thanks to Carl Ozyer for his funding and assistance in the Mackenzie Mountains, and Edith Martel for her initial work on the MRB. Thanks also go to Melanie Mercier for laying down a solid foundation for future work on the MRB. I would also like to thank Prof. Dan Gibson for the many conversations and lectures about the tectonic history of the Northern Cordillera, and for a great cross-Cordillera field trip. Thanks are due to Rob Creaser for his swift determination of the age of the MRB using the Re-Os pyrite system at the University of Alberta, but more importantly, for giving me an idea that fundamentally shaped my final interpretation and model. Kerry Klassen and April Vuletich from Queen's University are acknowledged for stable isotope analyses. I would like to thank Prof. Mati Raudsepp and Edith Czech at the University of British Columbia for guiding me on electron microprobe analysis of beryl. Dave Lee at SFU Physics is acknowledged for his patience and the hours spent over discussions of beryl crystallography. I would like to thank the other member of my committee, Prof. Derek Thorkelson, for his valuable suggestions that improved this thesis. I'd also like to thank Steve Gordey at the GSC and Maurice Colpron at the YGS for discussions on the geology and tectonic history of the northern Cordillera and Mackenzie Mountains.

I would especially like to thank my family and friends for the support they provided me through my academic career. In particular, I'd like to acknowledge my labmate, former student, and homegirl Lara, who suffered the early work on the MRB fluid inclusions and sympathized when I was measuring my own. Thanks to all of my colleagues at SFU and UBC without whom I would not have survived SFU and finished this thesis, especially my girls Andrea, Nancy, Joanna, Jolene, and Stacy.

This research would not have been possible without the financial assistance of NSERC (DM and MH), the NTGO and Government of the Northwest Territories, the Northern Scientific Training Program, the Department of Earth Sciences at SFU (Teaching Assistantships, Graduate Research Scholarships, Research Assistantships, and Graduate Fellowships to MH), the NWT & Nunavut Chamber of Mines (award to MH), and the Society of Economic Geologists Canada Foundation (Student Research Grant to MH), and I would like to express my gratitude to these organizations.

Table of Contents

Approval.....	ii
Partial Copyright License	iii
Abstract.....	iv
Dedication	v
Acknowledgements	vi
Table of Contents.....	viii
List of Tables.....	x
List of Figures.....	xi
Preface.....	xv
1. Introduction	1
1.1. Emerald.....	1
1.2. Goals of this thesis	3
1.3. Location, access, exposure, and sampling	4
1.4. Regional geology and tectonic history of the Mackenzie Mountains	5
1.5. Local geology	10
References.....	17
2. Petrography	20
2.1. Host rocks and alteration.....	20
2.2. Beryl-bearing veins.....	23
2.3. Beryl-free veins	28
2.4. Summary and discussion.....	28
References.....	31
3. Cathodoluminescence of Al zoning in a Colombian-style beryl and emerald occurrence: Implications for geochemical fingerprinting and growth history	32
3.1. Abstract.....	33
3.2. Introduction	34
3.3. Geologic setting and crystal petrography.....	37
3.4. Samples and analytical methods	39
3.4.1. Scanning electron microscopy and cathodoluminescence.....	39
3.4.2. Electron microprobe analysis	40
3.4.3. Raman spectroscopy	40
3.5. Results and discussion.....	41
3.5.1. Backscattered electron and cathodoluminescence imaging	41
3.5.2. Electron microprobe analysis	44
3.5.3. Raman spectroscopy	53
3.5.4. Compositional evolution of beryl	54
3.5.5. Geochemical signature of beryl.....	56
3.6. Conclusions.....	59
3.7. Acknowledgements	60
References.....	61

4. Colombian-style emerald mineralization in the northern Canadian Cordillera: Integration into a regional Paleozoic fluid flow regime.....	64
4.1. Abstract.....	65
4.2. Introduction	66
4.3. Geologic setting.....	68
4.4. Local geology and vein petrology	70
4.5. Results.....	71
4.5.1. Fluid inclusion studies.....	71
4.5.2. Stable isotopes	77
4.5.3. Geochronology.....	79
4.6. Discussion.....	81
4.6.1. Constraints on fluid conditions and source.....	81
4.6.2. Constraints on the timing of mineralization.....	90
4.6.3. A Colombian-like mineralization model.....	91
4.7. Conclusions.....	92
4.8. Acknowledgements	92
References.....	94
4.9. Appendix: Analytical Procedures	98
Appendix: References	100
5. Deposit type and conclusions	101
5.1. Similarities with Type 3 Colombian systems	103
5.2. Differences from Type 3 Colombian systems.....	104
5.3. Summary.....	107
References.....	108
Appendices.....	110
Appendix A: Sample locations.....	111
Appendix B: Bulk rock geochemistry.	122

List of Tables

Table 3-1. Compositions of zoned beryl determined from electron microprobe analysis.	46
Table 3-1. Continued.	47
Table 4-1. Microthermometric data from quartz- and emerald-hosted fluid inclusions from the Mountain River emerald occurrence.	73
Table 4-2. Stable isotope data of quartz, emerald, dolomite, and pyrite collected from emerald-bearing veins	77
Table 4-3. Re-Os data from pyrite taken from an emerald-bearing vein.	80
Table A-1. Listed locations, descriptions, samples, and measured structures from field stations.....	111
Table B-1. Major, minor, and trace element compositions of whole rock samples.	124
Table B-2. Quality control data for whole rock geochemical standards and blanks.....	129

List of Figures

Figure 1-1. The cyclosilicate structure of beryl, viewed down the c axis.	1
Figure 1-2. Location of the Mountain River beryl showing in the Mackenzie Mountains, relative to other northern Cordilleran emerald occurrences, major regional structures, and Mesozoic granitoid intrusions.	5
Figure 1-3. Representative stratigraphy of the Mackenzie Mountains in the area of the Mountain River.	8
Figure 1-4. Geologic map of the Mountain River area. Modified from Gordey et al. (2011b).	12
Figure 1-5. Carbonate-quartz-beryl veins cutting pink-grey gritty sandstone of the Twitya Formation are 3mm to 17cm wide, and strike 250° and dip 71°. Hammer for scale.	13
Figure 1-6. Radiating milky green euhedral fractured beryl crystals in a quartz-dolomite vein. The vein strikes 215° and dips 54°. Pencil for scale.	13
Figure 1-7. Massive vein of anhedral green beryl with white quartz in gritty sandstone of the Twitya Formation. Hammer for scale.	14
Figure 1-8. Massive vein of blue aquamarine and rusty weathering Fe-carbonate intersecting vein of quartz, purple albite, and Fe-carbonate.	14
Figure 1-9. Geologic map of the Mountain River beryl occurrence.	15
Figure 1-10. Footwall limestones are fractured and brecciated, as mosaic breccia with a calcite matrix. Pen for scale.	16
Figure 2-1. Representative scanned thin sections of host rock textures and alteration styles.	21
Figure 2-2. Subhedral pyrite (py) is intergrown with calcite alteration within the fine-grained carbonatized siltstone host rock proximal to a calcite (cal) and quartz (qtz) vein (upper right). Sample 10mh19Di.	22
Figure 2-3. A zone of grain size reduction and carbonate alteration (dashed yellow line) is pronounced near to vein edges in some samples. Sample 10mh11Avii.	22
Figure 2-4. Typical textures of beryl in thin section.	24
Figure 2-5. Red luminescence in a fractured zoned beryl crystal. A highly luminescent core surrounded by oscillatory zonation in a wide rim is visible in scanning electron microscopy using wavelength filtered CL.	25

Figure 2-6. Quartz in the veins shows strain in the form of micro-kinking filled by cryptocrystalline calcite (cal) and quartz (qtz). Sample 10mh19Di. Image taken in cross polarized transmitted light.	25
Figure 2-7. Zoned pyrite with rounded core and pyritohedral rim. Mineral inclusions (yellow arrow) were identified as a silver-bearing iron sulphide with an approximate formula of $\text{Ag}_2\text{Fe}_6\text{S}_{17}$. Sample MM2.	27
Figure 2-8. Rutile inclusions in zoned beryl. Sample 10mh11Av. Image taken in plane polarized transmitted light.	27
Figure 2-9. Paragenetic sequence of vein and host rock alteration minerals.	29
Figure 3-1. a) The cyclosilicate structure of beryl, viewed down the c axis, showing BeO_4 tetrahedra (dark grey), AlO_6 octahedra (medium grey), and rings of SiO_4 tetrahedra (light grey) which form hollow channels. Alkali cations (Na, K, Rb, Cs; + sign), water molecules, or vacancies (square) may exist at channel sites. Modified from Groat et al. (2008). b) Water molecules in channel sites exist either as free H_2O oriented so that its molecular symmetry axis is perpendicular to the crystal c axis (type I), or as H_2O associated with an alkali cation and oriented with its molecular symmetry axis parallel to the crystal c axis (type II)..	35
Figure 3-2. Photomicrographs of the studied crystals showing zoned cores that are optically continuous with rims. Samples a) 01Ai-2, b) 01-Ai-3, c) 01Bi-5, and d) 01Bi-6. Images taken using cross-polarized transmitted light microscopy.	39
Figure 3-3. Panchromatic cathodoluminescence (CL) images of the crystals studied showing bright cores and outer oscillatory zoning.	42
Figure 3-3. Continued.	43
Figure 3-4. Element plots obtained from EMPA data in atoms per formula unit (apfu).	48
Figure 3-5. An element plot obtained from EMPA data in atoms per formula unit (apfu) in which Al shows a very weak negative correlation to Si, for which it may substitute in the beryl structure.	49
Figure 3-6. Element plots obtained from EMPA data in atoms per formula unit (apfu) comparing element concentrations to CL intensity (dark vs. bright) for the crystals studied.	51
Figure 3-6. Continued.	52

Figure 3-7. Raman spectra of beryl crystals in the water range of 4300 to 2700 cm^{-1} , for samples a) 10mh01B and b) 10mh11Avii. I = intensity in total counts. Water oriented in the type I configuration is identified by a band at 3608 cm^{-1} , and the type II configuration is identified by a band at 3598 cm^{-1}	54
Figure 3-8. Diagrams of emerald compositions based on genetic type in terms of a) $\text{FeO-MgO-Cr}_2\text{O}_3$, b) $\text{FeO-V}_2\text{O}_3\text{-Cr}_2\text{O}_3$, and c) $\text{Sc}_2\text{O}_3\text{-V}_2\text{O}_3\text{-Cr}_2\text{O}_3$. Types 1, 2, and 3 data from Groat et al. 2008.	57
Figure 3-9. Intensity ratios of the two Raman shift bands assigned to the two water types versus the total alkali contents for beryl from Mountain River compared to emeralds from around the world. Higher alkali contents correlate strongly with higher intensity ratios. Types 1, 2, and 3 data from Le Thi-Thu et al. (2010).	58
Figure 4-1. Location of the Mountain River emerald occurrence in the Mackenzie Mountains in relation to the Lened and Tsa da Glisza occurrences and the extent of Cretaceous felsic plutonism (dark grey).....	67
Figure 4-2. Local geology of the Mountain River emerald occurrence in the Mount Eduni map area (NTS 106A southwest). Modified from Gordey et al. (2011a).	69
Figure 4-3. Two-phase fluid inclusions from (a) quartz and (b) emerald consist of brine and $\text{CO}_2\text{-N}_2$ vapour bubble at room temperature.....	72
Figure 4-4. Summary of fluid inclusion microthermometry obtained from emerald (a to c) and quartz (d to f) for ice melt temperatures ($T_{m(\text{ice})}$), clathrate melt temperatures ($T_{m(\text{cla})}$), and total homogenisation to the liquid phase ($T_{h(\text{total})}$).	76
Figure 4-5. A pyrite grain within emerald is consistent with coeval growth of the two minerals. The pyrite grain is 2 mm in diameter.	79
Figure 4-7. Homogenisation temperature versus salinity for calcite-, sphalerite-, quartz-, and emerald-hosted two-phase fluid inclusions from the Mountain River emerald occurrence and Bear-Twit carbonate-hosted Zn-Pb deposit. Bear-Twit data from Gleeson (2006).	82
Figure 4-8. Stable isotope ($\delta^{18}\text{O}$ and $\delta^{13}\text{C}$) values from vein dolomite and calcite cogenetic with emerald mineralization from the Mountain River and east and west zones of Colombia.	83
Figure 4-9. Stable isotope ($\delta^{18}\text{O}$ and $\delta^{13}\text{C}$) values from vein dolomite and calcite cogenetic with emerald mineralization from the Mountain River and east and west zones of Colombia.	85
Figure 4-10. Pressure-temperature diagram showing the range of formational conditions for the Mountain River veins.	88

Figure 4-11. Tectonic model at the time of emerald mineralization, ca. 345 Ma. a) Fluid circulation model for the mineralization of the Mountain River emerald occurrence.....	89
Figure 5-1. Schematic representation of emerald mineralization at MRB. H ₂ SO ₄ - bearing brines were sourced from gypsumiferous beds of the Little Dal or Coates Lake groups and ascended along extensional or transfer faults.....	105
Figure 5-2. Tectonic environments of emerald mineralization in (a) Colombia (ca. 38-31.5 Ma) and (b) MRB (ca. 345 Ma)..	107

Preface

This thesis presents new data and a deposit model describing the genesis of the Mountain River beryl occurrence, Canada's fifth emerald discovery. Chapter 1 will act as an introduction to beryl and emerald occurrences, and in particular the Mountain River occurrence and its local and regional geology. Chapter 2 will present the petrography and mineralogy of veins and host rock at the occurrence. A version of Chapter 3 has been submitted as a journal article to *American Mineralogist* and discusses the cathode luminescent properties, crystal chemistry, zonation, and growth history of emerald at Mountain River. A version of Chapter 4 has been submitted as a journal article to the *Canadian Journal of Earth Sciences* and discusses a model of formation as deduced from the occurrence's age, temperature and pressure conditions, fluid conditions, and fluid sources. Conclusions about the emerald deposit within the framework of accepted deposit types have been summarized in Chapter 5. The Mountain River emerald occurrence appears to belong to the category of sediment-hosted hydrothermal beryl deposits, and is geologically similar to the world famous emerald districts of Colombia.

A version of the paper presented as Chapter 3 was co-authored by D. Marshall and L. Ootes, who contributed to editing and the "big-picture" interpretation of emerald mineralization in a geologic and hydraulic framework.

A version of the paper presented as Chapter 4 was co-authored by D. Marshall, L. Ootes, L. Loughrey, and R. Creaser. Marshall was instrumental in the interpretation of stable isotope and fluid inclusion data, as well as being a major contributor to editing and writing. Ootes contributed immensely to the editing of text and figures throughout, and his knowledge and understanding of the regional geology and tectonics was influential in the development of a genetic model. Loughrey collected much of the fluid inclusion data. Creaser conducted the Re-Os isotopic analysis of pyrite reported in the paper, and provided the age and Os_i interpretation that cast light on the genesis of the Mountain River beryl occurrence.

1. Introduction

1.1. Emerald

Beryl is an aluminosilicate mineral with a cyclosilicate crystal structure (Fig. 1-1) produced by stacks of aluminum octahedra and beryllium tetrahedra alternating with rings of silicon tetrahedra which form hollow channels parallel to the crystal *c* axis (Deer et al. 1966). Beryl has an ideal chemical formula of $\text{Be}_3\text{Al}_2\text{Si}_6\text{O}_{18}$ but, due to the ease of substitution at the octahedral and tetrahedral sites, is better described by the formula $(\text{Be}_{3-X}, \text{Li}_{Y, X-Y})(\text{Al}, \text{Fe}, \text{Cr}, \text{V}, \text{Sc})^{3+}_{2-Z}(\text{Fe}, \text{Mg}, \text{Mn})^{2+}_Z\text{Si}_6\text{O}_{18} \cdot (\text{Na}, \text{K}, \text{Rb}, \text{Cs})_{2X-Y+Z}(\text{H}_2\text{O}, \text{He}, \text{Ar})_{\leq 2-(2X-Y+Z)+\text{Na}}$ where $(Y \leq 2)$, $(X \geq Y)$, $(Z < 2)$, and $(2X - Y + Z)$, and Na, K, Rb, Cs, H_2O , He, and Ar may occupy vacancies at channel sites (Turner and Groat 2007). Different colour varieties of gem-quality beryl are produced by the substitution of different chromophoric cations for aluminum at the octahedral site. The substitution of Cr and/or V gives beryl a deep green colour, and the gem is known as emerald.

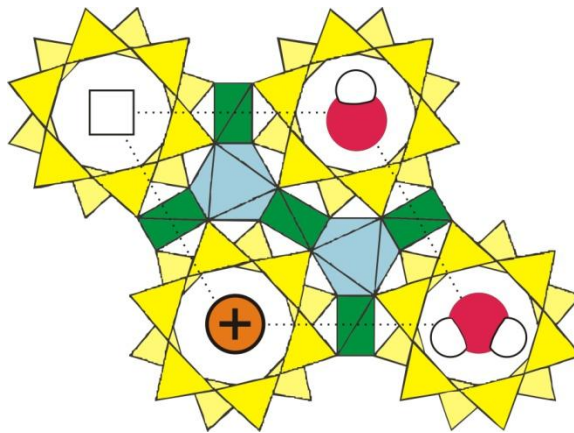


Figure 1-1. *The cyclosilicate structure of beryl, viewed down the *c* axis, is made of BeO_4 tetrahedra (green), AlO_6 octahedra (blue), and rings of SiO_4 tetrahedra (yellow) which form hollow channels. Alkalis (orange), water molecules (red), or vacancies may occupy channel sites. Modified from Turner and Groat (2007).*

Emerald mineralization requires the bringing together of Be with Cr and/or V, and therefore very specific geochemical and geological conditions must be met as these elements tend to fractionate into different rock types. Beryllium tends to fractionate into rocks of the continental crust, particularly granites, pegmatites, and shales, while Cr and V are concentrated in mafic and ultramafic rocks and black shales (Lentz 2003; Groat et al. 2007). As a result of this element partitioning, there are three major deposit types recognized in the literature (Schwarz and Giuliani 2001; Barton and Young 2002). The Type 1, or magmatic-associated, emeralds occur where Be-rich fluids derived from granitic, rhyolitic, or pegmatitic intrusions interact with Cr±V-bearing host rocks, generally mafic-ultramafic, schist, or black shale host rocks (e.g. Emmaville-Torrington, Australia; Mananjary, Madagascar; Ghost Lake, Ontario). The emeralds themselves are often found within the pegmatite bodies at the contact with the host rock. Type 2, or metamorphic, emeralds occur where upper greenschist to amphibolite facies metamorphism produces metasomatic fluids which circulate and scavenge Be and Cr±V locally. Mineralization is commonly associated with thrust faults and shear zones (e.g. Swat Valley, Pakistan; Habachtal, Austria; Santa Terezinha, Brazil). The Type 3 black shale-hosted emeralds are quite rare and represented by the world famous deposits of Colombia, where emeralds are found in extensional carbonate-silicate-pyrite veins, miarolitic cavities, and breccias in Early Cretaceous organic-rich black shale to carbonaceous shale (Cheillett and Giuliani 1996; Branquet et al. 1999). The sub-greenschist metamorphic grade sedimentary succession hosting the emerald deposits are up to 10 km thick and comprise marine siltstones, siliceous black shales, and carbonaceous black shales intercalated with limestone and anhydrite beds (Banks et al. 2000). The emerald precipitated from evolved sedimentary formational brines with salinities up to 40 wt% NaCl equivalent, which were likely derived from or interacted with evaporitic sulphate, and reduced by organic matter via thermochemical sulphate reduction (Ottaway et al. 1994; Cheillett and Giuliani 1996) at temperatures of 290 to 360°C and pressures of 1.06 to 1.12 kbar (Cheillett et al. 1994). Sulphate reduction produced H₂S and HCO₃⁻ (Cheillett and Giuliani 1996), which were responsible for the precipitation of pyrite, carbonates, and bitumen in the veins, resulting in the depletion of Fe from the fluids before emerald crystallization which produced very high quality crystals (Giuliani et al. 2012).

Emerald has historically been one of the most valuable and sought-after coloured gems available, and stones of superior quality may command more than US\$15,000 per carat, though ordinary stones are priced on the order of US\$12.50 to US\$250 per carat (Zachovay 2002). Other gem-quality beryl crystals, including aquamarine, heliodor, morganite, and goshenite, may also command high prices. Gem exploration and extraction contributes significantly to many local economies, particularly in Asia, Africa, and South America. Not only is beryl an important and valuable gem, it is also an important ore of beryllium, a strategic metal with applications in telecommunications, electronics, nuclear energy, ceramics, aerospace, and defense (Grew 2002). Beryllium consumption in the United States, the largest producer and consumer of beryllium, in 2011 was roughly 270 tons and valued at US\$121 million, up from 100 tons in 2007 (U.S. Geological Survey 2012). Even non-gem beryl occurrences may represent important economic ore reserves to supply growing industries. Beryl occurrences in Canada point toward possibilities for more significant discoveries, and understanding their geology, geochemical signatures, and models of formation will be important for future exploration and targeting of both gem-quality stones and beryllium ore.

The most recent Canadian discovery of emerald in 2007 at the Mountain River occurrence, Northwest Territories, and other discoveries of emerald (Tsa da Glisza, YT, Lened, NT, and Red Lake, B.C.) and aquamarine (True Blue, YT) in the northern Cordillera, have prompted interest in exploration in the Cordillera as a source of ethical and conflict-free rough gems (Walton 2004). With the exception of the Tsa da Glisza deposit which has produced some small rough stones, these occurrences have generally not yielded gem-quality material.

1.2. Goals of this thesis

The Mountain River beryl (MRB) showing is the fourth discovery of emerald in the Canadian Cordillera after Lened, Tsa da Glisza, and Red Lake. The MRB shares no geological similarities to these other occurrences, all of which are described by the type 1 deposit model. Discovered in 2007 by geologists from the Northwest Territories

Geoscience Office, the showing was only previously described by Mercier (2008). It was clearly different from earlier discoveries of Canadian emerald and from the currently accepted models of emerald genesis. The goal of this thesis is to establish the age and conditions of emerald mineralization, relate these findings to the geologic and tectonic history of the Mackenzie Mountains and Northern Cordillera, and produce a model for the genesis of emerald at Mountain River. This thesis will also compare the mineral chemistry of these geochemically unusual Sc-rich emeralds to other occurrences globally. Thus, this thesis has been divided into several chapters. Chapter 1 is an introduction to beryl and emerald occurrences, in particular the MRB occurrence and its local and regional geology. Chapter 2 will present the petrography and mineralogy of veins and host rock at the MRB occurrence. Chapters 3 and 4, the submitted articles, respectively discuss the crystal chemistry of emerald at MRB and its model of formation as deduced from its age, temperature-pressure conditions, fluid compositions, and fluid sources. Chapter 5 will summarize the findings of this thesis and compare the MRB occurrence to a known emerald deposit type.

1.3. Location, access, exposure, and sampling

The MRB study area (Fig. 1-2) is located in the Sayunei Range of the north-central Mackenzie Mountains (NTS map sheet 106A/06; UTM 7141024 N / 477188 E, NAD 83 Zone 9) approximately 10 km south-southeast of Palmer (Shale) Lake. Field work was carried out by the author, D. Marshall, L. Ootes, and C. Ozyer over six days in July 2010. The emerald-bearing veins outcrop on a north facing mountainside, and were accessed by helicopter from a base camp at Palmer Lake. The outcrop exposure in the study area is generally good, though much of the mountain is covered by talus. Sample locations and descriptions are reported in Appendix A (Table A-1). A few unlocated samples (DM08, MM2, and MM3) collected in the summer of 2007 (Mercier 2008) were also used in this study for petrographic observation and stable isotope analyses.

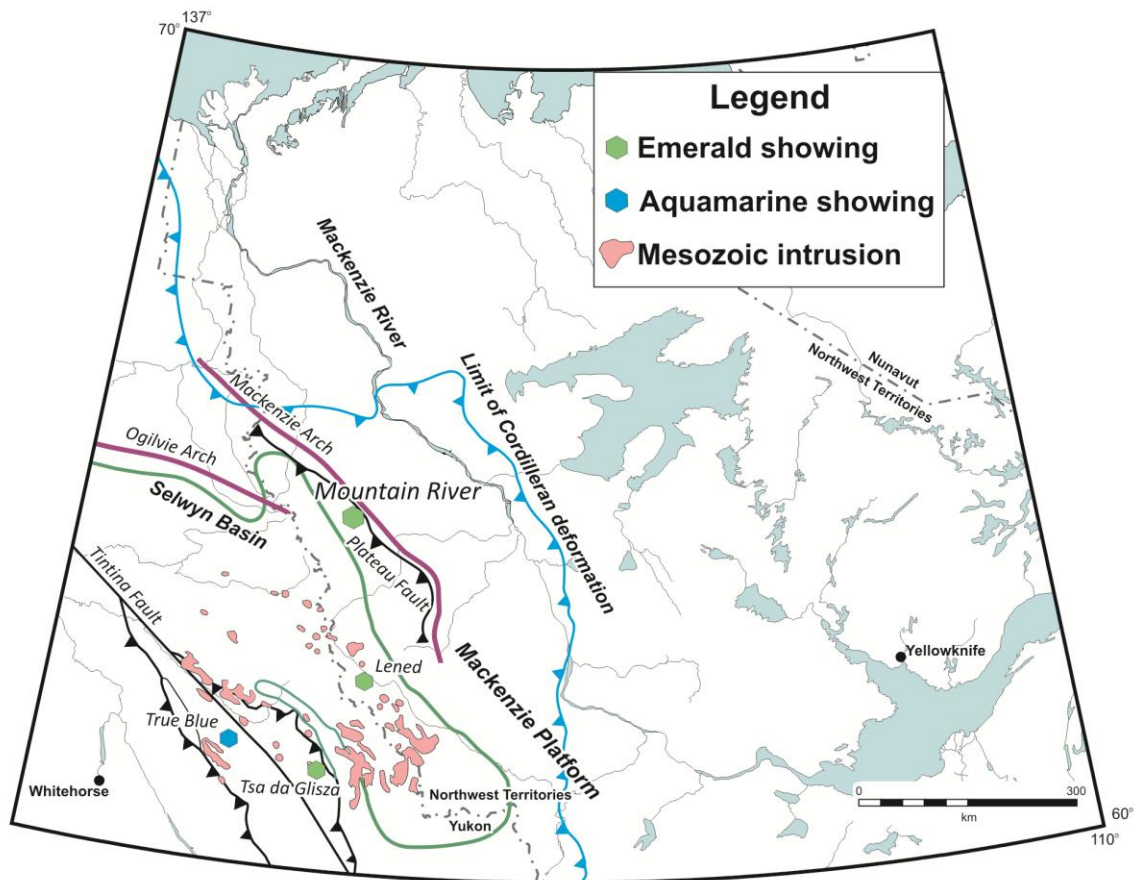


Figure 1-2. Location of the Mountain River beryl showing in the Mackenzie Mountains, relative to other northern Cordilleran emerald occurrences, major regional structures, and Mesozoic granitoid intrusions. The green line defines the eastern limit of the Selwyn Basin west of the Mackenzie Platform. Modified from Rasmussen et al. (2006) and Gordey et al. (2011a).

1.4. Regional geology and tectonic history of the Mackenzie Mountains

The Mackenzie Mountains lie within the northernmost extent of the foreland fold and thrust belt of the Canadian Cordillera, and are composed of a nearly complete sequence of well-preserved siliciclastic, carbonate, and minor evaporite rocks subjected to sub-greenschist grade metamorphism (Martel et al. 2011). These strata record the early rifting and breakup of the supercontinent Rodinia during the Neoproterozoic and

the establishment of the Mackenzie Platform east of the Selwyn Basin during the Paleozoic (Ross 1991). From oldest to youngest, the stratigraphic succession in the Mackenzie Mountains consists of the Mackenzie Mountains Supergroup, Windermere Supergroup, and overlying Paleozoic platformal facies strata (Fig. 1-3). The Mackenzie Mountains Supergroup is interpreted as having been deposited in an epicratonic basin and contains fluvial and deltaic deposits from a continental scale river system which drained the Grenville and Yavapai-Mazatzal orogenies, as well as the more proximal granitic pluton-rich Taltson-Thelon belt, Trans-Hudson Orogen, Slave Province, Hearne Province, and Hottah terrane (Rainbird et al. 1992; Leslie 2009). Gypsumiferous evaporite units of the Little Dal Group were deposited in a shallow-water setting and played a key role during Mesozoic deformation (Gordey and Roots 2011). Deposition of the Windermere Supergroup began in a shallow-water and arid, evaporitic setting (Coates Lake Group), immediately followed by rapid facies changes, syn-depositional extensional faulting, and deposition of unconformably overlying glaciogenic diamictites and rhythmites of the Rapitan Group (Klein and Beukes 1993). The subsequent succession consists of three shoaling-upward cycles: Twitya-Keele, Sheepbed-Gametrail, and Blueflower-Risky formations. The Blueflower and Risky formations are not preserved in the vicinity of the MRB occurrence. All three cycles comprise deep-water siliciclastic and shaley sediment grading into shallower carbonate platform deposits (Gordey and Roots 2011). The Windermere Supergroup reflects the rifting and breakup of Rodinia and continued sourcing of sediment from plutonic terranes to the east (Leslie 2009). During the Early to Middle Paleozoic, the newly formed western margin of Laurentia was characterized by the establishment of an extensive carbonate platform punctuated by sporadic episodes of renewed rifting, while deeper water siliciclastic deposits and barite-base metal sedimentary exhalative deposits accumulated to the west in the Selwyn Basin (Goodfellow 2007). This continued until the Middle to Late Devonian, when the far field effects of compression to the north-north east (Ellesmerian Orogeny) and subduction followed by extensional slab roll-back to the west, culminating in the separation of the Yukon-Tanana Terrane, began (Gordey and Roots 2011). These effects combined to produce a tectonically complex extensional or trans-tensional back-arc basin (Nelson et al. 2002; Gordey and Roots 2011). A passive margin setting was re-established during the Middle Mississippian, although very little has been

preserved of these units. Compressional tectonic activity resumed in the Jurassic to Cretaceous with the accretion of terranes to the west (Gordey and Roots 2011).

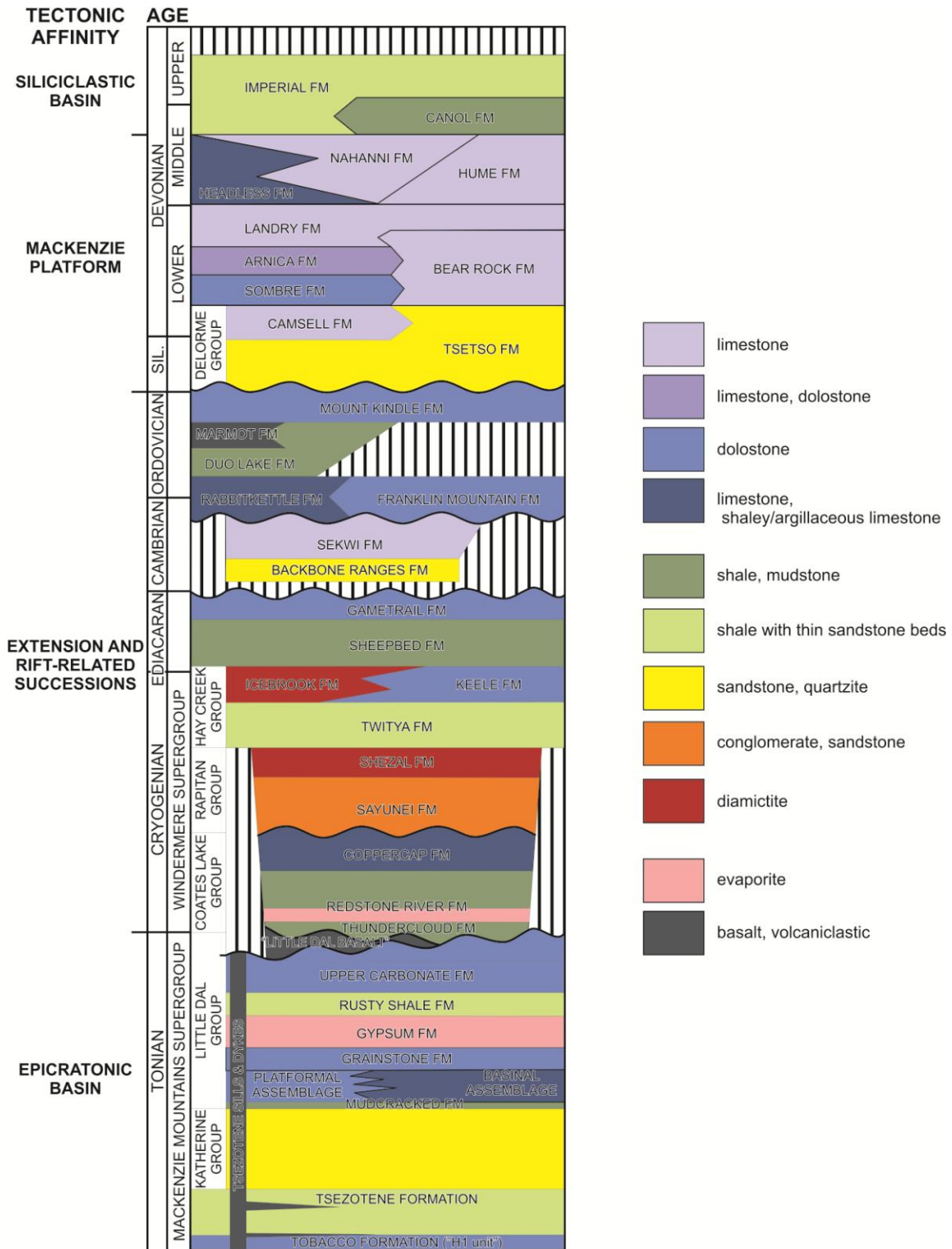


Figure 1-3. Representative stratigraphy of the Mackenzie Mountains in the area of the Mountain River. Simplified after Dewing et al. (2006), Gordey et al. (2011a), Gordey and Roots (2011), and Ootes et al. (in print).

The rocks of the Mackenzie Mountains were thrust and folded into their current configuration of broad regional folds, local tight folds, and thrust faults by Cretaceous-Tertiary deformation (Dewing et al. 2006; Gordey and Roots 2011). Numerous orogen-parallel thrust faults occur throughout the Mackenzie Mountains, one of which, the Shale Lake fault, is a major southwest-dipping thrust fault accounting for up to 15 km of shortening (Gordey et al. 2011a). Many of the carbonate units of the region have experienced moderate to extensive carbonate alteration. This alteration is due to six distinct fluid events identified by Morris and Nesbitt (1998) which span the Paleozoic to early Tertiary: 1) a Silurian sedimentary exhalative event associated with the expulsion of brines onto the seafloor along extensional faults; 2) diagenetic dolomitization affecting Early Devonian and older carbonates; 3) a Late Devonian to Mississippian regionally extensive Manetoe Facies hydrothermal dolomitization event associated with carbonate-hosted Zn-Pb mineralization and natural gas reserves; 4) a suggested Early Cretaceous or later vug-fill event, constrained by low δD values; 5) Early Cretaceous to Early Tertiary fault-hosted and high angle carbonate and quartz veins; and 6) calcite-barite mineralization infilling large voids and karsts deposited by inflowing meteoric water. These events represent the protracted history of fluid movement resulting from the evolving tectonic environment of the Northern Cordillera. Nelson et al. (2002) and Lund (2008) related the Late Devonian to Mississippian dolomitization event and extensive Mississippi Valley type (MVT)-like Zn-Pb mineralization to syngenetic sedimentary exhalative (SEDEX) and volcanogenic-hosted massive sulphide (VHMS) deposits of the same age farther to the west. They argued that the high temperature, high salinity fluids involved in MVT-like mineralization were driven by far-field effects of compression, subduction, and extension along the western margin of Laurentia, which also resulted in the development of a complex back-arc basin as the Slide Mountain Ocean opened and Yukon-Tanana rifted from Laurentia. The accompanying exhalative activity and hydrothermal fluids were driven along back-arc structures and permeable units (Nelson et al. 2002).

1.5. Local geology

The MRB occurrence is located in the Central Facies Belt of the Mackenzie Mountains, and occurs in the hangingwall of the Shale Lake fault (Fig. 1-4)(Gordey et al. 2011a). Beryl- and emerald-bearing extensional veins are hosted in bedded sandstones and siltstones of the Neoproterozoic Twitya Formation (Fig. 1-5). Beryl occurs as milky green euhedral crystals with radiating habit or as individual crystals within the veins (Fig. 1-6), and also occurs in massive to granular and anhedral habits (Fig. 1-7). Rare gem-quality emerald occurs as euhedral individual crystals in quartz-only or carbonate-only veins. Beryl and emerald crystals range in size from 1 to 10 mm wide and up to 5 cm long. Beryl typically occurs along vein selvages, but locally occurs towards the centres of carbonate-dominated veins. Minor minerals identified in the veins include pyrite, rutile, blue-violet albite, and trace aquamarine (Fig. 1-8). The veins are discordant to bedding and are moderately to steeply dipping to the north, with most striking between 220° to 300° (Fig. 1-9). A minor set of veins are sub-perpendicular to the main set and generally have strikes of 110° to 170°. The host rocks are orange to buff to pink-grey weathering massively bedded gritty sandstones, thinly bedded silty sandstones, and laminated shaley siltstones, with minor beds of buff-weathering massive silty dolostone. Localized bleached zones adjacent to emerald-bearing veins are several millimeters to 2 cm wide. Nearly all host rocks are affected by pervasive, weak to moderate carbonate alteration (predominantly dolomite), and are fractured, faulted, and folded in the immediate hangingwall of the Shale Lake fault. A younger generation of very thin veinlets cross-cuts quartz-carbonate(±beryl) veins. These veinlets are relatively rare, are up to 3 mm in width, and consist of quartz, green muscovite, and illite. Trace amounts of chalcopyrite and secondary chrysocolla were also identified at the MRB occurrence coating host rocks, but were not found in veins. A nearby copper occurrence (Twitya Cu±Ag; Ootes et al. 2011) may be linked to the trace copper-bearing minerals at Mountain River.

The fault places the Twitya Formation above limestone of the Early Devonian Arnica Formation (Fig. 1-4). The footwall limestones are fractured and brecciated, as mosaic and crackle breccia with a calcite matrix and calcite veins several millimetres to centimetres wide (Fig. 1-10). Like most faults of the foreland, the Shale Lake fault is believed to have developed during Cretaceous-Tertiary compression and deformation

(MacNaughton et al. 2008). The fault is listric and likely rooted at the depth of the evaporitic Gypsum Formation of the Neoproterozoic Little Dal Group, approximately 8 km below the current erosional level (Gordey et al. 2011a).

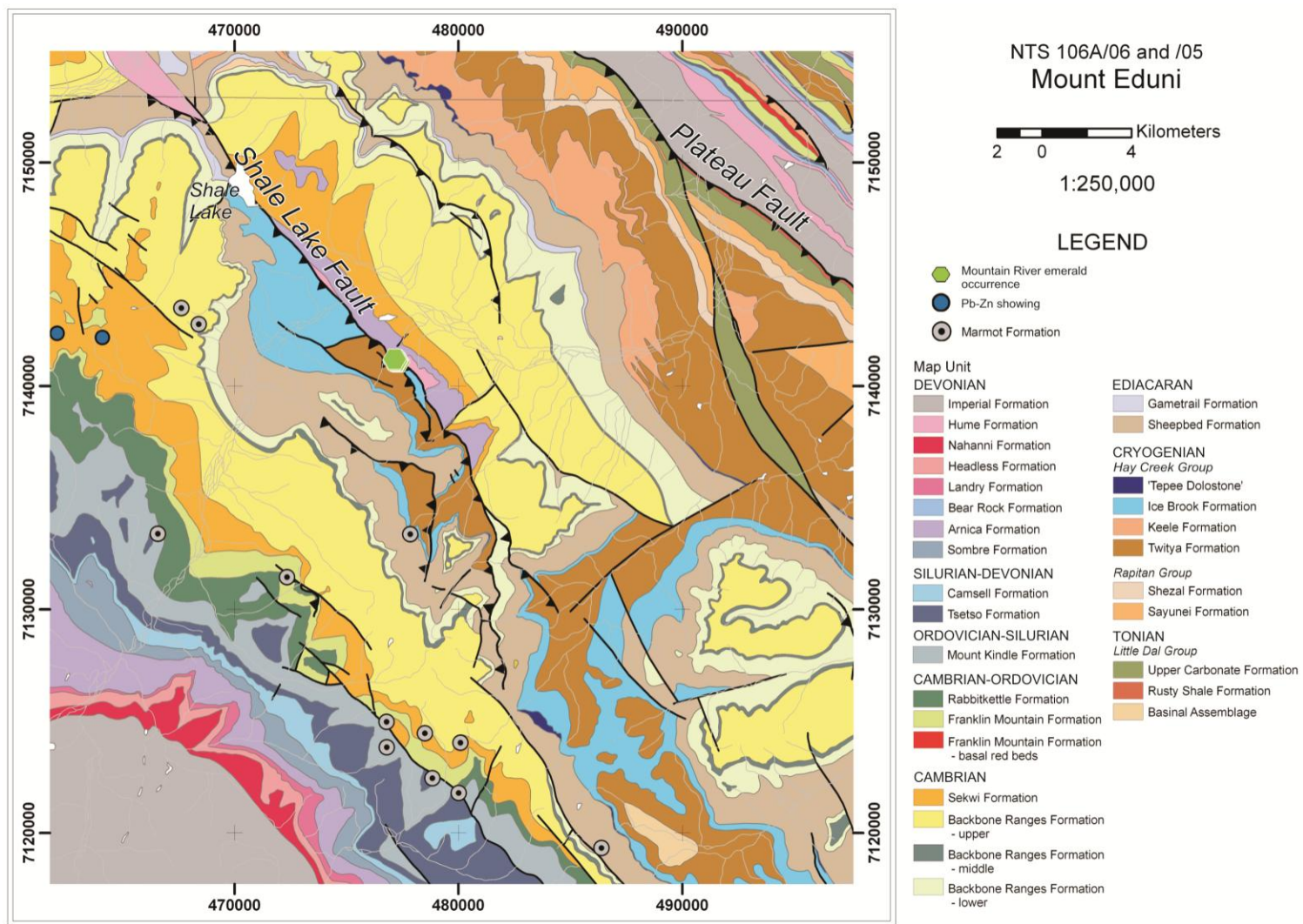


Figure 1-4. Geologic map of the Mountain River area. Modified from Gordey et al. (2011b).



Figure 1-5. Carbonate-quartz-beryl veins cutting pink-grey gritty sandstone of the Twitya Formation are 3mm to 17cm wide, and strike 250° and dip 71° . Hammer for scale.

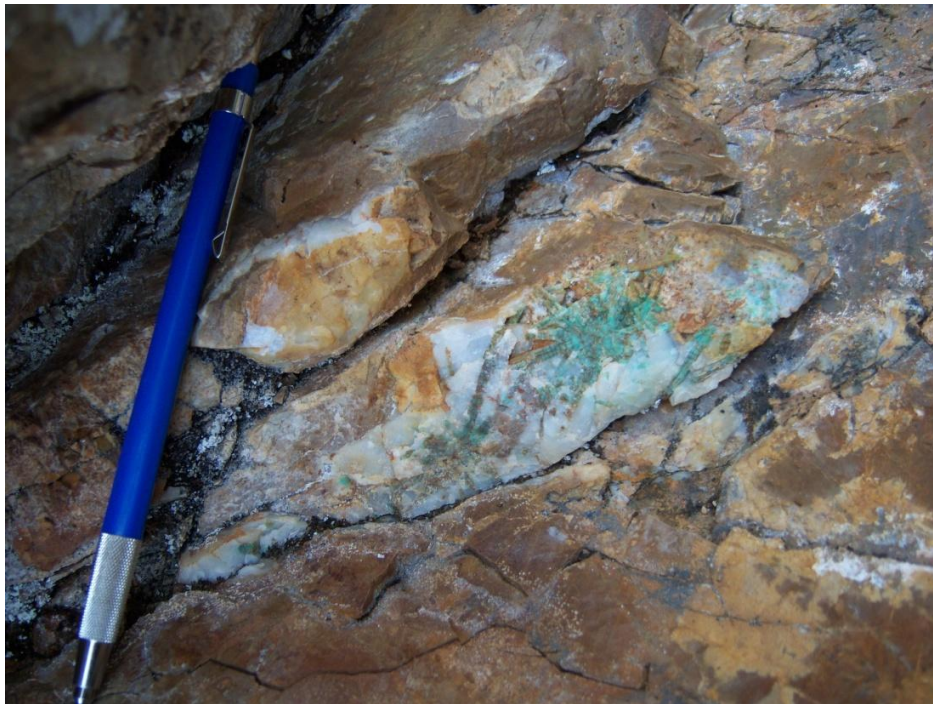


Figure 1-6. Radiating milky green euhedral fractured beryl crystals in a quartz-dolomite vein. The vein strikes 215° and dips 54° . Pencil for scale.



Figure 1-7. *Massive vein of anhedral green beryl with white quartz in gritty sandstone of the Twitya Formation. Hammer for scale.*



Figure 1-8. *Massive vein of blue aquamarine and rusty weathering Fe-carbonate intersecting vein of quartz, purple albite, and Fe-carbonate.*

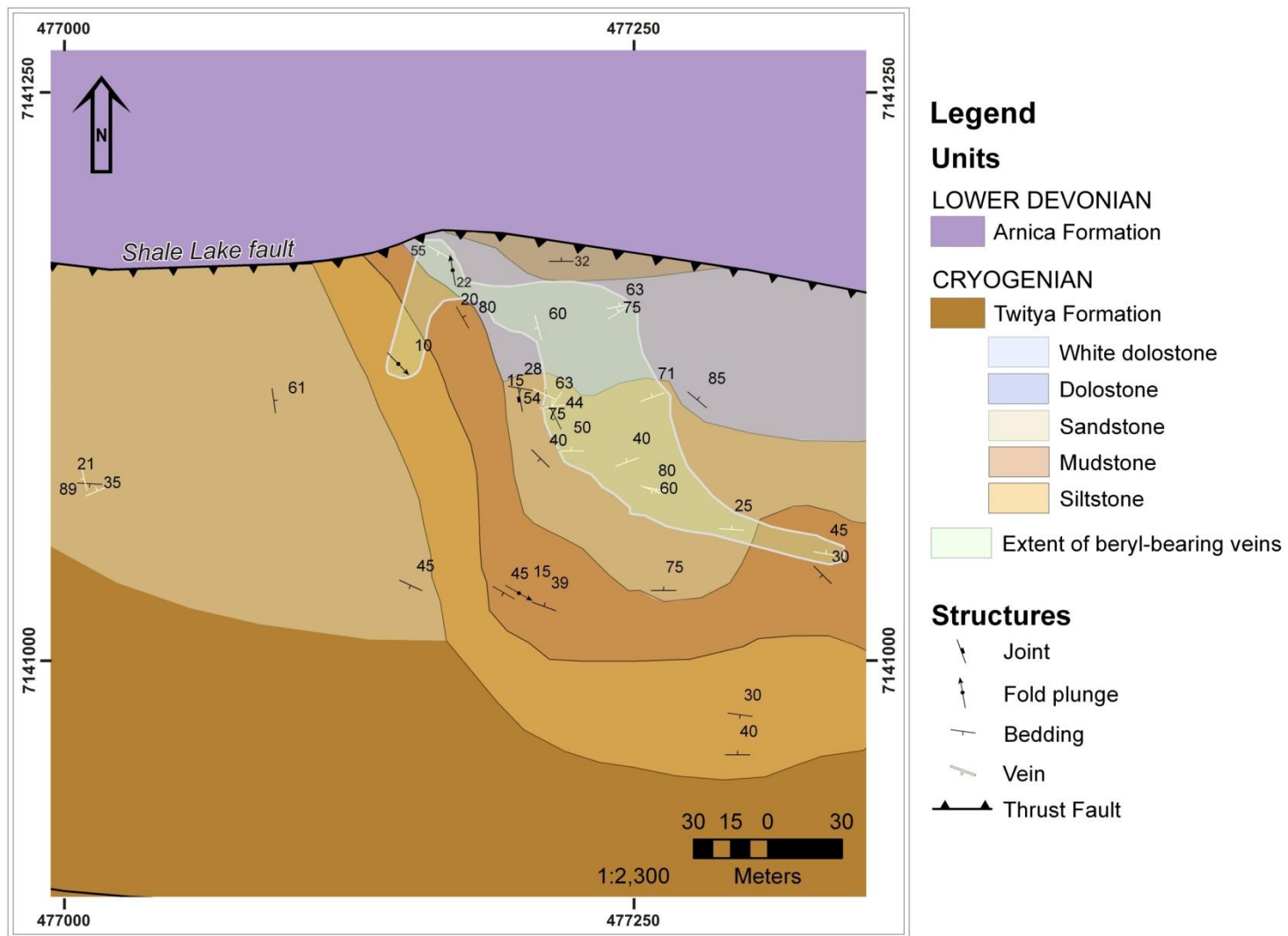


Figure 1-9. Geologic map of the Mountain River beryl occurrence.



Figure 1-10. *Footwall limestones are fractured and brecciated, as mosaic breccia with a calcite matrix. Pen for scale.*

References

- Banks, D.A., Giuliani, G., Yardley, B.W.D., and Cheilletz, A. 2000. Emerald mineralisation in Colombia: fluid chemistry and the role of brine mixing. *Mineralium Deposita*, **35**: 699-713.
- Barton, M.D., and Young, S. 2002. Non-pegmatitic deposits of beryllium: mineralogy, geology, phase equilibria and origin. *In Beryllium: Mineralogy, Petrology, and Geochemistry. Edited by E.S. Grew. Reviews in Mineral Geochemistry*, **50**: 591-691.
- Branquet, Y., Laumonier, B., Cheilletz, A., and Giuliani, G. 1999. Emeralds in the Eastern Cordillera of Colombia: Two tectonic settings for one mineralization. *Geology*, **27**(7): 597-600.
- Cheilletz, A., Féraud, G., Giuliani, G., and Rodriguez, C. T. 1994. Time-pressure and temperature constraints on the formation of Colombian emeralds: An $^{40}\text{Ar}/^{39}\text{Ar}$ laser microprobe and fluid inclusion study. *Economic Geology*, **89**: 361-380.
- Cheilletz, A., and Giuliani, G. 1996. The genesis of Colombian emeralds: A restatement. *Mineralium Deposita*, **31**: 359-364.
- Deer, W.A., Howie, R.A., and Zussman, J. 1966. *An Introduction to the Rock-Forming Minerals*, 528 p. Longman Group Limited, London.
- Dewing, K., Sharp, R.J., Ootes, L., Turner, E.C., and Gleeson, S. 2006. Geological assessment of known Zn-Pb showings, Mackenzie Mountains, Northwest Territories. Geological Survey of Canada, Current Research 2006-A4, 12 p.
- Giuliani, G., Ohnenstetter, D., Fallick, A.E., Groat, L.A., and Feneyrol, J. 2012. Geographic origin of gems linked to their geological history. *InColor*, **19**: 16-27.
- Goodfellow, W.D. 2007. Base metal metallogeny of the Selwyn Basin, Canada. *In Mineral Deposits of Canada: A Synthesis of Major Deposit Types, District Metallogeny, the Evolution of Geological Provinces, and Exploration Methods. Edited by W. D. Goodfellow. Geological Association of Canada, Mineral Deposits Division, Special Publication No. 5, p. 553-579.*
- Gordey, S.P., MacDonald, J.D., Roots, C.F., Fallas, K., and Martel, E. 2011a. Regional cross-sections, detachment levels and origin of the Plateau fault, central Mackenzie Mountains, Northwest Territories; Northwest Territories Geoscience Office, NWT Open File 2010-18. 1 sheet, scale 1:100,000.
- Gordey, S. P., Martel, E., Fallas, K., Roots, C.F., MacNaughton, R., and MacDonald, J. 2011b. Geology of Mount Eduni, NTS 106A Southwest, Mackenzie Mountains, Northwest Territories; Northwest Territories Geoscience Office, NWT Open File 2010-11 (Edition 2). 1 map, scale 1:100,000.

- Gordey, S.P., and Roots, C.F. 2011. Chapter 2. Regional Setting. *In* Geology of the central Mackenzie Mountains of the Canadian Cordillera, Sekwi Mountain (105P), Mount Eduni (106A), and northwestern Wrigley Lake (95M) map-areas, Northwest Territories. *Edited by* E. Martel, E.C. Turner, and B.J. Fischer. NWT Special Volume 1, NWT Geoscience Office, p. 18 to 30.
- Grew, E.S. 2002. Mineralogy, Petrology and Geochemistry of Beryllium: An Introduction and List of Beryllium Minerals. *In* Beryllium: Mineralogy, Petrology, and Geochemistry. *Edited by* E.S. Grew. *Reviews in Mineral Geochemistry*, **50**: 1-76.
- Groat, L.A., Giuliani, G., Marshall, D., and Turner, D. 2007. Chapter 3: Emerald. *In* Geology of Gem Deposits, Short Course 37. *Edited by* L.A. Groat. Mineralogical Association of Canada, Yellowknife, Northwest Territories, p. 79-109.
- Klein, C., and Beukes, N.J. 1993. Sedimentology and geochemistry of the glaciogenic Late Proterozoic Rapitan iron-formation, Canada. *Economic Geology*, **88**: 542-565.
- Lentz, D.R. 2003. Geochemistry of sediments and sedimentary rocks: historical to research perspectives. *In* Inorganic Geochemistry of Sediments and Sedimentary Rocks: Evolutionary Considerations to Mineral Deposit-Forming Environments. *Edited by* D.R. Lentz. Geological Association of Canada, GeoText 4, p. 1-6.
- MacNaughton, R.B., Fallas, K.M., and Zantvoort, W. 2008. Qualitative Assessment of the Plateau Fault (Mackenzie Mountains, NWT) as a conceptual hydrocarbon play. Geological Survey of Canada, Open File 5831, 29 p.
- Leslie, C.D. 2009. Detrital zircon geochronology and rift-related magmatism: Central Mackenzie Mountains, Northwest Territories. MSc. thesis. Department of Earth and Ocean Sciences, University of British Columbia, Vancouver, BC.
- Lund, K. 2008. Geometry of the Neoproterozoic and Paleozoic rift margin of western Laurentia: Implications for mineral deposit settings. *Geosphere*, **4**(2): 429-444.
- Martel, E., MacNaughton, R.B., and Fischer, B.J. 2011. Chapter 6. Metamorphism and Thermal Maturity. *In* Geology of the central Mackenzie Mountains of the Canadian Cordillera, Sekwi Mountain (105P), Mount Eduni (106A), and northwestern Wrigley Lake (95M) map-areas, Northwest Territories. *Edited by* E. Martel, E.C. Turner, and B.J. Fischer. NWT Special Volume 1, NWT Geoscience Office, p. 251 to 254.
- Mercier, M. 2008. Geology and mineralogy of the Mountain River Beryl (variety emerald) showing, Mackenzie Mountains, Northwest Territories, Canada. B.Sc. thesis, Department of Earth Sciences, University of Ottawa, Ottawa, ON.
- Morris, G.A., and Nesbitt, B.E. 1998. Geology and timing of palaeohydrogeological events in the Mackenzie Mountains, Northwest Territories, Canada. *In* Dating and Duration of Fluid Flow and Fluid-Rock Interaction. *Edited by* J. Parnell. Geological Society, London, Special Publications, v. 144, p. 161-172.

- Nelson, J., Paradis, S., Christensen, J., and Gabites, J. 2002. Canadian Cordilleran Mississippi Valley-Type deposits: A case for Devonian-Mississippian back-arc hydrothermal origin. *Economic Geology*, **97**: 1013-1036.
- Ootes, L., Fischer, B.J., Rasmussen, K.L., Borkovic, B., Long, D.F., and Gordey, S. P. 2011. Chapter 7. Mineral Deposits and Prospects. In *Geology of the central Mackenzie Mountains of the Canadian Cordillera, Sekwi Mountain (105P), Mount Eduni (106A), and northwestern Wrigley Lake (95M) map-areas, Northwest Territories*. Edited by E. Martel, E.C. Turner, and B.J. Fischer. NWT Special Volume 1, NWT Geoscience Office, p. 255 to 268.
- Ootes, L., Gleeson, S.A., Turner, E., Rasmussen, K., Gordey, S., Falck, H. Martel, E., and Pierce, K. Metallogenic evolution of the Mackenzie and eastern Selwyn mountains of Canada's northern Cordillera, Northwest Territories: A compilation and review. *Geoscience Canada*, *in press*.
- Ottaway, T.L., Wicks, F.J., Bryndzia, L.T., Kyser, T.K., and Spooner, E.T.C. 1994. Formation of the Muzo hydrothermal emerald deposit in Colombia. *Nature*, **369**(6481): 552-554.
- Rainbird, R.H., Heaman, L.M., and Young, G. 1992. Sampling Laurentia: Detrital zircon geochronology offers evidence for an extensive Neoproterozoic river system originating from the Grenville Orogen. *Geology*, **20**: 351-354.
- Rasmussen, K.L., Mortensen, J.K., and Falck, H. 2006. Geochronological and lithogeochemical studies of intrusive rocks in the Nahanni region, southwestern Northwest Territories and southeastern Yukon. *In Yukon Exploration and Geology 2005*. Edited by D.S. Emond, G.D. Bradshaw, L.L. Lewis and L.H. Weston. Yukon Geological Survey, p. 287-298.
- Ross, G.M. 1991. Tectonic setting of the Windermere Supergroup revisited. *Geology*, **19**: 1125-1128.
- Schwarz, D., and Giuliani, G. 2001. Emerald deposits – A review. *Australian Gemologist*, **21**: 17-23.
- Turner, D., and Groat, L.A. 2007. Chapter 4: Non-emerald gem beryl. In *Geology of Gem Deposits, Short Course 37*. Edited by L.A. Groat. Mineralogical Association of Canada, Yellowknife, Northwest Territories, p. 79-109.
- U.S. Geological Survey. 2012. Mineral commodity summaries 2012: U.S. Geological Survey, 198 p. <http://minerals.usgs.gov/minerals/pubs/mcs/2012/mcs2012.pdf>
- Walton, L. 2004. Exploration criteria for coloured gemstone deposits in the Yukon. Yukon Geological Survey, Open File 2004-10. 184 p.
- Zachovay, M. 2002. What is the Price of an Emerald? *In extraLapis English No. 2: Emeralds of the World*. Edited by G. Giuliani, M. Jarnot, G. Neumeier, T. Ottaway, J. Sinkankas, and G. Staebler. Lapis International, LLC, East Hampton, CT, USA. p. 93-96.

2. Petrography

2.1. Host rocks and alteration

Rocks of the Twitya Formation hosting veins at the MRB occurrence consist of thinly laminated mudstone to siltstone, massively bedded gritty sandstone, and massively bedded sandy dolostone (Fig. 2-1). These rocks are often weakly to moderately and pervasively altered by carbonate minerals, mostly dolomite. Carbonate alteration is composed of rhombic dolomite (0.2 to 2 mm in diameter) overprinting fine grained siliciclastic sediment or dolostone (Fig. 2-1d), or of interstitial dolomite between coarser grained sediment. Euhedral pyrite with pyritohedral crystal form and subhedral pyrite up to 2 mm in diameter often occurs overprinting or intergrown with carbonate (Fig. 2-2). The host rocks are commonly fractured or jointed, and very poorly developed veins of either pyrite or quartz are found along the edges of some fractures. Locally, grain size reduction and carbonate alteration is pronounced proximal to vein edges (Fig. 2-3), particularly where the veins are greater than a centimeter wide. This alteration appears as a bleached zone in hand sample. Bulk rock geochemical analyses of the unaltered host rocks show they are somewhat enriched in Be and transition metals, particularly Sc and V, compared to normal continental crust, greywacke, and shale (Appendix B Table B-1; Lentz 2003).

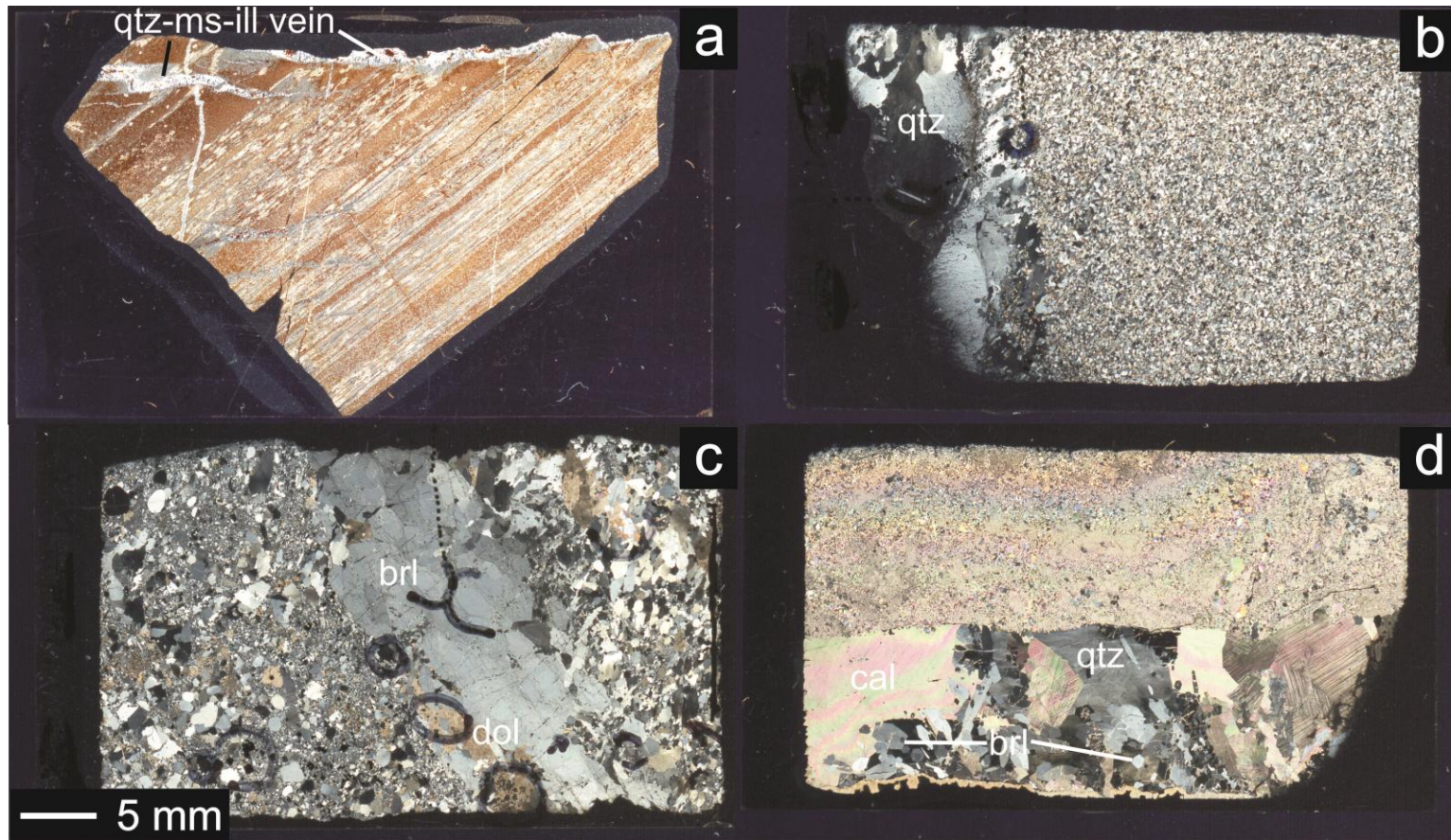


Figure 2-1. Representative scanned thin sections of host rock textures and alteration styles. Samples a) 10mh18Ai, showing thinly laminated siltstone cut by thin veinlets of quartz (qtz), muscovite (ms), and illite (ill); b) 10mh09Ai, a massively bedded fine-grained sandstone with weak dolomite alteration cut by a massive quartz-beryl vein; c) 10mh11Ai, gritty sandstone with weak dolomite (dol) alteration, cut by beryl (brl)-dolomite vein; d) 10mh12Ai, strongly dolomitized sandy dolostone cut by quartz-beryl-calcite (cal) vein. Images taken in cross-polarized transmitted light.

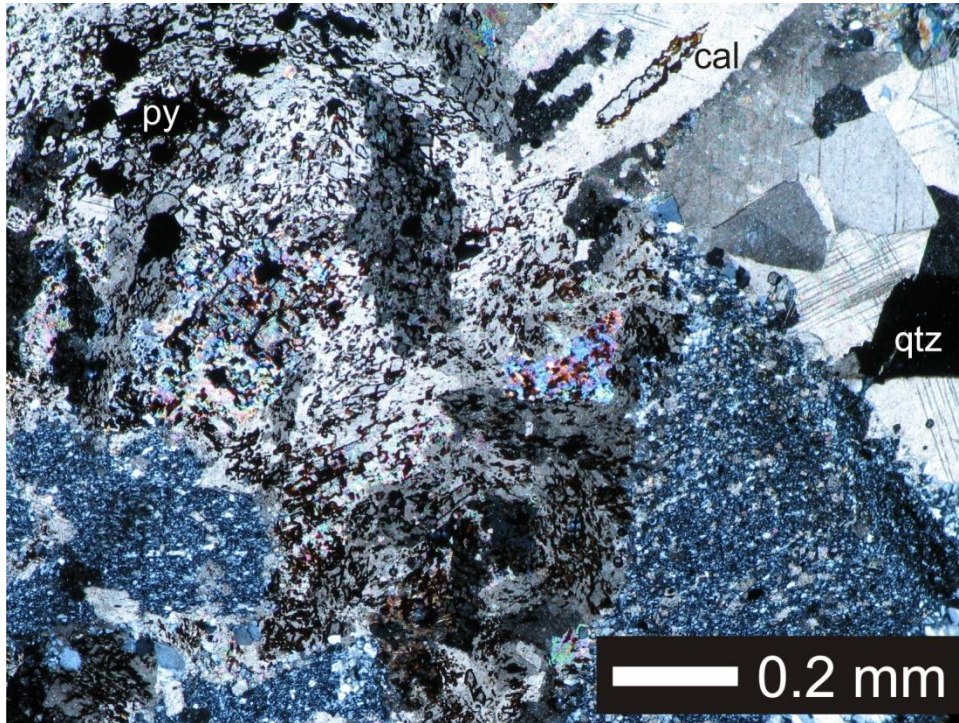


Figure 2-2. Subhedral pyrite (py) is intergrown with calcite alteration within the fine-grained carbonatized siltstone host rock proximal to a calcite (cal) and quartz (qtz) vein (upper right). Sample 10mh19Di.

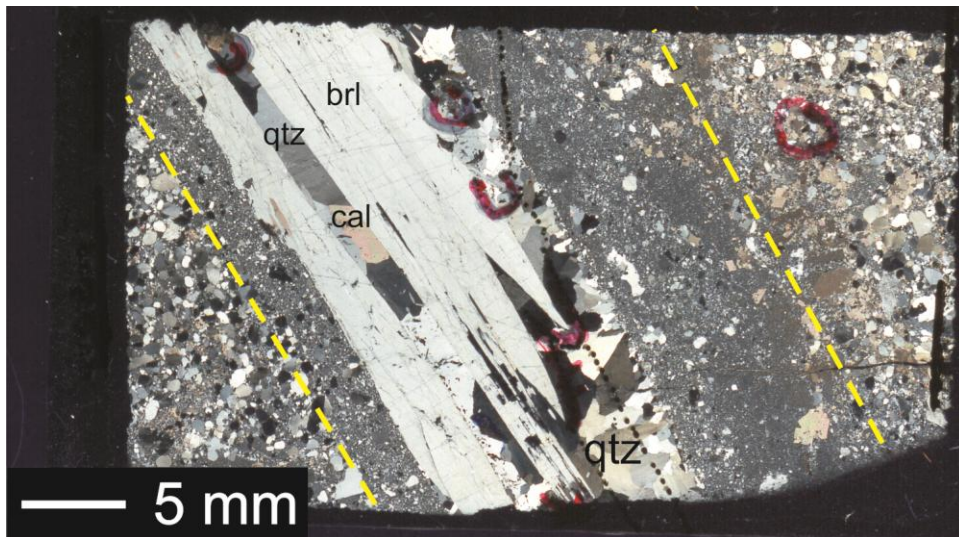


Figure 2-3. A zone of grain size reduction and carbonate alteration (dashed yellow line) is pronounced near to vein edges in some samples. Sample 10mh11Avii.

2.2. Beryl-bearing veins

The MRB occurrence consists of quartz, carbonate, and quartz-carbonate extensional veins hosting fractured milky green beryl and rare gem-quality emerald. Veins generally vary in width between several millimeters to 10 cm wide. Not all veins contain beryl, but of those that do, beryl accounts for between 10 to 90% of the vein. Crystal habits of beryl are of typically euhedral and hexagonal well-formed individual crystals, or needle-like beryl in clusters or radiating masses (Fig. 2-4), and beryl crystals are almost always severely fractured. Many of the crystals show distinct rounded cores encircled by thick euhedral, hexagonal rims (Fig. 2-4b). Some crystals show dissolution textures around their cores (Fig. 2-4c). The beryl shows very weak red luminescence and zoning under cathodoluminescence (CL) where the rounded cores are relatively highly luminescent and surrounded by thin oscillatory growth zones (Fig. 2-5). More detail on beryl petrography, CL, zonation, and crystal chemistry is given in Chapter 3.

The two other major vein constituents at the occurrence are quartz and carbonate. Quartz is milky white in hand sample and is massive or anhedral. Quartz is interstitial to beryl, carbonate, and other vein minerals. In some veins, quartz shows strain in the form of micro-kinking (Fig. 2-6), where the structures are filled with cryptocrystalline quartz and carbonate. Carbonate in the veins is anhedral to rhombic, with compositions dominated by dolomite and reddish-brown weathering ankerite (with minor surface replacement by limonite). Minor amounts of ferroan dolomite and magnesian siderite were confirmed by energy dispersive X-ray spectroscopy (EDS) equipped to a scanning electron microscope (SEM). Calcite is observed filling fractures in quartz and beryl (Fig. 2-4b), and post dates vein crystallization.

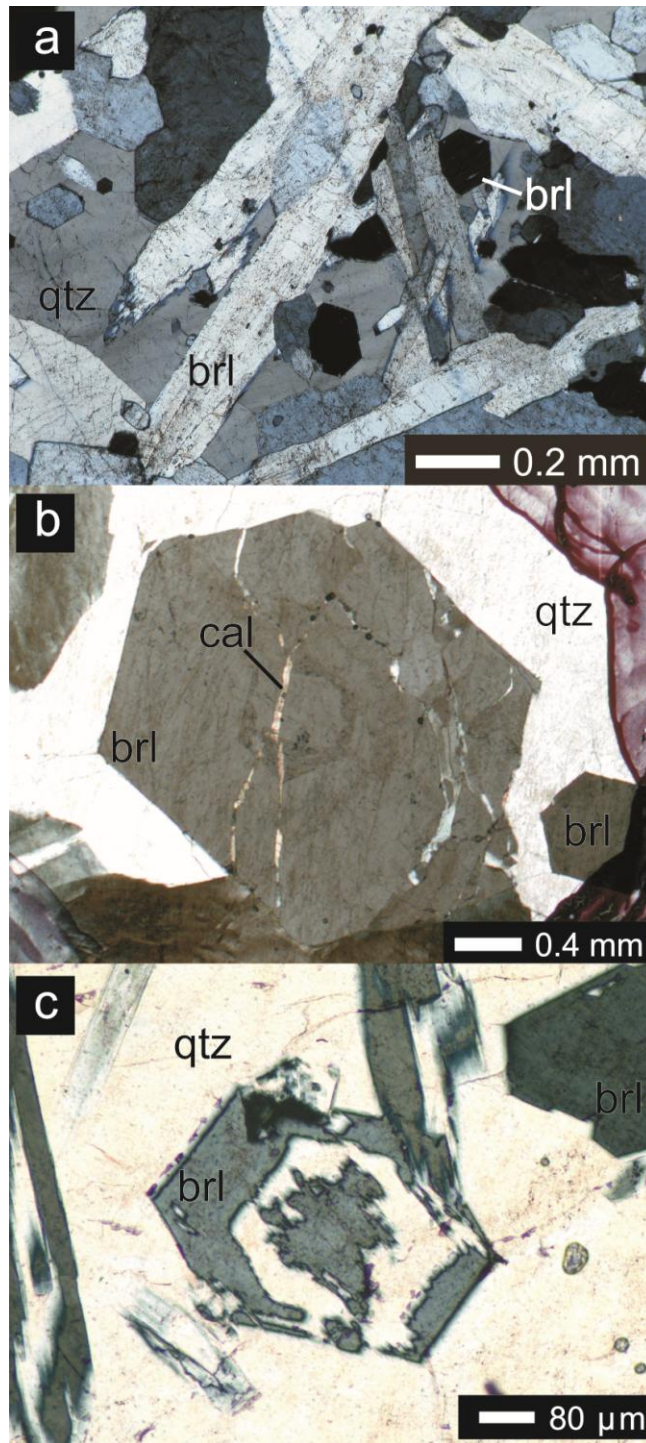


Figure 2-4. *Typical textures of beryl in thin section: a) massive intergrown needles, sample 10mh01Ai; b) individual euhedral, hexagonal crystals, sample 10mh11Aviii; c) euhedral crystals with dissolution and replacement by quartz around core and outer rim, sample 10mh15Ai. Images taken in cross polarized transmitted light.*

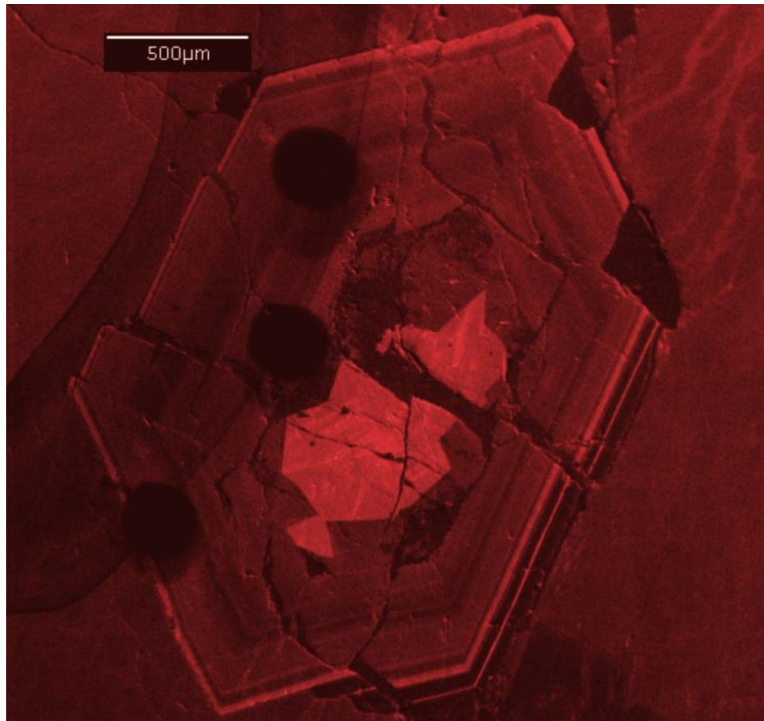


Figure 2-5. *Red luminescence in a fractured zoned beryl crystal. A highly luminescent core surrounded by oscillatory zonation in a wide rim is visible in scanning electron microscopy using wavelength filtered CL. Sample 10mh01Ai.*

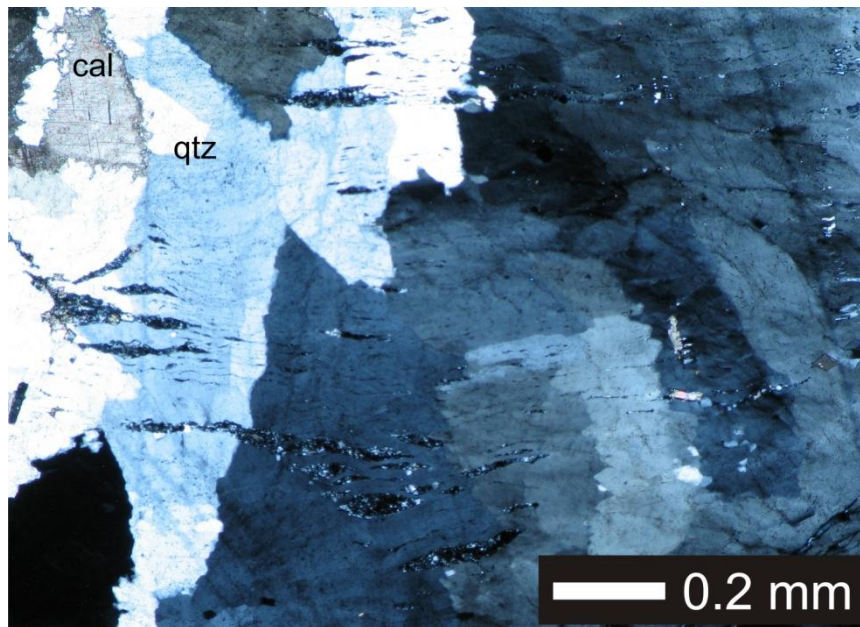


Figure 2-6. *Quartz in the veins shows strain in the form of micro-kinking filled by cryptocrystalline calcite (cal) and quartz (qtz). Sample 10mh19Di. Image taken in cross polarized transmitted light.*

Trace minerals in the veins include pyrite, albite, rutile, and biotite. Pyrite is rusty-weathering, generally euhedral with pyritohedron crystal form, and is associated with beryl and quartz. It occurs more commonly in quartz veins than in carbonate veins. In hand sample, a pyrite crystal within beryl indicates pyrite precipitation was largely coeval with beryl. Pyrite may be zoned in backscatter electron (BSE) images, with rounded cores and pyritohedral rims (Fig. 2-7). Small rounded inclusions of a silver-bearing sulphide mineral (approximate formula of $\text{Ag}_2\text{Fe}_6\text{S}_{17}$; possibly argentopyrite) are observed in the rims of pyrite. Trace amounts of end-member albite (Mercier 2008), generally too small to see in hand sample, occur in beryl-bearing veins. It is more abundant where beryl mineralization is minimal or absent and tends to occur more often along vein edges and in very thin veinlets. Rutile occurs in vein quartz and as inclusions in the outer rims of beryl (Fig. 2-8). Small flakes of biotite were only observed in one vein (sample 10mh01Ai), but not observed anywhere else.

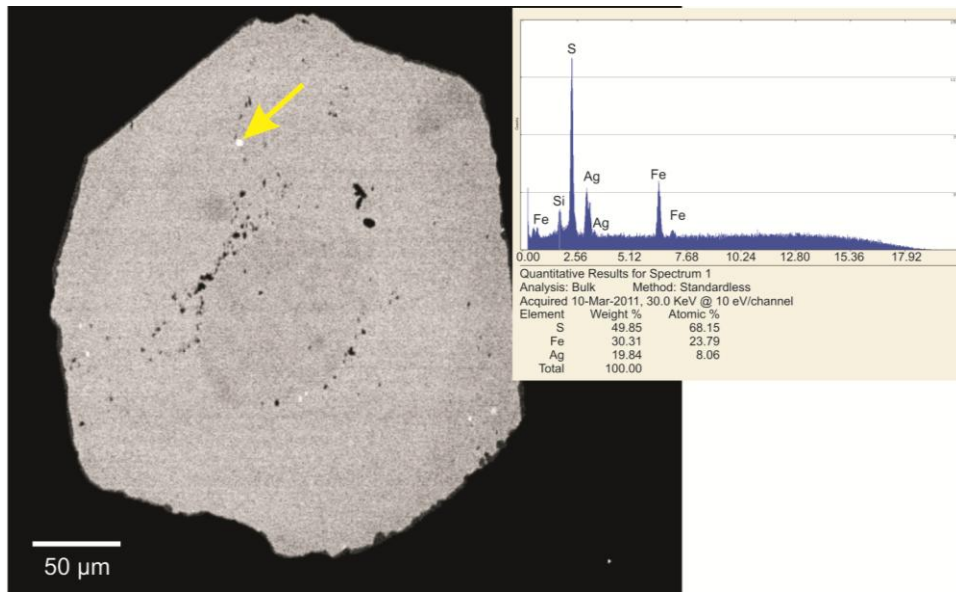


Figure 2-7. Zoned pyrite with rounded core and pyritohedral rim. Mineral inclusions (yellow arrow) were identified as a silver-bearing iron sulphide with an approximate formula of $\text{Ag}_2\text{Fe}_6\text{S}_{17}$. Sample MM2.

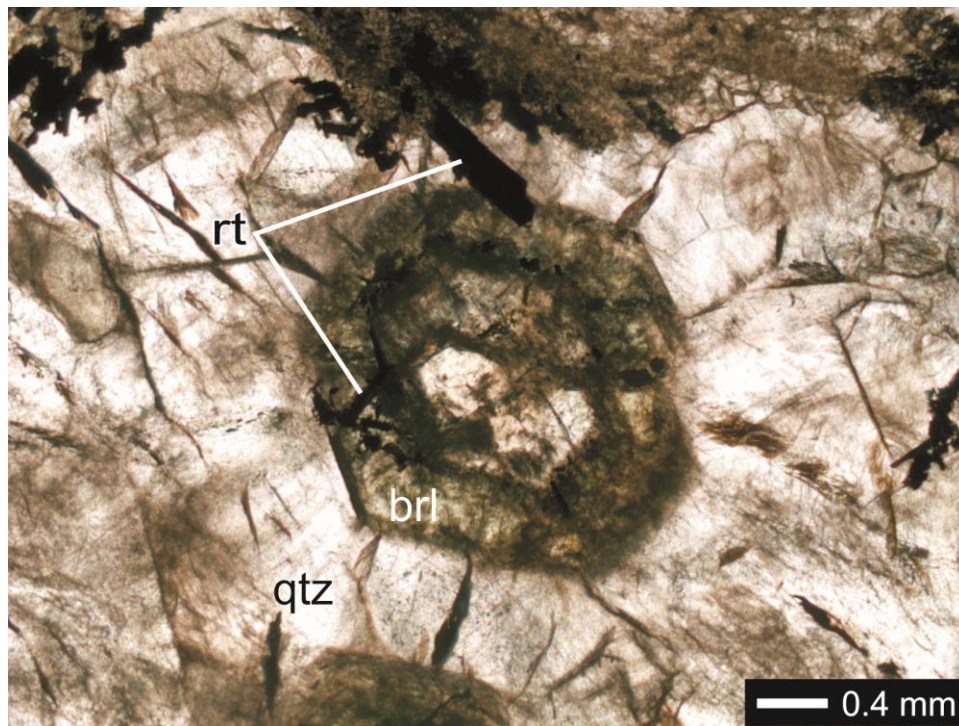


Figure 2-8. Rutile inclusions in zoned beryl. Sample 10mh11Av. Image taken in plane polarized transmitted light.

2.3. Beryl-free veins

Beryl-free quartz, carbonate, and quartz-carbonate veins mineralogically similar and texturally identical to beryl-bearing veins are present at the MRB occurrence. These veins are mostly found in the siltstone and mudstone beds of the Twitya Formation. Dolomite and rusty brown-weathering ankerite are the predominant carbonate minerals, with minor amounts of ferroan dolomite. Albite occurs in greater abundance in these veins than in beryl-bearing veins, and is blue-violet in colour. Albite tends to be concentrated along vein edges in contact with the host rock. Rutile is fine grained, euhedral and associated with quartz and albite. Pyrite is generally absent from beryl-free veins.

Quartz-green muscovite-illite veinlets at the MRB are also beryl-free (Fig. 2-1a), and are typically 0.5 to 3 mm wide. These veins are compositionally zoned with quartz along vein edges and muscovite and illite confined to vein centres. These veinlets cut quartz-carbonate veins and also cross-cut other quartz-muscovite-illite veinlets.

2.4. Summary and discussion

The paragenetic sequence of veins and alteration at the MRB (Fig. 2-9), as interpreted from petrographic observations, reflects the occurrence of two stages of beryl mineralization that were the result of two immediately successive pulses of hydrothermal fluid. Beryl precipitated early in the sequence, and was accompanied by the precipitation of trace pyrite in the veins and host rocks. Albite precipitation likely began late in stage I, but this is difficult to verify since no observations of albite in relation to beryl or pyrite were made. This interpretation assumes albite is the stable aluminous phase produced when the Be content of the mineralizing fluid is too low to crystallize beryl. Rutile precipitation began at the end of stage I or early in stage II and continued to the end of stage II. Carbonate (dolomite and ankerite) and quartz precipitation began in stage II, and quartz precipitation continued to the end of vein mineralization. Recrystallization of quartz occurred in deformational microkinks along with calcite, which also occurs in fractures cutting quartz and beryl, and post-dates vein mineralization.

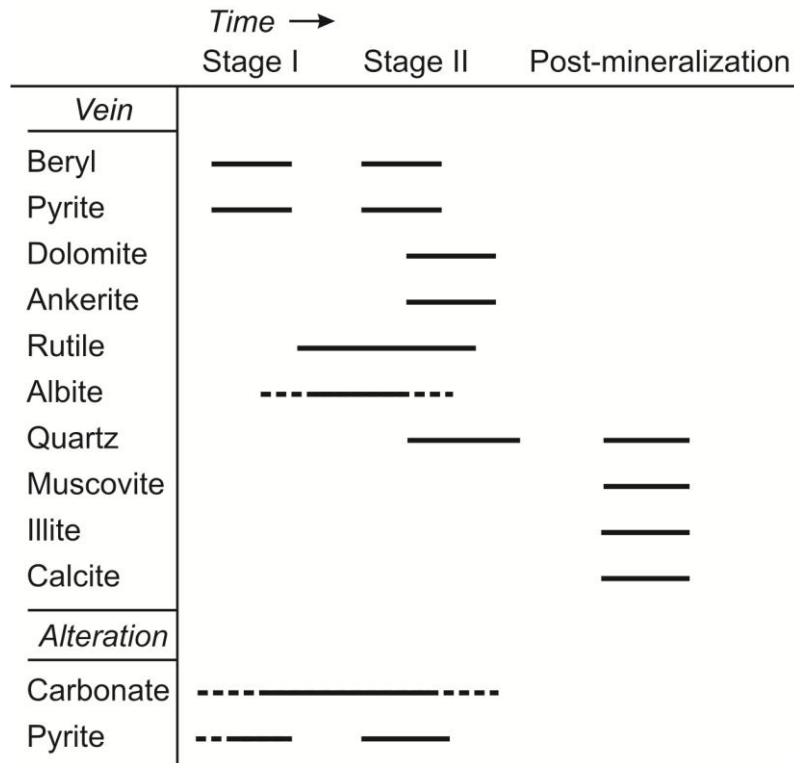


Figure 2-9. Paragenetic sequence of vein and host rock alteration minerals.

The presence of localized bleaching adjacent to veins related to carbonate alteration suggests leaching of elements from and/or into the host rocks. Unaltered rocks of the host Twitya Formation are two to seven times more enriched in Be and two to nine times more enriched in transition metals compared to normal continental crust, greywacke, and shale (Appendix B Table B-1; Lentz 2003). The elevation of these metals indicates that the host rocks are the most likely source of the components required for the mineralization of beryl and emerald, and beryl mineralization is therefore related to the in situ leaching and mobilization of cations. The same situation may be true for rocks of the older and stratigraphically lower Rapitan, Coates Lake, Little Dal, and Katherine groups (Fig. 1-3, Fig. 1-4). Fluids involved in beryl mineralization may have been sourced from and/or interacted with this entire package of rocks, leaching and mobilizing elements. The sedimentary provenance of these rocks best explains their enrichment in Be, which tends to be fractionated into plutons and pegmatites. The Neoproterozoic sediments of the Mackenzie Mountains were deposited via continental scale river systems sourcing pluton-rich cratons, orogenic belts, and ancient magmatic arcs of central and eastern Laurentia (Rainbird et al. 1992; Leslie 2009).

The zonation of both beryl and pyrite into distinct rounded cores and thick euhedral rims indicates that at least two stages of mineralization (stages I and II; Fig. 2-9), and therefore fluid pulse stages, occurred in relatively quick succession. The zonation indicates complex metal substitutions (Al, V, Fe, Sc, Cr, and Ti in beryl, and Fe and Ag in pyrite) over crystal growth histories, reflecting changes in fluid conditions over time as vein crystallization progressed. The observation that albite is more abundant in veins lacking beryl indicates that changes in fluid chemistry and conditions were also occurring spatially, and not just temporally. Where Be was abundant in the mineralizing fluid, beryl was able to crystallize. However, as Be contents diminished towards the edges of the mineralizing system, the stable aluminous phase became albite (Turner and Groat 2007). More detail on beryl crystal chemistry and growth history is given in Chapter 3.

The deformation of beryl and quartz, respectively as fractures and microkinks filled by calcite and quartz, indicate post-mineralization brittle deformation. These fractures and microkinks are interpreted to indicate that a later episode of movement, which post-dates beryl mineralization, fractured and deformed the veins. This episode of deformation may have occurred during Cretaceous-Tertiary movement along the Shale Lake fault. The presence of veins in the hanging wall of the Shale Lake fault may be evidence that it is related to an older, perhaps reactivated, fault originally formed prior to the Mesozoic. Other long-lived reactivated structures throughout the Mackenzie Mountains have been documented (Turner and Long 2008), and younger structures have been postulated to have been influenced by the architecture of older faults, folds, and basin geometry (Gordey and Roots 2011). It is not unlikely that the Shale Lake fault, which has been interpreted to have formed during Cretaceous-Tertiary deformation, may have taken advantage of or been influenced by the propagation of an older structure at depth (i.e., Mackenzie Arch and associated faults; Gordey et al. 2011). This older structure may well have been a conduit for fluid flow resulting in mineralization at the MRB occurrence.

References

- Gordey, S.P., and Roots, C.F. 2011. Chapter 2. Regional Setting. *In* Geology of the central Mackenzie Mountains of the Canadian Cordillera, Sekwi Mountain (105P), Mount Eduni (106A), and northwestern Wrigley Lake (95M) map-areas, Northwest Territories. *Edited by* E. Martel, E.C. Turner, and B.J. Fischer. NWT Special Volume 1, NWT Geoscience Office, p. 18 to 30.
- Gordey, S.P., Macdonald, J.D., Turner, E.C., and Long, D.G.F. 2011. Chapter 5. Structural Geology of the Mackenzie Mountains. *In* Geology of the central Mackenzie Mountains of the Canadian Cordillera, Sekwi Mountain (105P), Mount Eduni (106A), and northwestern Wrigley Lake (95M) map-areas, Northwest Territories. *Edited by* E. Martel, E.C. Turner, and B.J. Fischer. NWT Special Volume 1, NWT Geoscience Office, p. 215 to 250.
- Lentz, D.R. 2003. Geochemistry of sediments and sedimentary rocks: historical to research perspectives. *In* Inorganic Geochemistry of Sediments and Sedimentary Rocks: Evolutionary Considerations to Mineral Deposit-Forming Environments. *Edited by* D.R. Lentz. Geological Association of Canada, GeoText 4, p. 1-6.
- Leslie, C.D. 2009. Detrital zircon geochronology and rift-related magmatism: Central Mackenzie Mountains, Northwest Territories. MSc. thesis. Department of Earth and Ocean Sciences, University of British Columbia, Vancouver, BC.
- Mercier, M. 2008. Geology and mineralogy of the Mountain River Beryl (variety emerald) showing, Mackenzie Mountains, Northwest Territories, Canada. B.Sc. thesis, Department of Earth Sciences, University of Ottawa, Ottawa, ON.
- Rainbird, R.H., Heaman, L.M., and Young, G. 1992. Sampling Laurentia: Detrital zircon geochronology offers evidence for an extensive Neoproterozoic river system originating from the Grenville Orogen. *Geology*, **20**: 351-354.
- Turner, D., and Groat, L.A. 2007. Chapter 4: Non-emerald gem beryl. *In* Geology of Gem Deposits, Short Course 37. *Edited by* L.A. Groat. Mineralogical Association of Canada, Yellowknife, Northwest Territories, p. 79-109.
- Turner, E.C., and Long, D.G.F. 2008. Basin architecture and syndepositional fault activity during deposition of the Neoproterozoic Mackenzie Mountains supergroup, Northwest Territories, Canada. *Canadian Journal of Earth Sciences*, **45**: 1159-1184.

3. Cathodoluminescence of Al zoning in a Colombian-style beryl and emerald occurrence: Implications for geochemical fingerprinting and growth history*

M. L. Hewton

Department of Earth Sciences, Simon Fraser University

8888 University Drive, Burnaby, BC, V5A 1S6

D. D. Marshall

Department of Earth Sciences, Simon Fraser University

8888 University Drive, Burnaby, BC, V5A 1S6

L. Ootes

Northwest Territories Geoscience Office

Box 1500, Yellowknife, NT, X1A 2R3

* Submitted to *American Mineralogist* and reproduced here (including acknowledgements and references) as Chapter 3.

3.1. Abstract

Milky green beryl and rare gem quality emerald occur near the Mountain River, Northwest Territories, Canada, and are hosted in quartz-carbonate veins that cross-cut Neoproterozoic sandstones and siltstones. Emerald formed in a manner similar to the Colombian-style emerald mineralization model via sulfate reduction. The crystals show brightly luminescent cores and oscillatory zonation in cathodoluminescence (CL) imaging, but zoning is not observed via secondary or backscattered electron detectors. Electron microprobe analysis indicates that CL zonation arises from variations in the concentration of transition metals substituting for aluminum at the octahedral site. Aluminum concentration generally decreases from core to rim, and is accompanied by an increase in transition metals and alkalis from core to rim. Similar to other studies using quartz, this study of beryl indicates that higher CL intensity zones are the result of increased aluminum concentrations, while quenching of luminescence is related to transition metal substitutions, especially ferric iron. This finding is in contrast to previous studies of beryl which report increasing CL intensity to be related only to chromium and vanadium. Microprobe analyses demonstrate the unique high-scandium, high-vanadium, low-chromium crystal chemistry for emerald from Mountain River relative to other emerald globally. Raman analysis of water molecule vibration indicates that the majority of water present in the crystal channels is of the type II variety, oriented with symmetry axis parallel to the crystal *c*-axis, and reflects the high sodium content of these crystals. These combined chemical properties provide a unique signature of the geographic and geologic origin of the Mountain River beryl crystals.

Keywords: emerald, beryl, cathodoluminescence, Raman spectroscopy, zonation

3.2. Introduction

Beryl is an aluminosilicate mineral with a cyclosilicate crystal structure produced by stacks of aluminum octahedra and beryllium tetrahedra alternating with rings of silicon tetrahedra that form hollow channels along the crystal *c* axis (Deer et al. 1966). Beryl has an ideal chemical formula of $\text{Be}_3\text{Al}_2\text{Si}_6\text{O}_{18}$ but, due to the ease of substitution at the octahedral and tetrahedral sites, is better described by the formula $(\text{Be}_{3-X}, \text{Li}_Y, \text{X}^+)_Y(\text{Al, Fe, Cr, V, Sc, Ga})^{3+}_{2-Z}(\text{Fe, Mg, Mn})^{2+}_Z\text{Si}_6\text{O}_{18} \cdot (\text{Na, K, Rb, Cs})_{2X-Y+Z}(\text{H}_2\text{O, He, Ar})_{\leq 2-(2X-Y+Z)+\text{Na}}$ where $(Y \leq 2)$, $(X \geq Y)$, $(Z < 2)$, and $(2X - Y + Z)$, and Na, K, Rb, Cs, H_2O , He, and Ar may occupy vacancies at channel sites parallel to the crystal's *c* axis (Fig. 3-1; Turner and Groat 2007). Water present within the channel sites may constitute up to 2.5 weight % of the crystal and, being a polar molecule, may exist in one of two orientations: either as free H_2O oriented so that its molecular symmetry axis is perpendicular to the crystal *c* axis (type I), or as H_2O associated with an alkali cation (type II; Fig. 3-1b) and oriented with its molecular symmetry axis parallel to the crystal *c* axis (Wood and Nassau 1967). Different color varieties of gem-quality beryl are produced by the substitution of different chromophoric cations for Al^{3+} at the octahedral site. The substitution of Cr and/or V gives beryl a deep green color, and the gem is known as emerald. The extent of substitution of metal cations for Al at the octahedral site has made it possible for workers to discriminate the geographic locations of individual emerald occurrences worldwide based on crystal composition (Groat et al. 2008).

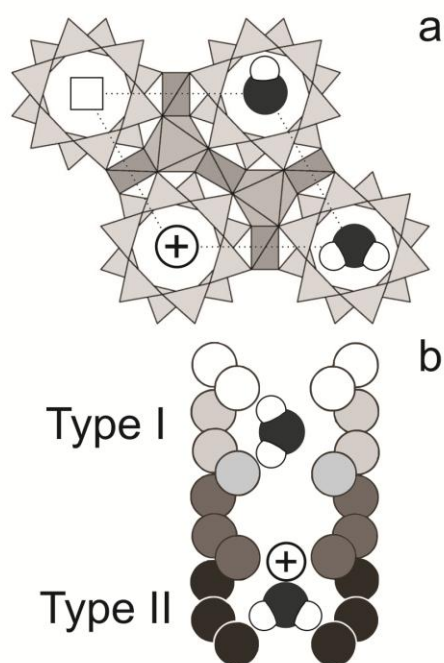


Figure 3-1. a) The cyclosilicate structure of beryl, viewed down the *c* axis, showing BeO₄ tetrahedra (dark grey), AlO₆ octahedra (medium grey), and rings of SiO₄ tetrahedra (light grey) which form hollow channels. Alkali cations (Na, K, Rb, Cs; + sign), water molecules, or vacancies (square) may exist at channel sites. Modified from Groat et al. (2008). b) Water molecules in channel sites exist either as free H₂O oriented so that its molecular symmetry axis is perpendicular to the crystal *c* axis (type I), or as H₂O associated with an alkali cation and oriented with its molecular symmetry axis parallel to the crystal *c* axis (type II). Modified from Wood and Nassau (1967).

Beryl commonly displays zonation patterns visible in hand sample, optical light microscopy, backscattered electron (BSE) imaging, and cathodoluminescence (CL). This zonation may reflect compositional variation or structural defects (Graziani et al. 1990; Beal and Lentz 2010; Loughrey et al. 2012; Marshall et al. 2012). Growth zones can also provide valuable information on the growth histories of crystals by revealing structures, dissolution surfaces and mineralization unconformities, overgrowths, and even crystal form growth rates (Vavra 1990; Shore and Fowler 1996). Cathodoluminescence in particular can often reveal more of these zonation details than optical microscopy or BSE imaging due to its high resolution and sensitivity to the presence of trace elements and crystal defects, and can be used in conjunction with a quantitative electron microprobe analysis (EMPA) to relate zonation and luminescence intensity to trace and minor element distributions (Lehmann et al. 2009). However, these correlations do not

equal causation, and the causes of CL activation are still poorly understood. The intensity of luminescence depends mainly on the concentration of impurities in the crystal lattice, but sorting out which impurities promote or suppress luminescence has proven difficult. Most authors using such tools together have focused on the feldspar minerals (Shore and Fowler 1996), quartz (Lehmann et al. 2009), or zircon (Vavra 1990). Few publications exist in which EMPA is used in conjunction with CL to map minor or trace element zonation in beryl (Beal and Lentz 2010; Marshall et al. 2012). Zoning in beryl observed with CL is largely associated with changes in concentrations of octahedral site Cr^{3+} , V^{3+} , and Fe^{2+} (Marshall et al. 2012). The concentrations of these metals vary as a result of different concentrations and conditions of the mineralizing fluid at subsequent stages of crystal growth.

Beryl is typically formed by the introduction of Be-rich fluids to Al-rich host rocks, and three deposit model types have been proposed in the literature for the formation of emerald (Schwarz and Giuliani 2001). Emerald commonly occurs where Be-rich pegmatitic intrusions interact with Cr(\pm V)-bearing mafic or schist host rocks (Type 1 deposit model), but also occurs in upper greenschist to amphibolite metasomatic environments (Type 2). The rarest type of emerald occurrence (Type 3) is typified by the world class deposits of Colombia (Schwarz and Giuliani 2001), which resulted from thermochemical sulphate reduction by reaction of hydrothermal brines with organic matter in black shale host rocks during Paleogene orogenesis (Ottaway et al. 1994; Giuliani et al. 2000).

Emerald near the Mountain River, western Northwest Territories, Canada, appears to have formed in a manner coincident with a modification of the Colombian-style emerald mineralization model (Hewton et al. in review). The unusual genesis of the emerald crystals prompts detailed study of their geochemical signature and growth history. Unraveling the growth history of the Mountain River beryl crystals may help to reveal fluctuations in fluid conditions during crystallization, and will contribute to the body of knowledge of mineral zonation, CL imaging, and Raman spectroscopy of beryl in general. This study particularly has applications for gemologists to help them identify the geographic source and genetic model of emerald and other gem quality beryl crystals.

3.3. Geologic setting and crystal petrography

The beryl and emerald at Mountain River occurs in quartz-carbonate extensional veins hosted in carbonate-altered sandstones and siltstones of the Neoproterozoic Windermere Supergroup in the Mackenzie Mountains. Cretaceous-Tertiary deformation produced a series of fold and thrust belts that resulted in the juxtaposition of the beryl-bearing Neoproterozoic rocks above Paleozoic limestones. A Re-Os isochron age of 345 ± 20 Ma has been determined for pyrite that crystallized contemporaneously with the beryl. Fluid inclusion observations and stable isotope data reveal that beryl formed from warm, metal-rich, basin-derived carbonic brines at temperatures of 380 to 415°C and pressures of 2.4 to 4.0 kbar, corresponding to depths of 9 to 15 km (Hewton et al. in review). These emeralds likely formed during the same massive fluid flow and mineralization event that produced the regionally extensive Manetoe Facies dolomite alteration (Morris and Nesbitt 1998; Al-Aasm et al. 2002) and hydrothermal base metal mineralization including some carbonate-hosted and sedimentary exhalative Zn-Pb deposits and volcanogenic massive sulphide occurrences throughout the northern Cordillera (Nelson et al. 2002; Nelson and Colpron 2007). These events were associated with the development of a back-arc basin and opening of the Slide Mountain Ocean along the western margin of Laurentia during the Late Devonian to Mississippian (Nelson et al. 2002; Nelson and Colpron 2007; Lund 2008). These events created a unique geological environment for beryl mineralization at Mountain River, making it geologically distinct from other emerald deposits.

The Mountain River beryl shares some similarities with the world-class emerald deposits of Colombia, such as its occurrence within sub-greenschist grade sedimentary host rocks and its formation from hydrothermal carbonic brines (Banks et al. 2000). However, the host black shales with cenicero alteration zones, organic thermochemical sulphate reduction, and direct genetic relationship to thrust faulting that characterize the Colombian emeralds (Ottaway et al. 1994) are absent at Mountain River. Instead, beryl-bearing veins are hosted in organic-poor sandstones, and inorganic sulphate reduction by iron-rich sediments (Ohmoto and Rye 1979) likely initiated beryl mineralization at Mountain River during a period dominated by crustal extension or transtension. Thus,

the Mountain River occurrence represents a variation of the Colombian-style emerald mineralization model in the northern Canadian Cordillera (Hewton et al. in review).

The beryl crystals commonly show weakly discernible rounded cores that are optically continuous with euhedral outer rims under optical light microscopy (Fig. 3-2), but are not visible under scanning electron microscopy (SEM) or BSE imaging. These characteristics make the beryl crystals ideal for study using EMPA in conjunction with panchromatic CL imaging to constrain the concentration and zonation of transition metals and accompanying monovalent alkali cations (Na, K, Cs) in the beryl.

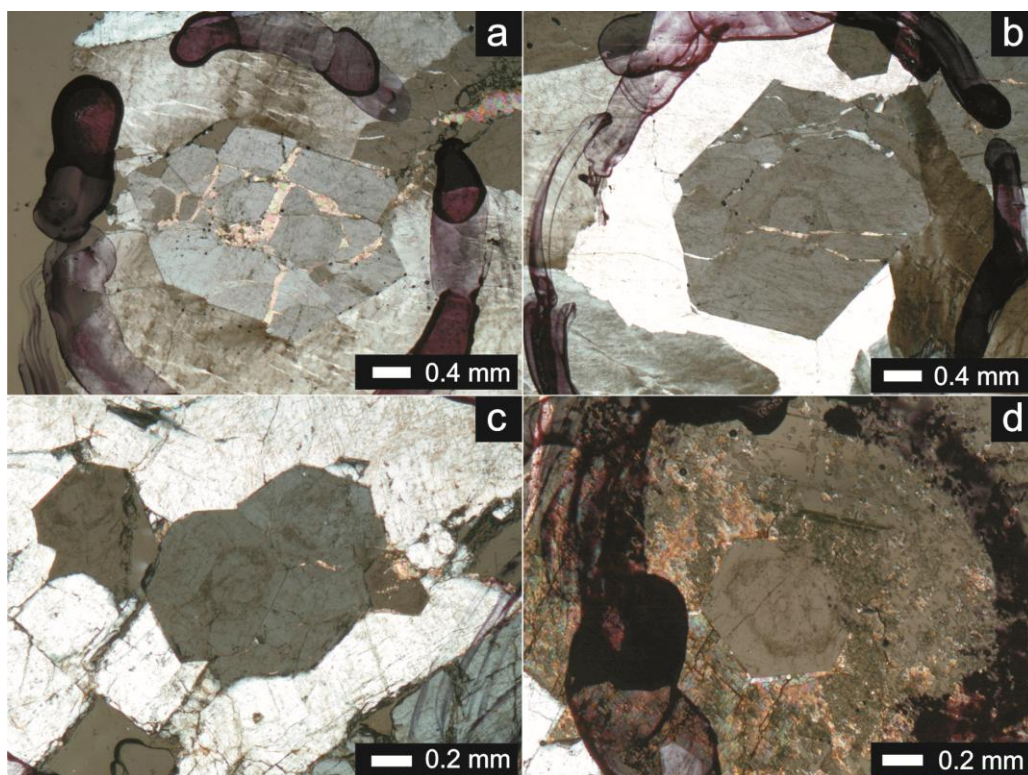


Figure 3-2. *Photomicrographs of the studied crystals showing zoned cores that are optically continuous with rims. Samples a) 01Ai-2, b) 01-Ai-3, c) 01Bi-5, and d) 01Bi-6. Images taken using cross-polarized transmitted light microscopy.*

3.4. Samples and analytical methods

3.4.1. Scanning electron microscopy and cathodoluminescence

Four euhedral hexagonal crystals oriented perpendicular to the crystal *c* axis were chosen for imaging. These crystals were hosted within quartz-carbonate vein material (Fig. 3-2). Two of these crystals were heavily fractured, with calcite fracture infill, while the other two crystals did not appear to be fractured. We interpret the entire growth history of these four crystals to be representative of the Mountain River occurrence.

Panchromatic CL and BSE imaging were carried out on carbon-coated polished thin sections of beryl using a Bausch and Lomb Nanolab LE 2100 scanning electron microscope equipped with BSE and CL detectors, and utilizing digital imaging 4pi

Spectral engine with Revolution software. The operating conditions were set to an accelerating voltage of 15 keV and sample current of 2.3 nA.

3.4.2. *Electron microprobe analysis*

Carbon-coated polished thin sections of the same beryl crystals imaged by CL were analysed on a fully automated CAMECA SX-50 microprobe operating in the wavelength-dispersion mode at the University of British Columbia. Analyses were conducted along set traverses across zonation of the crystals encompassing the maximum number of wider zones. Operating conditions were set to an excitation voltage of 15 kV, beam current of 20 nA, peak count time of 50s, and background count-time of 25s (20s Na, Al, Si peak count time, 10s background count-time), with a spot diameter of 10 μm . Data reduction was done using the 'PAP' $\phi(\rho Z)$ method (Pouchou and Pichoir 1985). For the elements considered, the following standards, X-ray lines and crystals were used: albite, $\text{NaK}\alpha$, $\text{AlK}\alpha$, $\text{SiK}\alpha$, TAP; diopside, $\text{MgK}\alpha$, TAP; diopside, $\text{CaK}\alpha$, PET; orthoclase, $\text{KK}\alpha$, PET; elemental Sc, $\text{Sc K}\alpha$, PET; rutile, $\text{TiK}\alpha$, PET; elemental V, $\text{VK}\alpha$, PET; synthetic magnesiochromite, $\text{CrK}\alpha$, LIF; synthetic rhodonite, $\text{MnK}\alpha$, LIF; synthetic fayalite, $\text{FeK}\alpha$, LIF; gahnite, $\text{ZnK}\alpha$, LIF; pollucite, $\text{CsL}\alpha$, PET.

3.4.3. *Raman spectroscopy*

Raman spectra of two beryl crystals, one rough crystal and one in thin section, were collected on a laser-excited Dilor LabRam spectrometer at Simon Fraser University which was equipped with optical microscope at room temperature using the 457.8 nm exciting line of an Ar ion laser, similar to the technique of Le Thi-Thu et al. (2010). Spectra were collected in the range of OH^- and water molecules (2800 to 4300 cm^{-1}). The instrument used a grating of 1800 grooves/mm, slit width of 200 μm , and collection time of 400 s. Peak analyses were performed with the Horiba-Jobin-Yvon LabSpec software and peak positions were checked periodically against silicon metal and corrected if required. The presence of type I and type II water in the crystal channels

was checked referencing the lines 3608 and 3598 cm^{-1} , respectively (Le Thi-Thu et al. 2010).

3.5. Results and discussion

3.5.1. *Backscattered electron and cathodoluminescence imaging*

Images of four beryl crystals were captured using BSE and panchromatic CL imaging. None of the crystals showed any discernible pattern in BSE, but showed bright unzoned, angular to sub-rounded, and anhedral cores surrounded by concentric euhedral oscillatory zoned rims in CL (Fig. 3-3). Red luminescence was observed during preliminary CL work, and although panchromatic CL was used for higher resolution imaging, all parts of the analysed beryl showed some degree of reddish luminescence. Cores are always the most luminescent part of the crystals, and rims are less bright. The innermost core of sample 01Bi-6 appears to have preserved a second, less luminescent zone that is slightly darker than the majority of the core and provides insight into the conditions of early crystal growth. The contact between the core and the first euhedral zone is sharp, irregular, and likely represents a growth unconformity formed by dissolution.

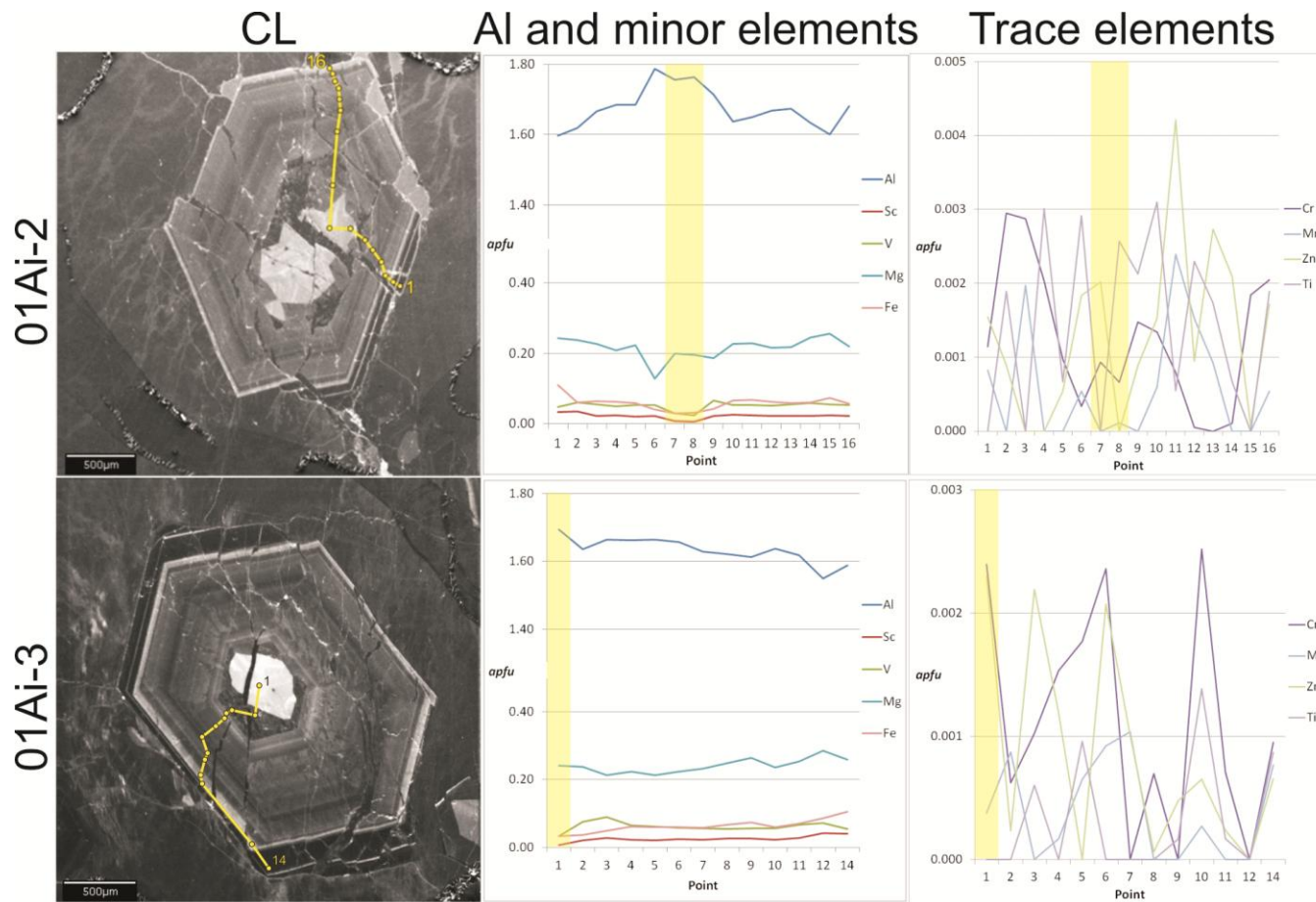


Figure 3-3. Panchromatic cathodoluminescence (CL) images of the crystals studied showing bright cores and outer oscillatory zoning. Traverse points are marked by yellow dots connected by yellow lines. Images in the first column are compared to their traverse points in element plots (in atoms per formula unit, apfu) for Al and minor elements (Sc, V, Mg, and Fe) in the second column, and trace elements (Cr, Mn, Zn, and Ti) in the third column. Yellow bars in the element plots indicate points analysed in the crystal cores.

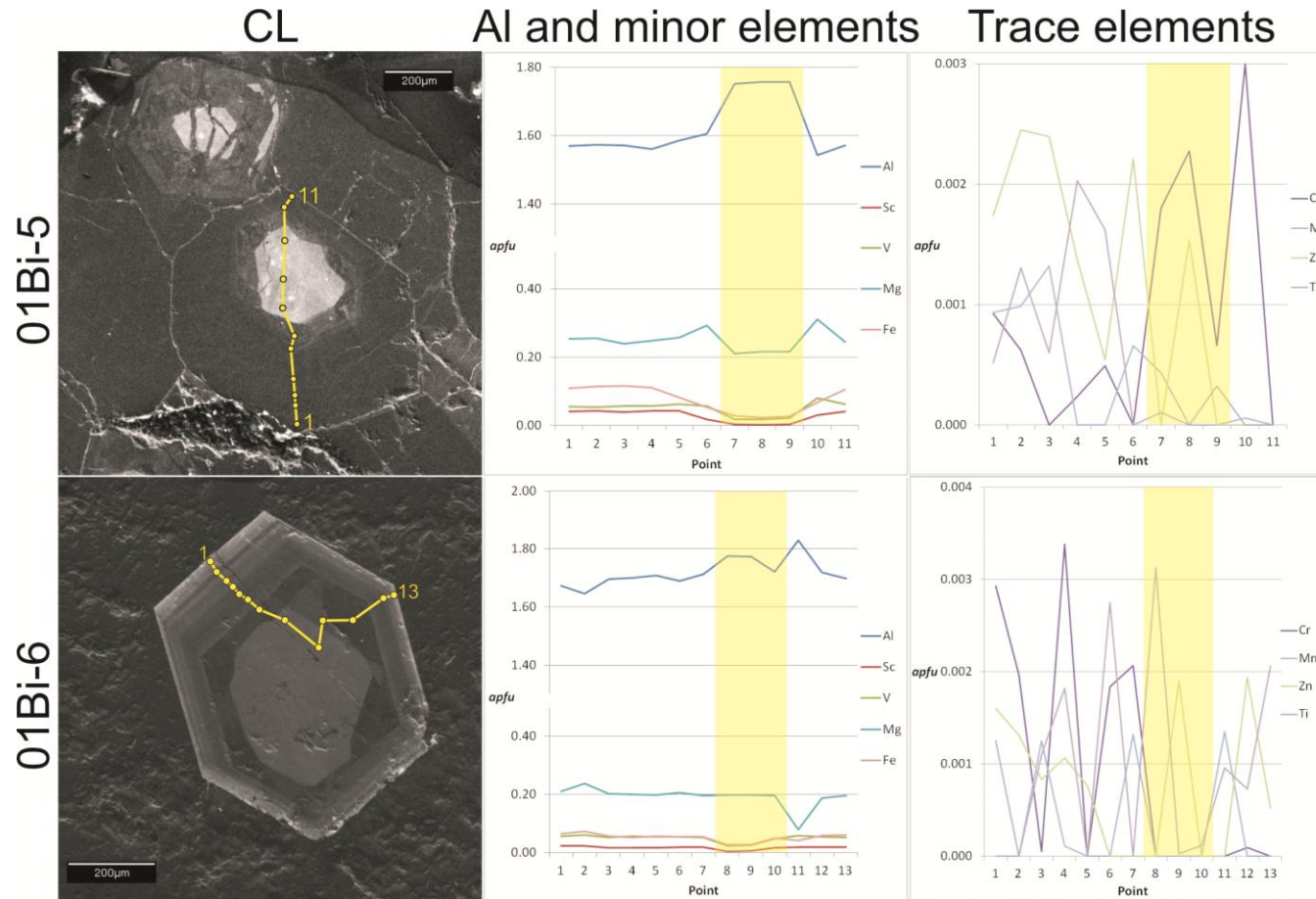


Figure 3-3. Continued.

Individual zones are several microns to 200 microns in width, and range in luminescence intensity from very dark (very little luminescence) to nearly as bright as their cores. Imaging shows samples 01Ai-2, 01Ai-3, and 01Bi-5 to have euhedral, hexagonal mantles surrounding the cores. These mantles are dark in CL and have a spotty or cellular texture. Sample 01Bi-6 also has a dark hexagonal mantle around its core, but the mantle has a solid monotonous texture and dark grey color. The general pattern of oscillatory zones is similar for samples 01Ai-2, 01Ai-3, and 01Bi-6 where dark mantles are overgrown by alternating bright and dark zones. The outermost zones of these crystals are very dark and overgrow a very bright zone. In sample 01Bi-6, however, this final dark rim is not present. In sample 01Bi-5, the width of the zoned area is less than 100 μm , and the outermost zone (100 to 400 μm wide) is a monotonous medium dark grey with no apparent textures or features.

Euhedral, hexagonal zones around anhedral, subangular cores indicate that at least two phases of beryl crystallization occurred and are separated by a period of dissolution. The first phase of growth appears to have produced crystals that were unzoned with monotonous textures. During the second phase of growth, the crystals maintained their euhedral shapes until the end of crystal growth, and zonation is oriented perpendicular to (0001). Cryptic sector overprinting of the inner oscillatory zones of sample 01Ai-3 may be indicative of strain during the early period of the second stage of crystal growth. It is unknown whether this strain was due to tectonic processes or the accumulation of point defects in the crystal structure.

3.5.2. *Electron microprobe analysis*

Electron microprobe traverses (Table 3-1) across zoned beryl crystals with corresponding CL images identify subtle patterns of cation enrichment and depletion (Fig. 3-3). The overall pattern shows a general decrease in Al content from the core (1.69 to 1.77 atoms per formula unit (apfu) Al) to the outermost rims (1.55 to 1.69 apfu Al), coupled with a general increase in the minor elements (Mg, Fe, V, Sc). Remarkably, EMPA analyses revealed that certain zones contain some of the highest concentrations of Sc, at 0.36 weight %, ever reported for emerald (Groat et al. 2008). Trace elements

(Cr, Mn, Zn, Ti) showed no discernible patterns across the traverses. The inverse relationship between Al and minor elements suggests the substitution of Al in the octahedral site by minor elements. This is supported by a nearly one-to-one inverse relationship between Al and minor element contents (Fig. 3-4a), as expected. Where divalent cations (Mg, Mn, Fe, Zn) substitute for Al (Fig. 3-4b), a comparable increase in the concentration of monovalent cations (Na, K, Cs) is also observed (Fig. 3-4c). The most abundant divalent cation, Mg, and the most abundant monovalent cation, Na, also have nearly identical distribution patterns (Fig. 3-3). The relationship suggests that, in order to achieve charge balance, the substitution of divalent cations for Al must be accompanied by the addition of a monovalent alkali in the channel site. However, the relationship deviates from a perfect one-to-one ratio towards higher concentrations of Mg+Mn+Fe+Zn. This deviation is most likely due to some of the Fe measured during analysis being present as Fe^{3+} occupying the Al octahedral site (Groat et al. 2007). Monovalent alkali ions trapped in the hollow *c*-axis channels balance ionic charge when divalent metal cations substitute for trivalent Al. Ideally, a 1:1 ratio of alkali to divalent metal is achieved by this substitution (Groat et al. 2007). Data points that lie below the 1:1 ratio line (Fig. 3-4c) indicate that some of the total Fe present in the crystal exists as Fe^{3+} , while data points that lie above the line indicate the substitution of Li^+ at the Be tetrahedral site (Groat et al. 2007). In the case of crystals from Mountain River, the majority of data points lie on or below the 1:1 line, indicating that little Li^+ , if any, is present and that some of the total Fe is present as Fe^{3+} . The presence of Fe^{3+} may act to quench CL intensity, as discussed previously. In any case, Na dominates the alkali component, even when compared to Na-rich emerald crystals from other occurrences, while the other alkali metals are generally below detection. Eliminating Fe entirely from the diagram produces a more precise one-to-one ratio (Fig. 3-4d), supporting the presence of some total Fe as Fe^{3+} as the cause of weak correlation.

Table 3-1. Compositions of zoned beryl determined from electron microprobe analysis.

Oxide %	01Ai-2-1	01Ai-2-2	01Ai-2-3	01Ai-2-4	01Ai-2-5	01Ai-2-6	01Ai-2-7	01Ai-2-8	01Ai-2-9	01Ai-2-10	01Ai-2-11	01Ai-2-12	01Ai-2-13	01Ai-2-14	01Ai-2-15	01Ai-2-16
SiO ₂	63.496	63.681	63.323	63.369	63.119	63.742	63.642	64.073	63.648	64.409	63.656	63.926	63.453	63.210	63.187	63.708
BeO [†]	13.248	13.259	13.238	13.225	13.200	13.320	13.303	13.364	13.320	13.409	13.292	13.333	13.252	13.176	13.163	13.308
Al ₂ O ₃	14.377	14.581	14.994	15.131	15.103	16.163	15.873	16.002	15.510	14.914	14.903	15.110	15.070	14.618	14.317	15.199
Sc ₂ O ₃	0.420	0.427	0.267	0.300	0.262	0.273	0.104	0.071	0.275	0.319	0.295	0.288	0.270	0.273	0.307	0.268
V ₂ O ₅	0.633	0.811	0.735	0.655	0.714	0.714	0.404	0.329	0.895	0.722	0.708	0.686	0.740	0.773	0.731	0.725
Cr ₂ O ₃	0.015	0.040	0.039	0.027	0.013	0.005	0.013	0.009	0.020	0.018	0.011	0.001	0.000	0.001	0.025	0.028
TiO ₂	0.000	0.027	0.000	0.042	0.009	0.041	0.000	0.037	0.030	0.044	0.008	0.033	0.025	0.009	0.000	0.027
MnO	1.725	1.688	1.609	1.478	1.576	0.919	1.424	1.401	1.336	1.637	1.637	1.552	1.547	1.738	1.804	1.575
CaO	0.007	0.005	0.015	0.005	0.000	0.012	0.005	0.000	0.025	0.019	0.023	0.004	0.008	0.010	0.010	0.000
MnO	0.010	0.000	0.025	0.000	0.000	0.007	0.000	0.001	0.000	0.008	0.030	0.019	0.012	0.000	0.000	0.007
FeO	1.391	0.773	0.830	0.805	0.742	0.532	0.393	0.409	0.535	0.857	0.859	0.809	0.745	0.767	0.935	0.727
Na ₂ O	1.660	1.361	1.487	1.236	1.442	0.826	1.361	1.130	1.332	1.334	1.524	1.344	1.407	1.462	1.677	1.312
K ₂ O	0.009	0.004	0.001	0.016	0.007	0.004	0.000	0.000	0.003	0.004	0.006	0.000	0.000	0.010	0.002	0.009
CaO	0.000	0.000	0.014	0.000	0.000	0.000	0.011	0.008	0.001	0.015	0.021	0.017	0.013	0.016	0.016	0.023
ZnO	0.022	0.013	0.000	0.000	0.008	0.027	0.029	0.000	0.013	0.022	0.061	0.014	0.039	0.030	0.001	0.025
H ₂ O [†]	2.247	1.993	2.101	1.888	2.062	1.539	1.994	1.797	1.969	1.970	2.132	1.979	2.033	2.079	2.262	1.952
Total	99.261	98.664	98.677	98.178	98.256	98.122	98.555	98.631	98.911	99.700	99.165	99.114	98.612	98.174	98.434	98.890
<i>apfu</i> [‡]																
Si	5.986	5.998	5.974	5.984	5.972	5.976	5.975	5.987	5.967	5.999	5.980	5.988	5.980	5.991	5.995	5.979
Ti	0.000	0.002	0.000	0.003	0.001	0.003	0.000	0.003	0.002	0.003	0.001	0.002	0.002	0.001	0.000	0.002
Al	1.597	1.619	1.667	1.684	1.684	1.786	1.756	1.762	1.714	1.637	1.650	1.668	1.674	1.633	1.601	1.681
Sc	0.035	0.035	0.022	0.025	0.022	0.022	0.009	0.006	0.022	0.026	0.024	0.024	0.022	0.023	0.025	0.022
V	0.048	0.061	0.056	0.050	0.054	0.054	0.030	0.025	0.067	0.054	0.053	0.052	0.056	0.059	0.056	0.055
Cr	0.001	0.003	0.003	0.002	0.001	0.000	0.001	0.001	0.001	0.001	0.001	0.000	0.000	0.000	0.002	0.002
Be	3.000	3.000	3.000	3.000	3.000	3.000	3.000	3.000	3.000	3.000	3.000	3.000	3.000	3.000	3.000	3.000
Mq	0.242	0.237	0.226	0.208	0.222	0.128	0.199	0.195	0.187	0.227	0.229	0.217	0.217	0.246	0.255	0.220
Ca	0.001	0.001	0.002	0.001	0.000	0.001	0.001	0.000	0.003	0.002	0.002	0.000	0.001	0.001	0.001	0.000
Mn	0.001	0.000	0.002	0.000	0.000	0.001	0.000	0.000	0.000	0.001	0.002	0.002	0.001	0.000	0.000	0.001
Fe	0.110	0.061	0.065	0.064	0.059	0.042	0.031	0.032	0.042	0.067	0.068	0.063	0.059	0.061	0.074	0.057
Na	0.303	0.248	0.272	0.226	0.265	0.150	0.248	0.205	0.242	0.241	0.278	0.244	0.257	0.269	0.308	0.239
K	0.001	0.001	0.000	0.002	0.001	0.000	0.000	0.000	0.000	0.000	0.001	0.000	0.000	0.001	0.000	0.001
Cs	0.000	0.000	0.001	0.000	0.000	0.000	0.000	0.000	0.000	0.001	0.001	0.001	0.001	0.001	0.001	0.001
Zn	0.002	0.001	0.000	0.000	0.001	0.002	0.002	0.000	0.001	0.002	0.004	0.001	0.003	0.002	0.000	0.002

Oxide %	01Ai-3-1	01Ai-3-2	01Ai-3-3	01Ai-3-4	01Ai-3-5	01Ai-3-6	01Ai-3-7	01Ai-3-8	01Ai-3-9	01Ai-3-10	01Ai-3-11	01Ai-3-13	01Ai-3-14
SiO ₂	64.162	64.139	63.465	63.244	63.915	63.795	63.725	63.209	63.199	63.803	63.404	63.400	63.181
BeO [†]	13.394	13.341	13.286	13.190	13.326	13.289	13.266	13.157	13.198	13.287	13.252	13.191	13.208
Al ₂ O ₃	15.412	14.835	15.017	14.898	15.074	14.963	14.680	14.504	14.462	14.789	14.571	13.889	14.254
Sc ₂ O ₃	0.086	0.259	0.335	0.277	0.255	0.294	0.290	0.316	0.317	0.288	0.350	0.503	0.501
V ₂ O ₅	0.453	1.002	1.194	0.853	0.819	0.772	0.739	0.720	0.747	0.752	0.884	0.942	0.714
Cr ₂ O ₃	0.033	0.008	0.014	0.021	0.024	0.032	0.000	0.009	0.000	0.034	0.010	0.000	0.013
TiO ₂	0.000	0.000	0.009	0.000	0.014	0.000	0.000	0.000	0.002	0.020	0.002	0.000	0.012
MnO	1.740	1.703	1.522	1.580	1.522	1.591	1.660	1.753	1.872	1.684	1.809	2.017	1.841
CaO	0.007	0.014	0.006	0.003	0.010	0.000	0.012	0.005	0.014	0.010	0.000	0.000	0.004
MnO	0.005	0.011	0.000	0.002	0.008	0.012	0.013	0.000	0.000	0.003	0.000	0.000	0.010
FeO	0.425	0.477	0.623	0.779	0.772	0.768	0.740	0.849	0.927	0.771	0.901	1.086	1.339
Na ₂ O	1.679	1.264	1.419	1.196	1.317	1.207	1.585	1.389	1.714	1.358	1.644	1.413	1.708
K ₂ O	0.001	0.000	0.003	0.009	0.017	0.007	0.000	0.000	0.003	0.000	0.015	0.005	0.007
CaO	0.006	0.000	0.012	0.027	0.005	0.006	0.000	0.024	0.000	0.005	0.077	0.025	0.000
ZnO	0.033	0.003	0.032	0.017	0.000	0.030	0.015	0.001	0.007	0.009	0.003	0.000	0.009
H ₂ O [†]	2.263	1.911	2.043	1.853	1.956	1.862	2.184	2.018	2.293	1.991	2.234	2.037	2.289
Total	99.698	98.967	98.978	97.948	99.032	98.627	98.909	97.952	98.754	98.803	99.156	98.507	99.089
<i>apfu</i> [‡]													
Si	5.982	6.004	5.965	5.988	5.990	5.995	5.999	6.000	5.980	5.997	5.975	6.002	5.974
Ti	0.000	0.000	0.001	0.000	0.001	0.000	0.000	0.000	0.000	0.001	0.000	0.000	0.001
Al	1.694	1.637	1.664	1.662	1.665	1.657	1.629	1.623	1.613	1.638	1.618	1.550	1.588
Sc	0.007	0.021	0.027	0.023	0.021	0.024	0.024	0.026	0.026	0.024	0.029	0.041	0.041
V	0.034	0.075	0.090	0.065	0.062	0.058	0.056	0.055	0.057	0.057	0.067	0.071	0.054
Cr	0.002	0.001	0.001	0.002	0.002	0.002	0.000	0.001	0.000	0.003	0.001	0.000	0.001
Be	3.000	3.000	3.000	3.000	3.000	3.000	3.000	3.000	3.000	3.000	3.000	3.000	3.000
Mq	0.242	0.238	0.213	0.223	0.213	0.223	0.233	0.248	0.264	0.236	0.254	0.285	0.259
Ca	0.001	0.001	0.001	0.000	0.001	0.000	0.001	0.000	0.001	0.001	0.000	0.000	0.000
Mn	0.000	0.001	0.000	0.000	0.001	0.001	0.001	0.000	0.000	0.000	0.000	0.000	0.001
Fe	0.033	0.037	0.049	0.062	0.060	0.060	0.058	0.067	0.073	0.061	0.071	0.086	0.106
Na	0.303	0.229	0.259	0.220	0.239	0.220	0.289	0.256	0.314	0.247	0.300	0.259	0.313
K	0.000	0.000	0.000	0.001	0.002	0.001	0.000	0.000	0.000	0.000	0.002	0.001	0.001
Cs	0.000	0.000	0.000	0.001	0.000	0.000	0.000	0.001	0.000	0.000	0.003	0.001	0.000
Zn	0.002	0.000	0.002	0.001	0.000	0.002	0.001	0.000	0.000	0.001	0.000	0.000	0.001

* Determined by stoichiometry

† Calculated H₂O = (0.84958 x Na₂O) + 0.8373 (Giuliani et al. 1997).

‡ Compositions recalculated on the basis of 3 Be and 18 O atoms per formula unit (apfu).

Table 3-1. Continued.

Oxide %	01Bi-5-1	01Bi-5-2	01Bi-5-3	01Bi-5-4	01Bi-5-5	01Bi-5-6	01Bi-5-7	01Bi-5-8	01Bi-5-9	01Bi-5-10	01Bi-5-11
SiO ₂	63.086	63.010	63.272	63.602	62.991	63.340	64.290	64.255	64.117	62.563	63.226
BeO [†]	13.120	13.163	13.154	13.248	13.107	13.222	13.388	13.414	13.370	13.057	13.136
Al ₂ O ₃	13.996	14.080	14.039	14.055	14.124	14.426	15.931	16.016	15.955	13.692	14.033
Sc ₂ O ₃	0.485	0.510	0.484	0.519	0.507	0.209	0.044	0.032	0.046	0.364	0.484
V ₂ O ₃	0.727	0.713	0.740	0.757	0.807	0.756	0.250	0.236	0.292	1.045	0.808
Cr ₂ O ₃	0.012	0.008	0.000	0.003	0.007	0.000	0.024	0.031	0.009	0.040	0.000
TiO ₂	0.007	0.018	0.008	0.029	0.023	0.000	0.002	0.000	0.005	0.000	0.000
MqO	1.789	1.804	1.690	1.760	1.803	2.070	1.510	1.557	1.543	2.173	1.723
CaO	0.003	0.022	0.006	0.006	0.000	0.015	0.004	0.000	0.000	0.002	0.007
MnO	0.012	0.012	0.016	0.000	0.000	0.008	0.006	0.000	0.000	0.001	0.000
FeO	1.364	1.426	1.468	1.392	1.039	0.682	0.358	0.297	0.336	0.844	1.312
Na ₂ O	1.342	1.748	1.341	1.681	1.269	1.801	1.139	1.388	1.164	1.829	1.262
K ₂ O	0.000	0.001	0.000	0.001	0.006	0.000	0.009	0.001	0.008	0.000	0.023
Cs ₂ O	0.010	0.000	0.031	0.000	0.021	0.000	0.000	0.027	0.017	0.026	0.021
ZnO	0.025	0.035	0.034	0.020	0.008	0.032	0.000	0.022	0.000	0.000	0.000
H ₂ O [†]	1.978	2.323	1.976	2.266	1.916	2.367	1.805	2.016	1.827	2.391	1.910
Total	97.956	98.875	98.259	99.339	97.626	98.928	98.759	99.292	98.689	98.026	97.944
<i>apfu</i> [‡]											
Si	6.005	5.978	6.007	5.995	6.002	5.982	5.997	5.982	5.989	5.984	6.011
Ti	0.001	0.001	0.001	0.002	0.002	0.000	0.000	0.000	0.000	0.000	0.000
Al	1.570	1.574	1.571	1.561	1.586	1.606	1.751	1.757	1.756	1.543	1.572
Sc	0.040	0.042	0.040	0.043	0.042	0.017	0.004	0.003	0.004	0.030	0.040
V	0.055	0.054	0.056	0.057	0.062	0.057	0.019	0.018	0.022	0.080	0.062
Cr	0.001	0.001	0.000	0.000	0.000	0.000	0.002	0.002	0.001	0.003	0.000
Be	3.000	3.000	3.000	3.000	3.000	3.000	3.000	3.000	3.000	3.000	3.000
Mq	0.254	0.255	0.239	0.247	0.256	0.291	0.210	0.216	0.215	0.310	0.244
Ca	0.000	0.002	0.001	0.001	0.000	0.001	0.000	0.000	0.000	0.000	0.001
Mn	0.001	0.001	0.001	0.000	0.000	0.001	0.000	0.000	0.000	0.000	0.000
Fe	0.109	0.113	0.117	0.110	0.083	0.054	0.028	0.023	0.026	0.068	0.104
Na	0.248	0.322	0.247	0.307	0.234	0.330	0.206	0.250	0.211	0.339	0.233
K	0.000	0.000	0.000	0.000	0.001	0.000	0.001	0.000	0.001	0.000	0.003
Cs	0.000	0.000	0.001	0.000	0.001	0.000	0.000	0.001	0.001	0.001	0.001
Zn	0.002	0.002	0.002	0.001	0.001	0.002	0.000	0.002	0.000	0.000	0.000

Oxide %	01Bi-6-1	01Bi-6-2	01Bi-6-3	01Bi-6-4	01Bi-6-5	01Bi-6-6	01Bi-6-7	01Bi-6-8	01Bi-6-9	01Bi-6-10	01Bi-6-11	01Bi-6-12	01Bi-6-13
SiO ₂	63.765	63.341	63.918	63.840	63.936	63.475	63.074	63.446	63.468	64.627	64.256	64.256	63.511
BeO [†]	13.308	13.198	13.335	13.305	13.354	13.224	13.189	13.244	13.264	13.464	13.429	13.413	13.265
Al ₂ O ₃	15.130	14.750	15.363	15.379	15.498	15.188	15.358	15.986	15.982	15.537	15.684	16.669	15.508
Sc ₂ O ₃	0.267	0.274	0.203	0.206	0.205	0.225	0.223	0.048	0.060	0.221	0.230	0.209	0.190
V ₂ O ₃	0.733	0.780	0.689	0.730	0.701	0.696	0.675	0.302	0.315	0.680	0.703	0.778	0.621
Cr ₂ O ₃	0.040	0.026	0.001	0.046	0.000	0.025	0.028	0.000	0.000	0.000	0.001	0.000	0.000
TiO ₂	0.018	0.000	0.016	0.026	0.000	0.039	0.000	0.044	0.000	0.030	0.010	0.014	0.002
MqO	1.506	1.676	1.447	1.431	1.421	1.459	1.389	1.410	1.410	1.420	1.355	0.571	1.397
CaO	0.016	0.011	0.000	0.010	0.004	0.005	0.011	0.008	0.004	0.046	0.023	0.011	0.007
MnO	0.000	0.000	0.016	0.001	0.000	0.000	0.016	0.000	0.000	0.000	0.000	0.017	0.000
FeO	0.821	0.902	0.706	0.654	0.722	0.683	0.684	0.339	0.334	0.762	0.745	0.522	0.635
Na ₂ O	1.339	1.186	1.323	1.020	1.305	1.095	1.359	1.066	1.305	1.062	1.240	0.591	1.311
K ₂ O	0.004	0.006	0.003	0.007	0.015	0.000	0.000	0.000	0.005	0.006	0.004	0.006	0.000
Cs ₂ O	0.000	0.025	0.011	0.000	0.011	0.003	0.002	0.024	0.000	0.009	0.000	0.011	0.015
ZnO	0.023	0.019	0.012	0.015	0.011	0.000	0.000	0.000	0.027	0.008	0.028	0.000	0.000
H ₂ O [†]	1.974	1.845	1.961	1.704	1.946	1.768	1.992	1.743	1.946	1.740	1.891	1.340	1.951
Total	98.942	98.037	99.002	98.374	99.129	97.884	97.999	97.659	98.120	99.610	99.599	98.407	98.413
<i>apfu</i> [‡]													
Si	5.984	5.994	5.986	5.992	5.979	5.995	5.972	5.983	5.976	5.995	5.976	5.983	5.979
Ti	0.001	0.000	0.001	0.002	0.000	0.003	0.000	0.003	0.000	0.002	0.001	0.001	0.000
Al	1.673	1.645	1.696	1.701	1.708	1.690	1.714	1.777	1.773	1.699	1.719	1.829	1.721
Sc	0.022	0.023	0.017	0.017	0.017	0.019	0.018	0.004	0.005	0.018	0.019	0.017	0.016
V	0.055	0.059	0.052	0.055	0.053	0.053	0.051	0.023	0.024	0.051	0.052	0.058	0.047
Cr	0.003	0.002	0.000	0.003	0.000	0.002	0.002	0.000	0.000	0.000	0.000	0.000	0.000
Be	3.000	3.000	3.000	3.000	3.000	3.000	3.000	3.000	3.000	3.000	3.000	3.000	3.000
Mq	0.211	0.236	0.202	0.200	0.198	0.205	0.196	0.198	0.198	0.196	0.188	0.079	0.196
Ca	0.002	0.001	0.000	0.001	0.000	0.000	0.001	0.001	0.000	0.005	0.002	0.001	0.001
Mn	0.000	0.000	0.001	0.000	0.000	0.000	0.001	0.000	0.000	0.000	0.000	0.001	0.000
Fe	0.064	0.071	0.055	0.051	0.056	0.054	0.054	0.027	0.026	0.059	0.058	0.041	0.050
Na	0.244	0.218	0.240	0.186	0.237	0.201	0.249	0.195	0.238	0.191	0.224	0.107	0.239
K	0.000	0.001	0.000	0.001	0.002	0.000	0.000	0.000	0.001	0.001	0.000	0.001	0.000
Cs	0.000	0.001	0.000	0.000	0.000	0.000	0.000	0.001	0.000	0.000	0.000	0.000	0.001
Zn	0.002	0.001	0.001	0.001	0.001	0.000	0.000	0.000	0.002	0.001	0.002	0.000	0.000

* Determined by stoichiometry

† Calculated H₂O = (0.84958 x Na₂O) + 0.8373 (Giuliani et al. 1997).

‡ Compositions recalculated on the basis of 3 Be and 18 O atoms per formula unit (apfu).

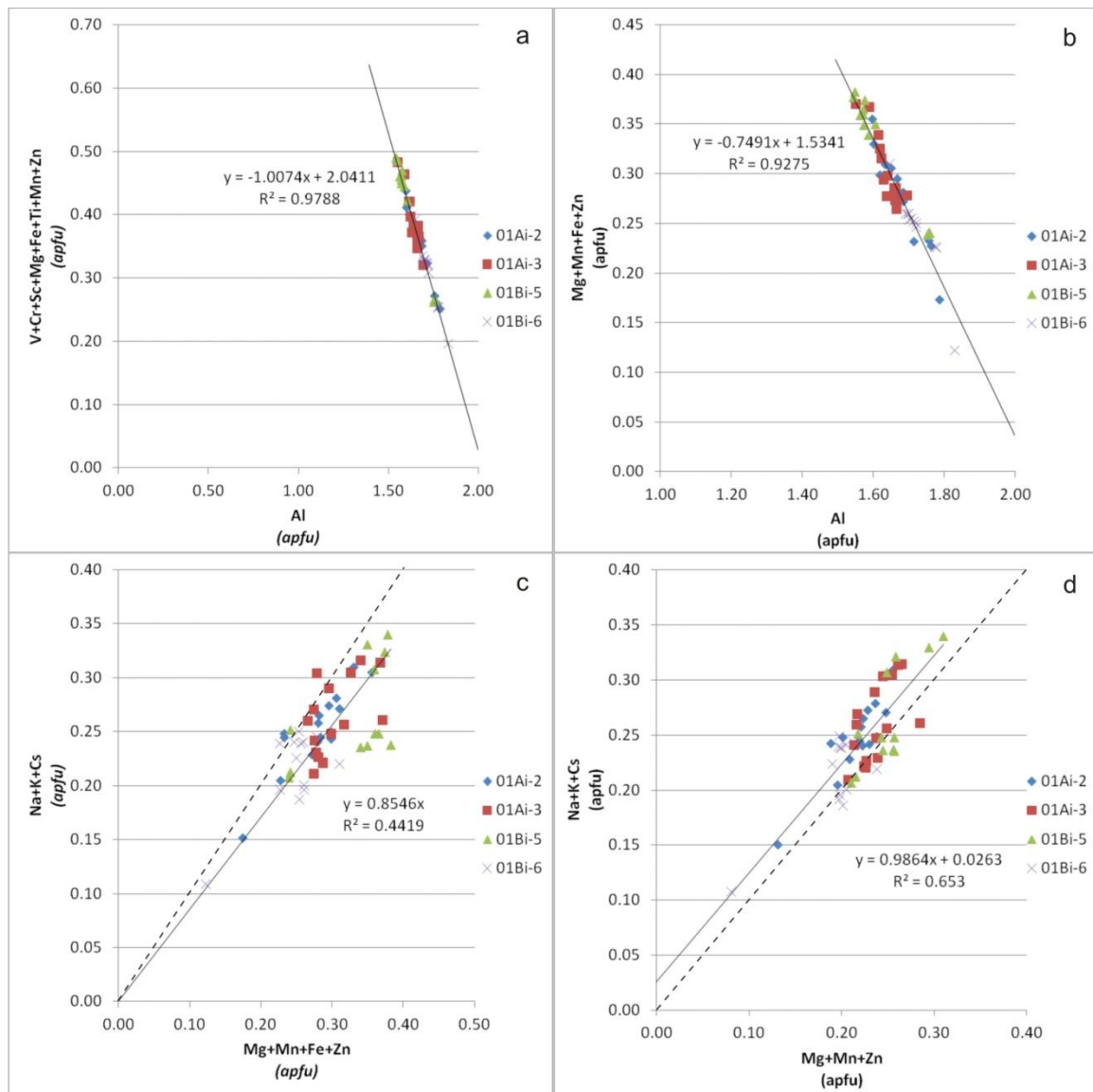


Figure 3-4. *Element plots obtained from EMPA data in atoms per formula unit (apfu). a) Al plotted against minor and trace elements from beryl shows a nearly 1:1 inverse relationship, as expected; b) Al plotted against divalent cations displays an inverse relationship that slightly deviates from a 1:1 substitution ratio; c) divalent cations plotted against alkali cations displays a strong positive correlation that deviates below the 1:1 substitution line (dashed line); d) divalent cations (not including Fe) plotted against alkalis displays a good 1:1 positive correlation.*

The ideal beryl formula contains 6 apfu Si and, ideally, emerald should contain 2 apfu of total Al and substituting cations (V, Cr, Sc, Fe, Mg, Mn, Ti, Zn). However, the crystals analysed consistently contain less than 6 apfu Si in most zones (5.97 to 6.01

apfu), and more than 2 apfu total Al and substituting cations (2.00 to 2.05 apfu). In order to avoid having vacancies in the Si tetrahedral sites, Al in IV coordination would enter into the site, and the remaining Al in VI coordination would fill its regular position in the octahedral site. A weak negative correlation between low Si and high Al (Fig. 3-5) indicates a possible site for excess Al, where it likely substitutes for Si as it does in quartz (Rusk et al. 2008; Lehmann et al. 2009).

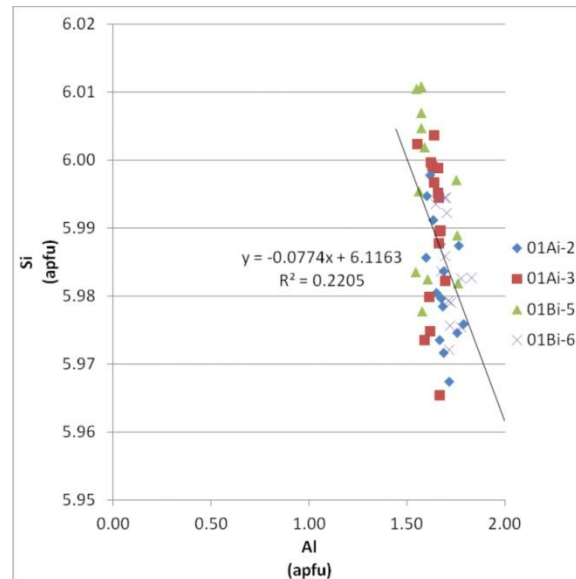


Figure 3-5. *An element plot obtained from EMPA data in atoms per formula unit (apfu) in which Al shows a very weak negative correlation to Si, for which it may substitute in the beryl structure.*

The EMPA traverses also reveal a subtle relationship between zonation and CL intensity for three of the four crystals studied. Relationships between element contents and CL intensity from dark to bright are weak, with shallow positive slopes on lines of best fit (Fig. 3-6). EMPA traverses for crystals 01Ai-2, 01Ai-3, and 01Bi-5 indicate that bright cores and all bright zones are associated with relatively high Al contents and relatively low minor element contents. The darkest, least luminescent zones are always associated with the lowest Al, and highest minor element contents. Aluminum is not known as a CL activator in beryl, but is implicated in CL activation in igneous and authigenic quartz where it substitutes for Si in the tetrahedral site (Rusk et al. 2008; Lehmann et al. 2009), as it does in the Mountain River beryl crystals. Chromium and Zn are also relatively high in the cores of two of the four crystals studied. Chromium has been implicated as a CL activator in beryl (Loughrey et al. 2012; Marshall et al. 2012)

and it may contribute to or intensify CL brightness in conjunction with Al in the beryl crystals from Mountain River. High Zn contents are also often, but not always, associated with CL brightness in the zones. Zinc's role in CL is unknown and it is not known as a CL activator in beryl. In beryl from Mountain River, it may contribute to some degree to activation or may simply be associated with Cr during crystallization. Outside of the cores, bright zones in the rims are always associated with higher Cr contents, whereas Al concentrations tend to decrease towards the outer rims. Chromium has been implicated in luminescence activation in beryl crystals from other occurrences (Loughrey et al. 2012; Marshall et al. 2012), thus Cr may be the cause of CL activation of the outer zones. Iron contents are always relatively high when zones are dark and CL activation is quite low. This relationship may be due to the quenching effect of Fe^{3+} (Ponahlo 2000). Magnesium, Na, V, and occasionally Sc are also associated with zones of low CL activation, and may contribute to the quenching effect, or are simply associated with Fe in the transport and crystallization process. Iron, V, and Sc have nearly identical distribution patterns (Fig. 3-6), supporting the correlation in the transport and crystallization process. This is quite dissimilar to other emerald occurrences where strong correlations between Cr, V, and Fe have been reported (Loughrey et al. 2012; Marshall et al. 2012). Calcium, Mn, Zn, Ti, K, and Cs seem to vary in concentrations independently of each other and of CL intensity.

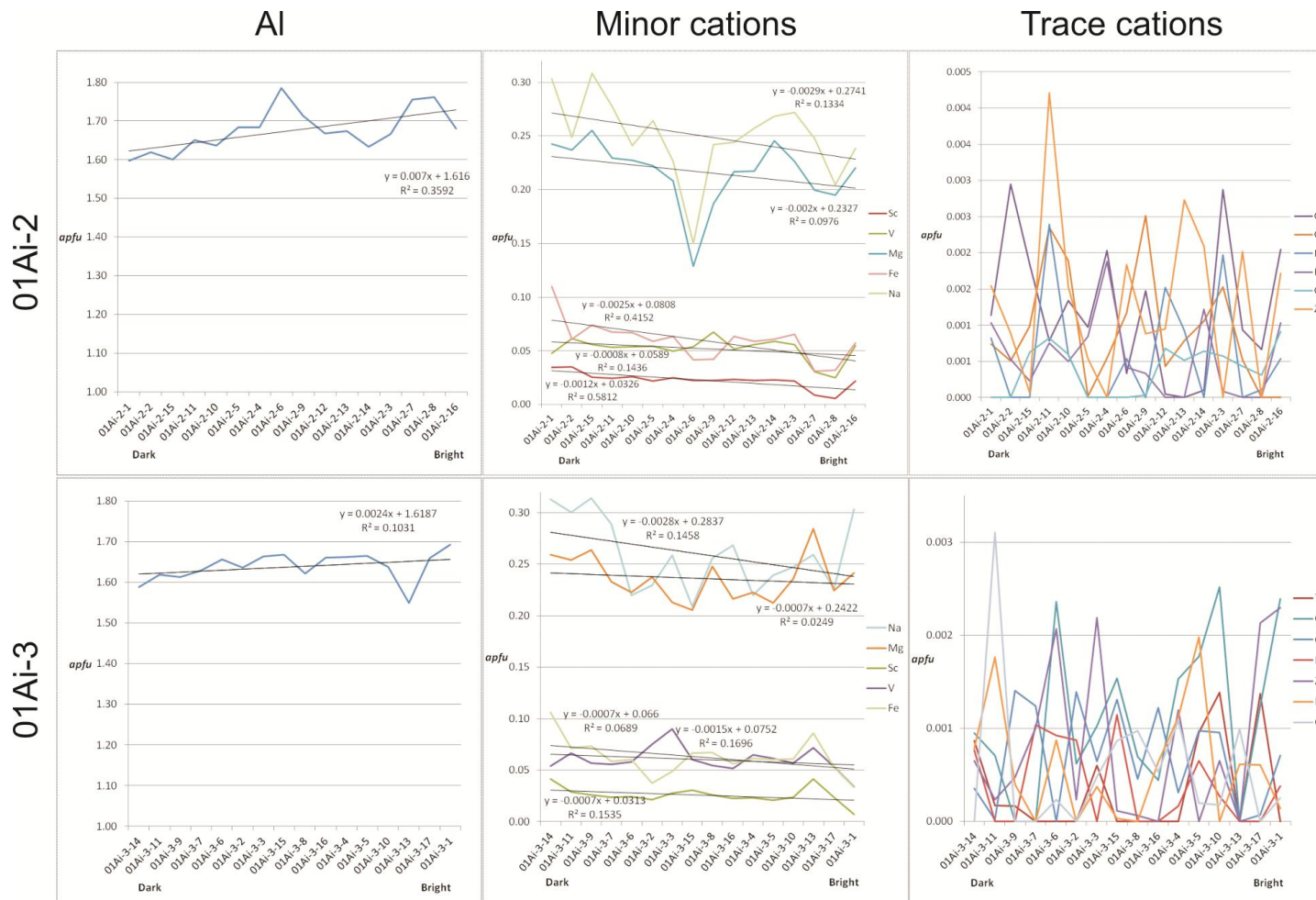


Figure 3-6. Element plots obtained from EMPA data in atoms per formula unit (apfu) comparing element concentrations to CL intensity (dark vs. bright) for the crystals studied.

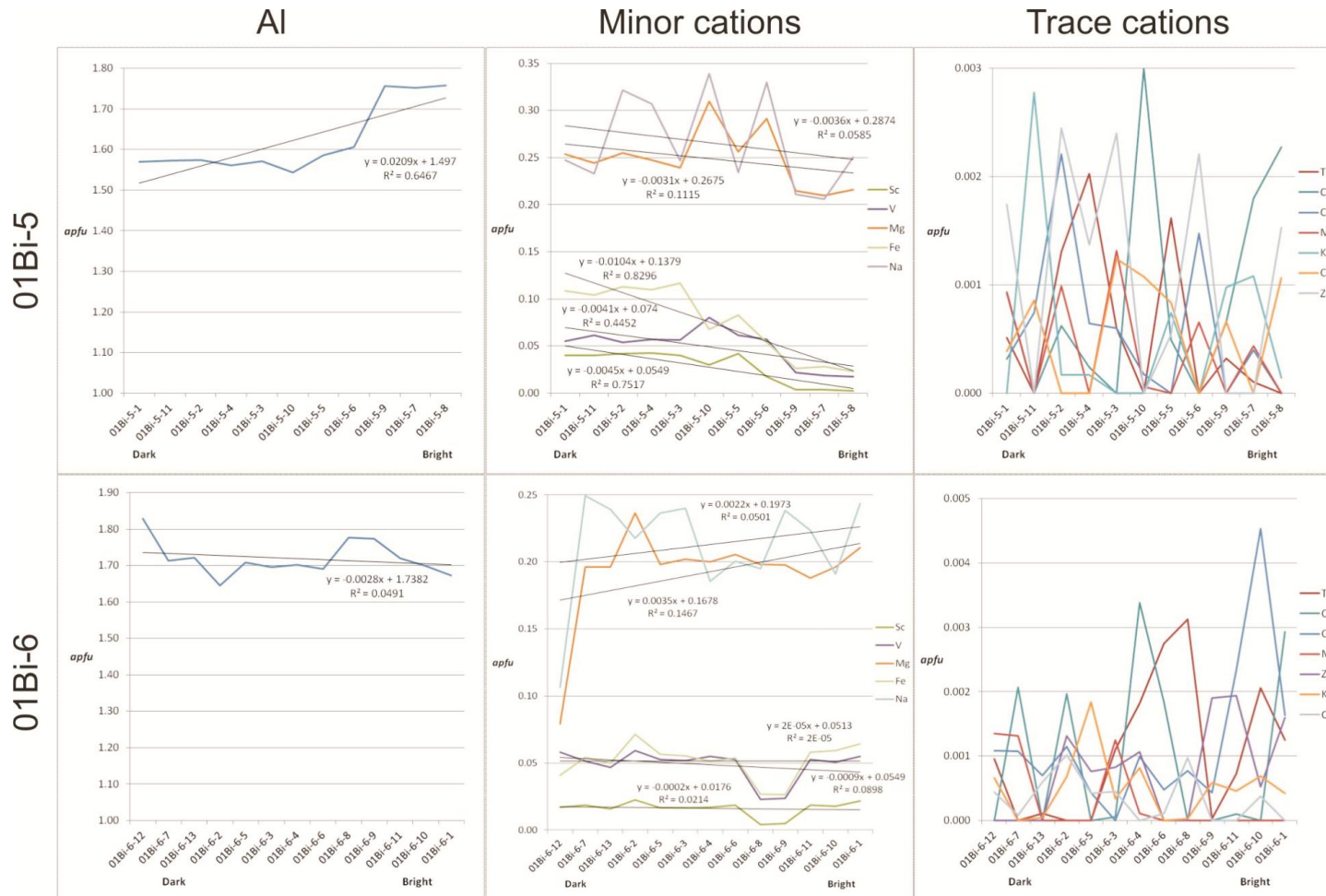


Figure 3-6. Continued.

For the fourth crystal studied, 01Bi-6, the relationships discussed above did not hold true. In this crystal, Al contents have a weak negative correlation from dark to bright zones, however, the coefficient of determination was so poor ($R^2 = 0.0491$) that this sample can effectively be ignored in our interpretation and assume this crystal has no meaningful correlation between Al concentration and CL intensity.

3.5.3. Raman spectroscopy

Raman shift bands were observed at 3608 and 3598 cm^{-1} in the spectra of both samples of beryl analysed (Fig. 3-7) with very similar relative intensities. For both samples, the band at 3608 cm^{-1} was less intense than the band at 3598 cm^{-1} , so that $I_{3598}/I_{3608} = 1.36$ (where I is peak intensity) for sample 10mh01B, and $I_{3598}/I_{3608} = 1.31$ for sample 10mh11Avii. In natural beryl crystals, the strength of the band at 3598 cm^{-1} , and therefore the I_{3598}/I_{3608} ratio, is dependent on the amount of alkali ions present in the crystal (Le Thi-Thu et al. 2010). Le Thi-Thu et al. (2010) assigned this band to the vibration of type II water molecules trapped within the hollow channels of beryl, while the band at 3608 cm^{-1} was assigned to the vibration of type I free water molecules. We interpret the Raman spectra to indicate that a substantial amount of water present in the beryl crystals is type II water and is associated with alkali cations in the hollow channels. This interpretation is supported by EMPA data indicating average total alkali abundances (Na+K+Cs) of 1.1 and 1.3 elemental weight % for the two samples 10mh01B and 10mh11Avii, respectively. The total amount of water present in the crystal channels was calculated from measured Na_2O compositions according to the equation of Giuliani et al. (1997), and found to be 1.34 to 2.39 weight % H_2O (Table 3-1). These values are in good agreement with measured amounts of water (1.8 to 2.4 weight % H_2O) extracted from the beryl by step heating methods (Hewton et al. 2011).

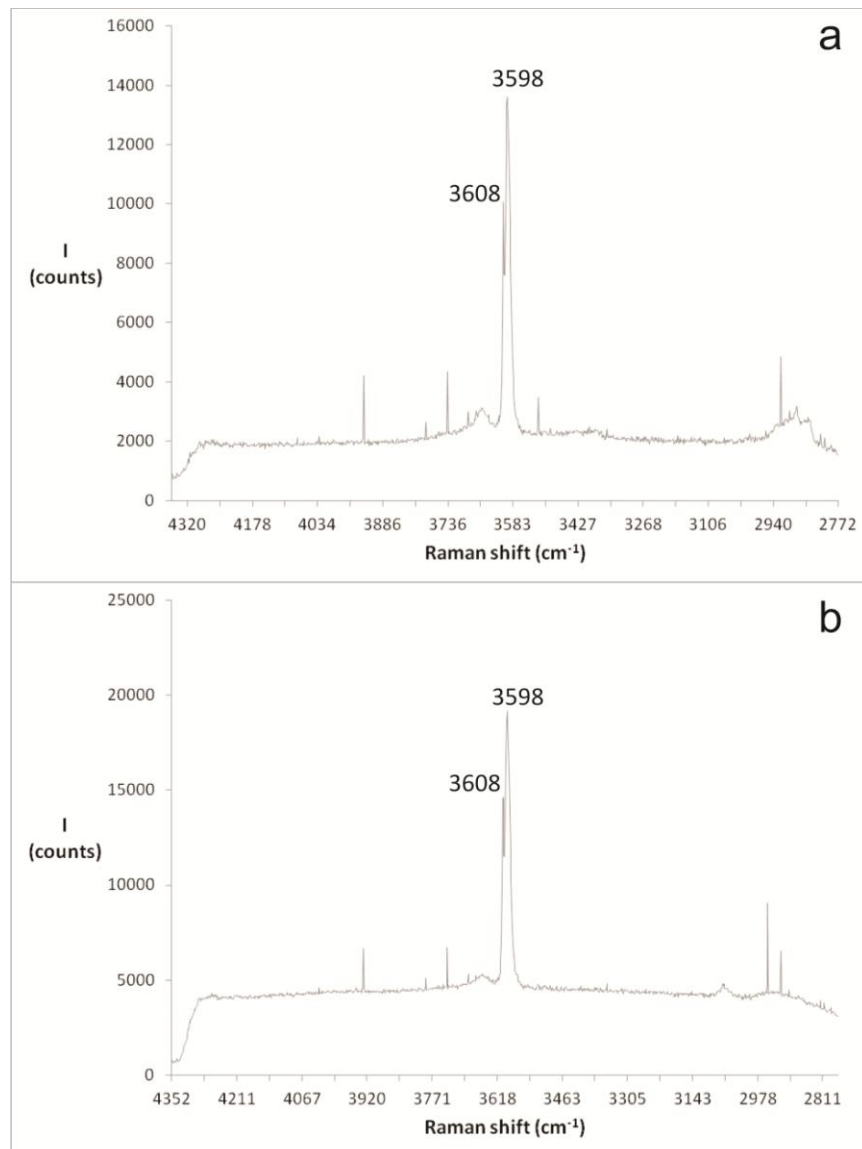


Figure 3-7. Raman spectra of beryl crystals in the water range of 4300 to 2700 cm^{-1} , for samples a) 10mh01B and b) 10mh11Avii. I = intensity in total counts. Water oriented in the type I configuration is identified by a band at 3608 cm^{-1} , and the type II configuration is identified by a band at 3598 cm^{-1} .

3.5.4. Compositional evolution of beryl

Combining otherwise invisible textures and zonation patterns revealed by CL imaging with EMPA traverses has elucidated a petrogenetic history of beryl

crystallization at Mountain River. The general decrease in Al concentration from core to rim indicates that the fluids from which beryl precipitated also decreased in Al over time. Since Al solubility is sensitive to changes in pH, this decrease may reflect a gradual increase in fluid pH as a result of host rock buffering and fluid neutralization, therefore making Al less soluble and less mobile in the system. Similar patterns of Al concentrations have been reported in quartz (Rusk et al. 2008).

Two phases of beryl crystallization, separated by a brief dissolution unconformity, are clearly visible in CL imaging, but not in SEM or BSE imaging. Early beryl crystallized from a high-Al, and low trace element content fluid that produced highly luminescent crystals. The high Al content of the beryl cores indicates that the original mineralizing fluids were probably quite acidic. The cores studied have experienced severe dissolution of their crystal faces, and only some of the earliest phase of beryl crystallization has been preserved. However, sample 01Bi-6 has preserved a second zone that is slightly darker than the majority of the core (Fig. 3-3). This preserved zone is low in Al and high in Fe, V, Sc, and Mg. Chromium, Mn, Ti, and Zn concentrations are very low or below detection limit in this zone. This low-Al zone in the core indicates that pH buffering accompanied by a decrease in Al solubility was already taking place in the first phase of beryl crystallization. Dissolution of beryl crystal faces immediately following the first phase of crystallization indicates fluids were probably under-saturated with respect to Al (Shore and Fowler 1996). Zones of the second phase of crystallization are typically lower in Al and less bright under CL than their cores. The zones show a trend towards lower Al content from core to rim, indicating a decrease in Al solubility over time as fluid pH was buffered by host rocks. The presence of abundant carbonate in the beryl-bearing veins indicates the most abundant acid involved in mineralizing fluids was likely carbonic acid. This is supported by Raman analysis of fluid inclusions in beryl which identified a CO₂ vapour phase in brine-rich two-phase (liquid + vapour) fluid inclusions (Hewton et al. in review).

3.5.5. *Geochemical signature of beryl*

It is possible to distinguish between emerald occurrences from around the globe based on their unique crystal chemical signature, particularly with respect to their minor and trace element composition. Authors have traditionally characterized the crystal chemical signatures of emerald occurrences based only on their geographic locality (Groat et al. 2007; Groat et al. 2008). Here we extend that geochemically characterizing emerald occurrences based on their proposed geological genetic model using emerald crystal chemistry in order to distinguish between the Type 1 pegmatite-hosted, Type 2 schist- or metamorphic-hosted, and Type 3 Colombian-style emerald genetic models, and compare the crystal chemical signature of beryl taken from Mountain River to this classification system.

Geochemical analyses of beryl crystals from the Mountain River occurrence show they are quite ordinary in their ratio of Fe:Mg:Cr when compared to other emerald deposit types, particularly the Type 3 Colombian emeralds (Fig. 3-8a). They are also ordinary to slightly enriched in their V and Fe contents relative to Cr (Fig. 3-8b). However, the crystals are distinctly enriched in Sc and V relative to other emerald deposit types (Fig. 3-8c). The elevated Sc in these crystals are the highest contents ever reported for emerald at up to 0.36 weight % Sc. Geochemical analyses of bulk rock samples from unveined host rocks are also high in Sc, ranging up to 125 ppm Sc (Hewton et al. 2011), which is an order of magnitude greater than estimated average compositions of continental crust, greywacke, and shale (Lentz 2003). These host rocks are the most likely source of Sc for these crystals.

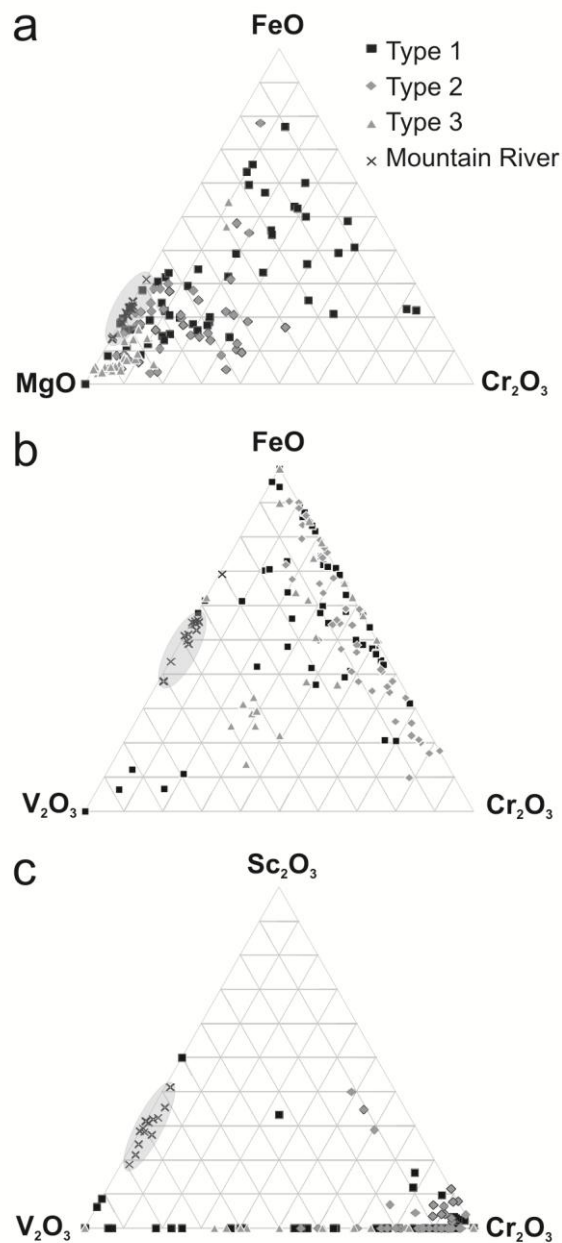


Figure 3-8. Diagrams of emerald compositions based on genetic type in terms of a) FeO-MgO-Cr₂O₃, b) FeO-V₂O₃-Cr₂O₃, and c) Sc₂O₃-V₂O₃-Cr₂O₃. Types 1, 2, and 3 data from Groat et al. 2008.

Significant amounts of alkali ions can be incorporated into the *c*-axis channels in addition to water molecules. Combining determined alkali weight percent content with relative intensities of the Raman shift bands demonstrates how the band at 3598 cm⁻¹ increases in relative intensity to the 3608 cm⁻¹ band (Fig. 3-9) as total alkali content increases in emerald crystals (Le Thi-Thu et al. 2010). This non-destructive technique of

Raman spectroscopy therefore fingerprints and distinguishes individual emerald occurrences from around the world. Crystals from Mountain River correlate well with the exponential relationship found between alkali content and relative intensity (I_{3598}/I_{3608}), and contain roughly 1.1 to 1.3 weight % total ionic Na and K. This correlation demonstrates that the Na and K present in crystals from Mountain River are located in the *c* axis channels.

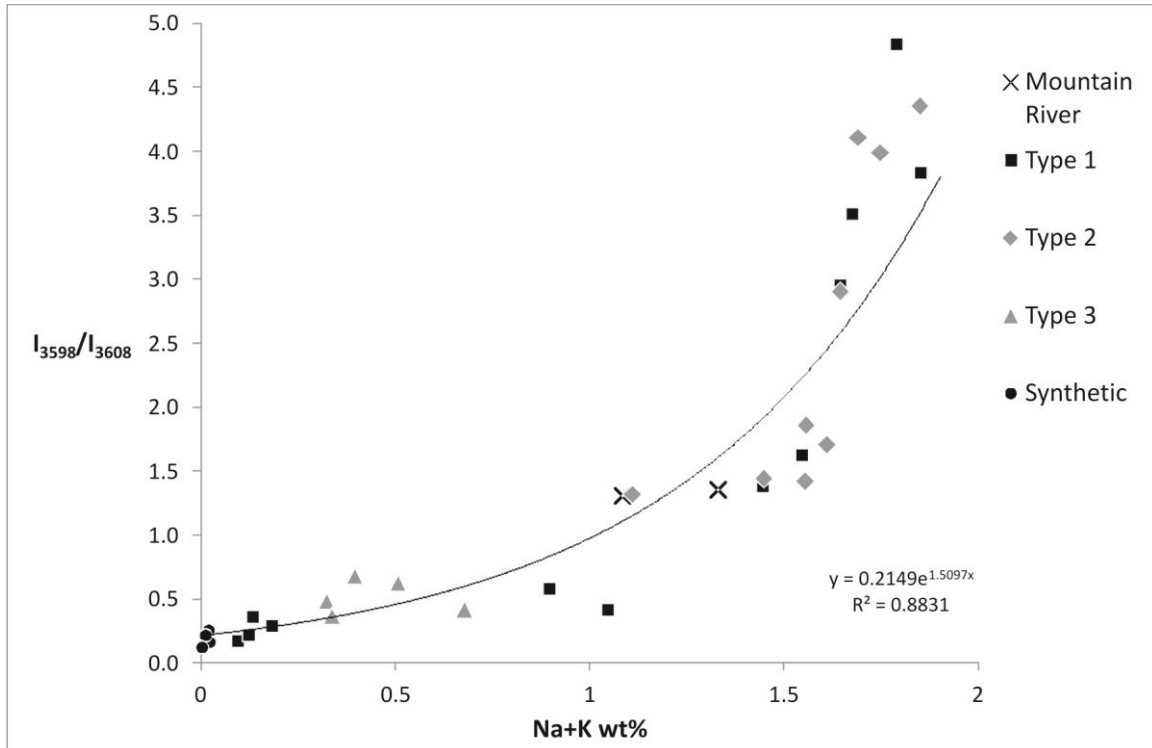


Figure 3-9. *Intensity ratios of the two Raman shift bands assigned to the two water types versus the total alkali contents for beryl from Mountain River compared to emeralds from around the world. Higher alkali contents correlate strongly with higher intensity ratios. Types 1, 2, and 3 data from Le Thi-Thu et al. (2010).*

Type 1 (pegmatite hosted) emerald spans the range of alkali contents and therefore this Raman technique is only useful to determine individual geographic, not geologic, origin. Type 2 metamorphic emeralds apparently contain higher amounts of total alkalis, which are expressed in terms of higher relative intensities of Raman bands (I_{3598}/I_{3608}), while type 3 emeralds from Colombia contain lower amounts of total alkalis, expressed in terms of lower relative intensities of Raman bands. Emerald analyses from Mountain River, despite being derived from a type 3 Colombian-style occurrence, fall

within the range expected for type 2 emeralds. Because the Mountain River emeralds are hosted in very low grade meta-sedimentary rocks, this result may simply reflect the greater temperatures and pressures involved in emerald precipitation at Mountain River relative to those at the Colombian emerald deposits (Cheilletz et al. 1994).

3.6. Conclusions

Electron microprobe traverses across zoned beryl crystals have indicated that early beryl crystallized from a high-Al, low trace element content acidic fluid that decreased in Al concentration over time. Sodium dominates the alkali component, even when compared to other Na-rich emerald. A subtle relationship between zonation and CL intensity for three of the four crystals studied indicates that Al is a probable CL activator in these crystals, a finding that has never been reported for beryl before, although Cr is likely also an activator in the outer rims where Al tends to be depleted. Zones of the second phase of crystallization are typically lower in Al and less bright under CL than their cores. The zones also show a trend towards lower Al content from core to rim. The crystals are slightly enriched in their V and Fe contents relative to Cr compared to emerald from other occurrences. However, the crystals from Mountain River are distinctly enriched in Sc and V relative to other emerald deposit types, and this enrichment is an important geochemical fingerprint for these crystals.

Combining determined alkali weight percent content with relative intensities of the Raman shift bands is also an important geochemical fingerprint. The data from Mountain River beryl correlates well with the exponential relationship found between alkali content and relative intensity (I_{3598}/I_{3608}). This finding clearly distinguishes the Mountain River crystals from other individual emerald occurrences.

3.7. Acknowledgements

The authors gratefully acknowledge Dr. M. Raudsepp and E. Czech for their supervision in operating the electron microprobe at the University of British Columbia, and C. Ozyer for his assistance and financial support of field work in the Mackenzie Mountains. The authors also acknowledge the contributions of M. Mercier, E. Martel, S. Gordey, H. Falck, J. Ketchum, and A. Lalonde to the project. The authors acknowledge funding and field support provided by the Northwest Territories Geoscience Office (contribution #0064), as well as scholarships and grants to MH and DM from NSERC, SEG Canada, and the NSTP.

References

- Al-Aasm, I.S., Lonnee, J.S., and Clarke, J. 2002. Multiple fluid flow events and the formation of saddle dolomite: case studies from the Middle Devonian of the Western Canada Sedimentary Basin. *Marine and Petroleum Geology*, **19**, 209-217.
- Banks, D.A, Giuliani, G., Yardley, B.W.D., and Cheilietz, A. 2000. Emerald mineralisation in Colombia: fluid chemistry and the role of brine mixing. *Minerallium Deposita*, **35**: 699-713.
- Beal, K-L. and Lentz, D.R. 2010. Aquamarine beryl from Zealand Station, Canada: a mineralogical and stable isotope study. *Journal of Geosciences*, **55**: 57-67.
- Cheilietz, A., Féraud, G., Giuliani, G., and Rodriguez, C. T. 1994. Time-pressure and temperature constraints on the formation of Colombian emeralds: An $^{40}\text{Ar}/^{39}\text{Ar}$ laser microprobe and fluid inclusion study. *Economic Geology*, **89**: 361-380.
- Deer, W.A., Howie, R.A., and Zussman, J. 1966. *An Introduction to the Rock-Forming Minerals*, 528 p. Longman Group Limited, London.
- Giuliani, G., France-Lanord, C., Zimmermann, J.L., Cheilietz, A., Arboleda, C., Charoy, B., Coget, P., Fontan, F., and Giard, D. 1997. Fluid composition, δD of channel H_2O , and $\delta^{18}\text{O}$ of lattice oxygen in beryls: genetic implications for Brazilian, Colombian, and Afghanistani emerald deposits. *International Geology Review*, **39**: 400–424.
- Giuliani, G., France-Lanord, C., Cheilietz, A., Yannick-Branquet, P., and Laumonnier, B. 2000. Sulfate reduction by organic matter in Colombian emerald deposits: Chemical and stable isotope (C, O, H) evidence. *Economic Geology*, **95**: 1129-1153.
- Graziani, G., Lucchesi, S., and Scandale, E. 1990. General and specific growth marks in pegmatite beryls. *Physics and Chemistry of Minerals*, **17**: 379-384.
- Groat, L.A., Giuliani, G., Marshall, D., and Turner, D. 2007. Chapter 3: Emerald. *In Geology of Gem Deposits, Short Course 37. Edited by L.A. Groat. Mineralogical Association of Canada, Yellowknife, Northwest Territories*, p. 79-109.
- Groat, L.A., Giuliani, G., Marshall, D., and Turner, D. 2008. Emerald deposits and occurrences: A review. *Ore Geology Reviews*, **34**: 87-112.
- Hewton, M.L., Marshall, D.D., Ootes, L., Loguhrey, L.E., and Creaser, R.A. (in review). Colombian-style emerald mineralization in the northern Canadian Cordillera: Integration into a regional Paleozoic fluid flow regime.
- Hewton, M., Marshall, D., Ootes, L., and Martel, E. 2011. Geochemical constraints on the origin of emeralds at Mountain River, Mackenzie Mountains, NT, Canada. NWT Geoscience Office, NWT Open Report 2011-005, 28 p.

- Le Thi-Thu, H., Haeger, T., and Hofmeister, W. 2010. Confocal micro-Raman spectroscopy; a powerful tool to identify natural and synthetic emeralds. *Gems and Gemmology*, **46**(1): 36-41.
- Lehmann, K., Berger, A., Götze, T., Ramseier, K., and Wiedenbeck, M. 2009. Growth related zones in authigenic and hydrothermal quartz characterized by SIMS-, EPMA-, SEM-CL- and SEM-CC-imaging. *Mineralogical Magazine*, **73**: 633-643.
- Lentz, D.R. 2003. Geochemistry of sediments and sedimentary rocks: historical to research perspectives. *In Inorganic Geochemistry of Sediments and Sedimentary Rocks: Evolutionary Considerations to Mineral Deposit-Forming Environments*. Edited by D.R. Lentz. Geological Association of Canada, *GeoText 4*, p. 1-6.
- Loughrey, L., Marshall, D., Jones, P., Millstead, P., and Main, A. 2012. Pressure-temperature-fluid constraints for the Emmaville-Torrington emerald deposit, New South Wales, Australia: Fluid inclusion and stable isotope studies. *Central European Journal of Geoscience*, **4**(2): 287-299.
- Lund, K. 2008. Geometry of the Neoproterozoic and Paleozoic rift margin of western Laurentia: Implications for mineral deposit settings. *Geosphere*, **4**(2): 429-444.
- Marshall, D., Pardieu, V., Loughrey, L., Jones, P., and Xue, G. 2012. Conditions for emerald formation at Davdar, China: fluid inclusion, trace element and stable isotope studies. *Mineralogical Magazine*, **76**: 213-226.
- Morris, G.A. and Nesbitt, B.E. 1998. Geology and timing of palaeohydrogeological events in the Mackenzie Mountains, Northwest Territories, Canada. *In Dating and Duration of Fluid Flow and Fluid-Rock Interaction*. Edited by J. Parnell. Special Publications 144, Geological Society, London, p. 161-172.
- Nelson, J., Paradis, S., Christensen, J., and Gabites, J. 2002. Canadian Cordilleran Mississippi Valley-Type deposits: A case for Devonian-Mississippian back-arc hydrothermal origin. *Economic Geology*, **97**: 1013-1036.
- Nelson, J. and Colpron, M. 2007. Tectonics and metallogeny of the British Columbia, Yukon and Alaskan Cordillera, 1.8 Ga to the present. *In Mineral Deposits of Canada: A Synthesis of Major Deposit Types, District Metallogeny, the Evolution of Geological Provinces, and Exploration Methods*. Edited by W.D. Goodfellow. Special Publication No. 5, Geological Association of Canada, Mineral Deposits Division, p. 755-791.
- Ohmoto, H. and Rye, R.O. 1979. Isotopes of Sulfur and Carbon. *In Geochemistry of Hydrothermal Ore Deposits*. Edited by H. Barnes. John Wiley and Sons, New York.
- Ottaway, T.L., Wicks, F.J., Bryndzia, L.T., Kyser, T.K., and Spooner, E.T.C. 1994. Formation of the Muzo hydrothermal emerald deposit in Colombia. *Nature*, **369**: 552-554.

- Ponahlo, J. 2000. Cathodoluminescence as a Tool in Gemstone Identification. *In* Cathodoluminescence in Geosciences. *Edited by* M. Pagel, V. Barbin, P. Blanc, D. Ohnenstetter. Springer-Verlag, Berlin.
- Pouchou, J.L. and Pichoir, F. 1985. PAP $\phi(\rho Z)$ procedure for improved quantitative microanalysis. *Microbeam Analysis*, **1985**: 104-106.
- Rusk, B.G, Lowers, H.A., and Reed, M.H. 2008. Trace elements in hydrothermal quartz: Relationships to cathodoluminescent textures and insights into vein formation. *Geology*, **36**: 547-550.
- Schwarz, D., and Giuliani, G. 2001. Emerald deposits – A review. *Australian Gemmologist*, **21**: 17-23.
- Shore, M., and Fowler, A.D. 1996. Oscillatory zoning in minerals: a common phenomenon. *Canadian Mineralogist*, **34**: 1111-1126.
- Turner, D., and Groat, L.A. 2007. Chapter 4: Non-emerald gem beryl. *In* *Geology of Gem Deposits, Short Course 37*. *Edited by* L.A. Groat. Mineralogical Association of Canada, Yellowknife, Northwest Territories, p. 79-109.
- Vavra, G. 1990. On the kinematics of zircon growth and its petrogenetic significance: a cathodoluminescence study. *Contributions to Mineralogy and Petrology*, **106**: 90-99.
- Wood, D.L., and Nassau, K. 1967. Infrared spectra of foreign molecules in beryl. *The Journal of Chemical Physics*, **47**(7): 2220-2228.

4. Colombian-style emerald mineralization in the northern Canadian Cordillera: Integration into a regional Paleozoic fluid flow regime*

Hewton, M. L.

Department of Earth Sciences, Simon Fraser University,
8888 University Drive, Burnaby, BC, V5A 1S6

Marshall, D. D.

Department of Earth Sciences, Simon Fraser University,
8888 University Drive, Burnaby, BC, V5A 1S6

Ootes, L.

Northwest Territories Geoscience Office,
Box 1500, Yellowknife, NT, X1A 2R3

Loughrey, L. E.

Department of Earth Sciences, Simon Fraser University,
8888 University Drive, Burnaby, BC, V5A 1S6

Creaser, R. A.

Department of Earth & Atmospheric Sciences, University of Alberta,
126 ESB, Edmonton, AB, T6G 2R3

*Submitted to *Canadian Journal of Earth Sciences* and reproduced here (including acknowledgements, appendix, and references) as Chapter 4.

4.1. Abstract

Emerald in the Mackenzie Mountains is associated with extensional quartz-carbonate veins in organic-poor sandstones and siltstones. The section hosting the emerald-bearing veins is within the hangingwall of a thrust fault placing Neoproterozoic siliciclastic strata above Paleozoic rocks. Isotopic compositions of water extracted from emerald are typical of evolved sedimentary waters. $\delta^{18}\text{O}_{\text{V-SMOW}}$ values for emerald, quartz, and dolomite have averages of 17.3‰ (± 0.9), 19.6‰ (± 1.5), and 18.1‰ (± 1.0), respectively. Dolomite has an average $\delta^{13}\text{C}_{\text{VPDB}}$ value of -6.8‰ (± 1.0). Two pyrite samples returned $\delta^{34}\text{S}_{\text{CDT}}$ values of 5.1 and 11.2‰. Triply concordant mineral equilibration temperatures were determined by mineral pair $\delta^{18}\text{O}_{\text{V-SMOW}}$ equilibration (quartz-emerald, quartz-dolomite, emerald-dolomite) in the range 379 to 415°C. Fluid inclusion analyses indicate saline (>19.8 wt% NaCl equivalent) $\text{CO}_2\text{-N}_2$ -bearing brines and minimum trapping temperatures between 118 and 258°C. Isochores derived from fluid inclusion data and constrained by isotope equilibration temperatures indicate fluid pressures of 2.4 to 4.0 kbar, corresponding to depths of 9 to 15 km. A Re-Os isochron age of 345 ± 20 Ma from pyrite indicates that mineralization was contemporaneous with estimated ages of some northern Cordillera Zn-Pb occurrences. Emerald formation resulted from inorganic thermochemical sulphate reduction via the circulation of deep-seated hydrothermal carbonic brines through basinal siliciclastic, carbonate, and evaporitic rocks. These brines were driven along deep basement structures and reactivated normal faults related to tectonic activity associated with the development of a back-arc basin during the Late Devonian to Middle Mississippian. The Mountain River emerald occurrence thus represents a modification of the Colombian-type emerald deposit model.

4.2. Introduction

Emerald, the green gem variety of the cyclosilicate mineral beryl, is typically formed by the introduction of Be-rich fluids to Cr (\pm V)-rich host rocks. In general, emerald deposits can be classified into three main categories (Schwarz and Giuliani 2001): Type 1 deposits are associated with the intrusion of Be-rich granitic or pegmatitic bodies into mafic or ultramafic host rocks; Type 2 deposits are found in upper greenschist to amphibolite facies metamorphic environments coincident with major crustal breaks (ie. shear zones and thrusts) and metasomatism; and Type 3 deposits, typified by the world class deposits of Colombia, involve the in situ mobilization of hydrothermal carbonic brines that liberate and transport Be and Cr (\pm V) from organic-rich black shales in situ. Emerald mineralization in Colombia resulted from thermochemical sulphate reduction by reaction with organic matter within the host rocks during Paleogene tectonic activity (Ottaway et al. 1994; Giuliani et al. 2000).

Emeralds in Canada's northern Cordillera were first identified in 1997 at the Lened occurrence, Northwest Territories, where emeralds are hosted in quartz-carbonate veins in skarn. Skarn formation and emerald mineralization are associated with the 93 Ma Lened pluton (Marshall et al. 2004). Other emeralds at the Tsa da Glisza deposit in the Yukon are found in quartz veins cutting meta-volcanic rocks of the Yukon-Tanana Terrane in close proximity to a 109 Ma granitic pluton (Groat et al. 2002). Both occurrences are categorized as Type 1 deposits, according to their relationships with granitic plutons (Groat et al. 2002; Marshall et al. 2004).

The Mountain River emerald occurrence, discovered in 2007 in the north-central Mackenzie Mountains, Northwest Territories (Fig. 4-1; Mercier 2008), is the third discovery of emerald in the northern Canadian Cordillera. Mineralization consists of quartz-carbonate-emerald veins within sub-greenschist facies organic-poor siliciclastic rocks. The emerald-bearing veins and host rocks are preserved within the hangingwall of a regional scale thrust fault that strikes southeast. There is no evidence of felsic igneous activity or significant regional metamorphism in this area of the northern Cordillera, and overall the Mountain River occurrence appears to have no geological similarities with either the Type 1 or 2 deposit models. However, the Mountain River occurrence appears

to share some geological similarities with the type 3 Colombian-style deposit model as emeralds at both localities are found in quartz-carbonate veins hosted in sedimentary rocks, and are associated with regional structural features in regions that lack evidence of magmatic and metamorphic activity (Cheilletz et al. 1994; Gordey et al. 2011a).

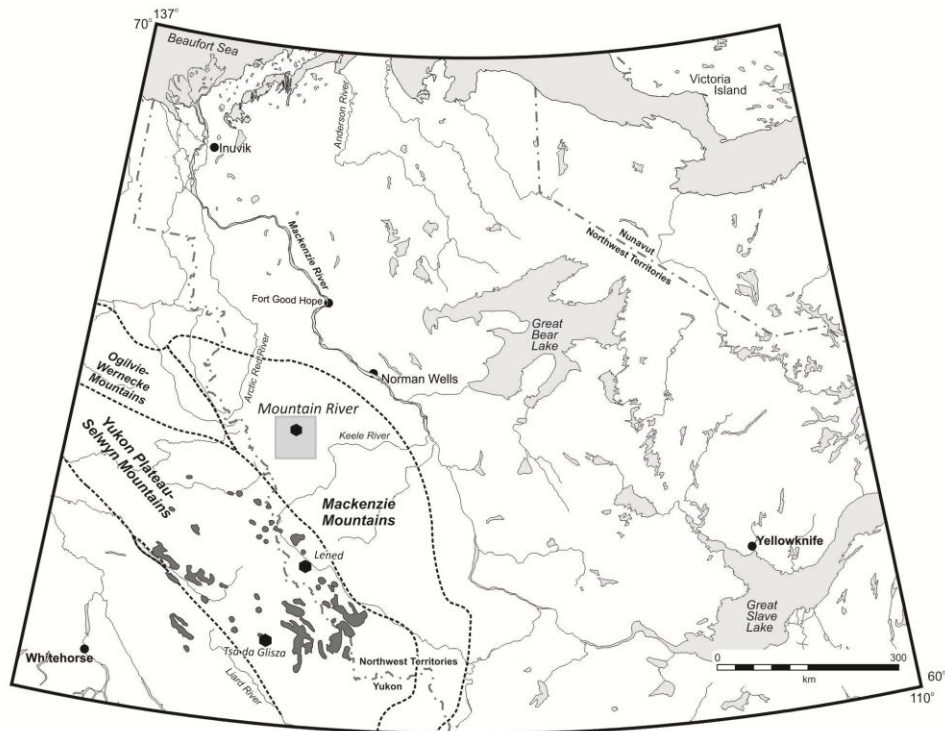


Figure 4-1. Location of the Mountain River emerald occurrence in the Mackenzie Mountains in relation to the Lened and Tsa da Glisza occurrences and the extent of Cretaceous felsic plutonism (dark grey).

This paper presents results from fluid inclusion analyses, stable isotope (D, O, C, and S), and radiogenic isotope (Re-Os) results from vein material taken from the emerald showing, and discusses how these results constrain conditions (temperature and pressure), composition, and the source of fluids responsible for emerald mineralization. The timing of mineralization is significant as it is coincident with extensive base metal mineralization and dolomite alteration throughout the northern Cordillera. Collectively the data indicate the Mountain River emerald occurrence represents a modification to the Type 3 Colombian-style emerald mineralization model and is the result of wide-spread, late Paleozoic fluid flow in the northern Cordillera of Canada.

4.3. Geologic setting

The Mackenzie Mountains (Fig. 4-1), the northernmost extent of the Cordilleran foreland fold and thrust belt, are composed of a thick succession of well-preserved siliciclastic, carbonate, and minor evaporite rocks that record the early rifting and breakup of the supercontinent Rodinia during the Neoproterozoic and the establishment of the Mackenzie Platform east of the Selwyn Basin during the Paleozoic (Ross 1991). These rocks were thrust and folded into their current configuration of broad regional folds, local tight folds, and thrust faults during Cretaceous-Tertiary orogenesis (Yorath 1991). Numerous orogen-parallel thrust faults occur throughout the Mackenzie Mountains. One of these, the Shale Lake fault, is a major southwest-dipping thrust fault that is suggested to account for up to 15 km of shortening (Fig. 4-2; Gordey et al. 2011b). The Shale Lake fault is likely rooted in the evaporitic Gypsum Formation of the Little Dal Group, 8 km below the current erosional level (Gordey et al. 2011b). Orogenesis also resulted in sub-greenschist facies regional metamorphism and thermal alteration, which reached the level at which hydrocarbons were converted to pyrobitumen (Narbonne and Aitken 1995). However, many of the carbonate units of the region have experienced moderate to extensive carbonate alteration that predated Cretaceous-Tertiary compression. Morris and Nesbitt (1998) identified six distinct fluid events spanning the Paleozoic to early Tertiary: 1) a Silurian sedimentary exhalative event associated with the expulsion of brines onto the seafloor along extensional faults; 2) diagenetic dolomitization affecting Early Devonian and older carbonates; 3) the Late Devonian to Mississippian regionally extensive Manetoe Facies hydrothermal dolomitization event associated with carbonate-hosted Zn-Pb mineralization and natural gas reserves; 4) a suggested Early Cretaceous or later vug-fill event, constrained by low δD values of dolomite-hosted fluid inclusions; 5) Early Cretaceous to Early Tertiary fault-hosted and high angle quartz and carbonate veins; and 6) calcite-barite mineralization infilling large voids and karsts deposited by inflowing meteoric water (Morris and Nesbitt 1998). These events represent a protracted history of fluid movement that reflect the evolving tectonic environment of the northern Cordillera, and suggest the Laurentian margin underwent a long period of subsidence and rifting punctuated by Paleozoic tectonic activity and followed by Cretaceous-Tertiary compression. Nelson et al. (2002) related the Late Devonian to Mississippian dolomitization event to extensive Zn-Pb

mineralization of the Mackenzie Mountains Zn-Pb belt, and to syngenetic sedimentary exhalative (SEDEX) and volcanogenic-hosted massive sulphide (VHMS) deposits to the west. They concluded that the high temperature, high salinity fluids involved in mineralization were driven by far-field effects of subduction along the western margin of Laurentia, which generated slab roll-back, regional extension, and the development of a back-arc basin as the Slide Mountain Ocean opened and Yukon-Tanana was rifted from Laurentia. The accompanying exhalative activity and hydrothermal fluids are postulated to have been driven along back-arc structures and permeable units toward the carbonate platform (Nelson et al. 2002; Lund 2008).

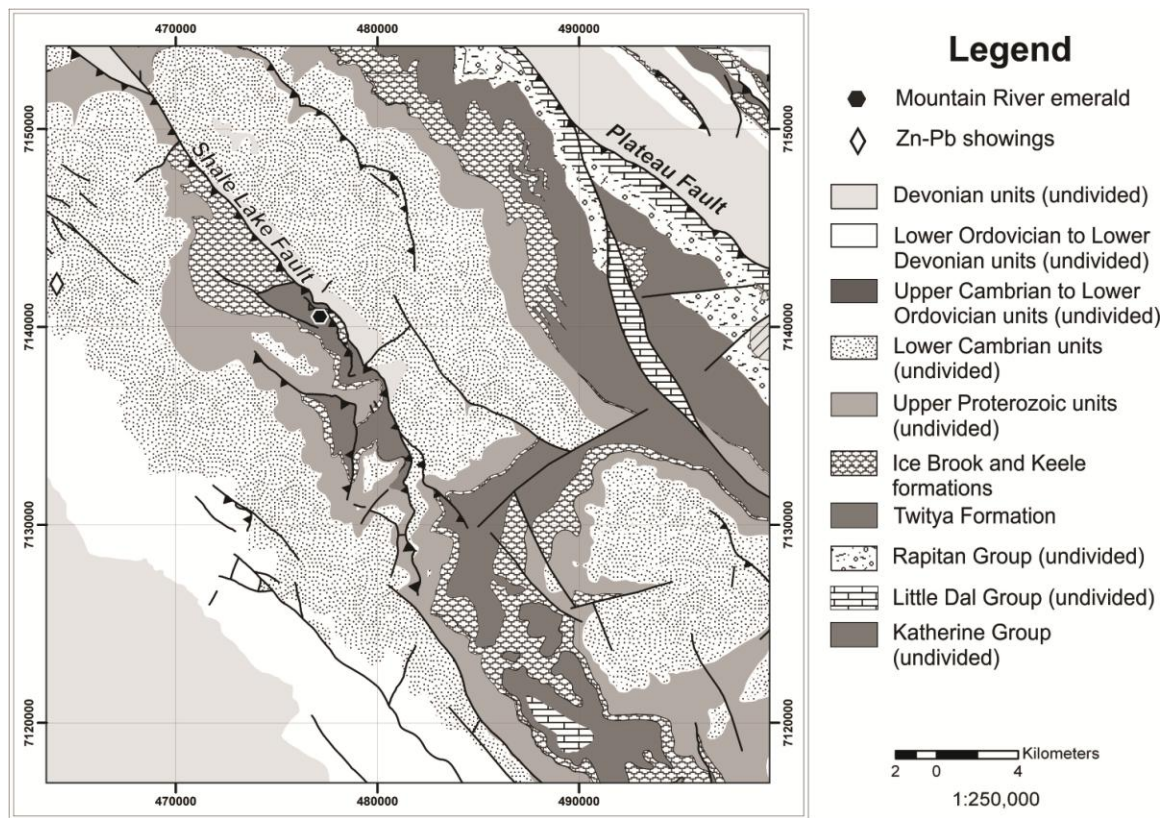


Figure 4-2. Local geology of the Mountain River emerald occurrence in the Mount Eduni map area (NTS 106A southwest). Modified from Gordey et al. (2011a).

Emerald-bearing extensional veins at Mountain River are hosted within bedded sandstones and siltstones of the Twitya Formation, part of the Neoproterozoic Windermere Supergroup (Fig. 4-2). The Twitya Formation comprises a lower shaley half cycle with packets of thin-bedded limestone turbidites and an upper package of sideritic

and dolomitic turbidite siltstones and sandstones (Narbonne and Aitken 1995). The Twitya Formation oversteps rift-related blocks and normal faults and was deposited variably on the underlying basal Rapitan Group or, in some places, on units down to the Little Dal Group, the uppermost strata of the Mackenzie Mountain Supergroup (Narbonne and Aitken 1995; Gordey et al. 2011a). In the immediate area of the emerald occurrence, the Twitya Formation may rest on top of the Little Dal Group (Gordey et al. 2011a). Sandwiched between the Little Dal Group and the Rapitan Group is the Coates Lake Group. Both the Little Dal and Coates Lake groups contain evaporitic units, which appear important to the paragenesis of the Mountain River emeralds.

4.4. Local geology and vein petrology

The host-rocks to the emerald-bearing veins are carbonatized and locally pyritized and are fractured, faulted, and folded in the immediate hangingwall of the Shale Lake fault. Within the hangingwall, emerald, quartz, and carbonate (dolomite, ankerite, calcite) are preserved in thin veins (1 mm to 10 cm). Milky green euhedral emerald crystals up to 8 mm wide and 4 cm long are commonly found toward vein selvages as individual disseminated crystals, in clusters, or in massive agglomerations. Massive white quartz and subhedral to anhedral carbonate minerals are interstitial between emerald crystals. Trace minerals include dodecahedral pyrite, rutile, albite, and biotite. Quartz and emerald in the veins show strain in the form of microkinking, and brittle fractures filled by calcite cut all primary vein minerals. This observation is interpreted to indicate that movement and brittle deformation along the Shale Lake fault occurred after emerald mineralization, which likely occurred during Cretaceous-Tertiary regional deformation. Localized bleached zones up to 2 cm wide adjacent to emerald-bearing veins are related to carbonate and silica alteration and indicate leaching of cations from host rocks. The emeralds themselves typically show zoning under cathode luminescence, and are usually high in V and Sc, but poor in Cr.

4.5. Results

4.5.1. *Fluid inclusion studies*

Fluid inclusions in emerald and quartz are abundant but quite small, ranging in size up to 20 microns. The samples were chosen based on the interpretation that quartz from the veins formed coevally with emerald, and therefore contain the same fluids that were involved in emerald mineralization. This interpretation is supported by the observation that phase ratios in both emerald- and quartz-hosted fluid inclusions are consistent. The dominant population is of two-phase fluid inclusion types (FITs) at room temperature, consisting of a brine and vapour (Fig. 4-3). A rare population consisting of a liquid, vapour, and salt crystal was observed only in quartz. Both FITs showed consistent phase ratios, where the two-phase inclusions consisted of 10% vapour and 90% brine by volume, and the three-phase FITs consisted of 10% vapour, 10% salt crystal, and 80% brine. It was not obvious whether fluid inclusions were aligned with growth zones, situated along healed fractures, or as isolated inclusions, and thus most inclusions were identified as secondary but grouped petrographically into fluid inclusion types (Goldstein and Reynolds 1994).

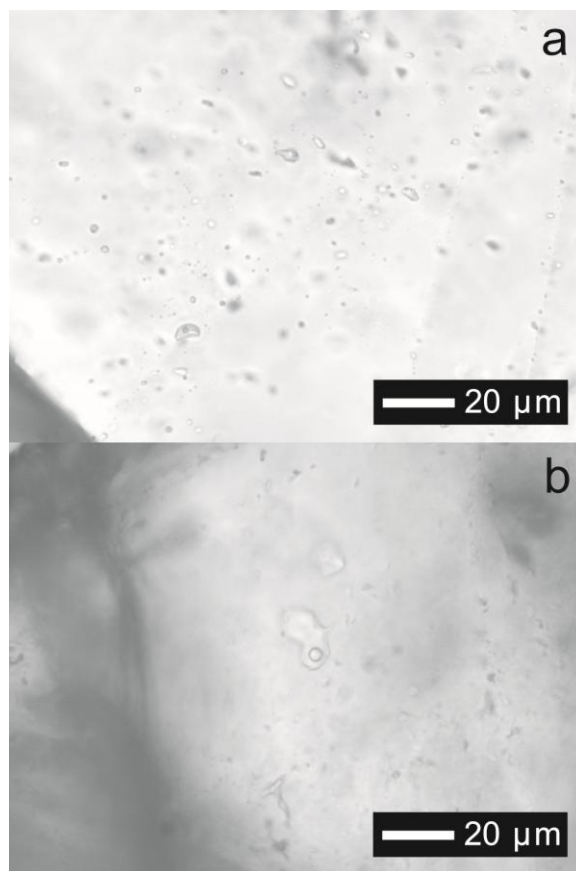


Figure 4-3. Two-phase fluid inclusions from (a) quartz and (b) emerald consist of brine and CO₂-N₂ vapour bubble at room temperature.

The fluid inclusions in emerald and quartz were small and difficult to observe. Additional difficulties included stretching and post-entrapment volume changes due to decrepitation and damage from heating the inclusions. Raman spectrometry confirmed the presence of CO₂ and N₂ in the vapour phase, but neither CH₄ nor H₂S were detected. Microthermometric results are presented in Table 4-1. Upon rapid cooling of the emerald-hosted inclusions, all of which were two-phase, ice and clathrate normally nucleated simultaneously between -57.6 and -95.1°C. Upon heating, the ice was observed to melt between -23.8 and -15.6°C, with two outlying values at -11.4 and -4.8°C (Fig. 4-4a). The clathrate was observed to melt between -11.3 and -7.2°C (Fig. 4-4b). Further heating of the inclusions resulted in homogenization to the liquid phase between 154 and 253°C (Fig. 4-4c). Salinities in CO₂-bearing brine inclusions are difficult to determine. Diamond (1992) defined a technique to estimate salinities based on homogenisation of the carbonic phases and clathrate melting temperatures.

Homogenisation temperatures in the carbonic (vapour) phase of the fluid inclusions was not visible as final homogenisation of the carbonic phase is to the vapour and thus the very small amount of liquid CO₂ in the fluid inclusions is obscured by the brine meniscus and the small size of the inclusions. However we can estimate this value at approximately -6 °C and this has been combined with the observed clathrate melting temperatures to calculate salinities using the Diamond (1992) model. Salinity was determined to be generally greater than 22.2 wt% NaCl equivalent (Diamond 1992).

Table 4-1. Microthermometric data from quartz- and emerald-hosted fluid inclusions from the Mountain River emerald occurrence.

Chip Number	Inclusion Number	Mineral	T _{n(ice)} (°C)	T _{n(cia)} (°C)	T _{m(ice)} (°C)	T _{m(cia)} (°C)	T _{n(total)} (°C)	Salinity (wt%, NaCl equiv.)
DM08-03-01-1	1	quartz	-68.8	-56.0	-21.6	-8.5	-	23.7
	2	quartz	-61.4	-	-21.8	-	189	
	3	quartz	-68.0	-	-22.0	-	220	
	4	quartz	-67.0	-60.5	-22.4	-6.5	-	21.5
	5	quartz	-69.0	-56.0	-22.0	-8.0	250	23.1
	6	quartz	-67.0	-	-22.2	-	221	
	7	quartz	-68.0	-61.0	-22.0	-6.8	224	21.8
	8	quartz	-68.8	-	-22.2	-	232	
	9	quartz	-69.0	-60.0	-21.4	-7.6	141	22.7
	10	quartz	-62.1	-56.7	-22.8	-10.0	184	25.5
	11	quartz	-68.0	-	-22.1	-	328	
DM08-03-01-2	1	quartz	-64.0	-54.0	-22.0	-7.4	156	22.4
	2	quartz	-63.0	-56.0	-22.0	-7.2	-	22.2
	3	quartz	-65.0	-55.0	-22.1	-7.2	218	22.2
	4	quartz	-65.0	-56.0	-22.5	-7.2	230	22.2
	5	quartz	-63.0	-56.0	-22.8	-8.3	251	23.4
	6	quartz	-67.0	-58.0	-22.6	-6.5	-	21.5
	7	quartz	-68.0	-59.0	-22.5	-5.8	210	20.8
	8	quartz	-70.0	-	-22.4	-	258	
	9	quartz	-69.0	-58.0	-22.8	-7.0	230	22.0
	10	quartz	-64.0	-56.0	-22.0	-7.4	221	22.4
	11	quartz	-74.0	-61.0	-22.3	-5.6	224	20.6
DM08-03-03-1	1	quartz	-62.0	-	-22.0	-	218	
	2	quartz	-63.0	-	-22.4	-	197	
	3	quartz	-74.0	-62.0	-21.9	-8.1	-	23.2
	4	quartz	-72.0	-61.0	-22.0	-7.9	236	23.0
	5	quartz	-68.0	-	-21.9	-	182	

	6	quartz	-64.0	-	-22.0	-	137	
	7	quartz	-71.0	-	-22.2	-	228	
	8	quartz	-70.0	-63.0	-22.3	-5.4	103	20.4
	9	quartz	-68.0	-	-22.4	-	213	
DM08-03-2	1	emerald	-72.0	-	-22.0	-	-	
	2	emerald	-68.0	-	-21.9	-	-	
	3	emerald	-75.0	-	-22.0	-	-	
10mh11Ai-2	1	emerald	-76.0	-	-21.4	-10.2	-	25.8
	2	emerald	-	-	-21.4	-	-	
	3	emerald	-	-	-21.3	-	-	
10mh11Ai-3	1	emerald	-	-	-19.5	-8.3	-	23.4
	2	emerald	-85.6	-	-20.2	-	-	
10mh11Ai-4	1	emerald	-76.3	-	-23.7	-	-	
	2	emerald	-68.4	-	-4.8	-	-	
10mh11Ai-5	1	emerald	-71.9	-61.4	-21.6	-8.2	185	23.3
10mh11Ai-6	1	emerald	-90.6	-	-21.4	-	-	-
10mh11Aii-1	1	quartz	-	-56.8	-	-8.8	-	24.0
10mh11Aii-2	1	quartz	-62.9	-57.6	-23.7	-9.4	147	24.8
	2	quartz	-65.7	-58.2	-22.7	-8.8	-	24.0
10mh11Aii-5	1	emerald	-63.4	-	-18.3	-8.2	-	23.3
	2	emerald	-69.2	-	-20.5	-	253	
	3	emerald	-	-59.1	-17.6	-9.8	-	25.3
	4	emerald	-	-	-23.5	-8.5	154	23.7
	5	emerald	-	-	-22.1	-9.5	-	24.9
	6	emerald	-	-	-23.8	-11.3	158	27.4
	7	emerald	-71.7	-	-22.3	-	173	
10mh11Aii-6	1	quartz	-66.4	-	-23.0	-	234	
	2	quartz	-	-61.4	-22.0	-8.6	-	23.8
	3	quartz	-64.3	-	-19.2	-8.8	199	24.0
10mh11Aii-7	1	quartz	-	-68.4	-22.2	-8.8	218	24.0
	2	quartz	-	-63.1	-20.3	-8.0	226	23.1
	3	quartz	-	-	-19.0	-4.8	353	19.8
	4	quartz	-	-	-20.5	-6.5	350	21.5
	5	quartz	-	-54.1	-18.6	-7.6	197	22.7
	6	quartz	-	-61.5	-19.4	-7.2	151	22.2
10mh11Aii-8	1	quartz	-85.4	-	-5.1	-	-	
	2	quartz	-78	-	-16.9	-	139	
	3	quartz	-88	-	-26.1	-	-	
	4	quartz	-87	-	-17.0	-	296	
	5	quartz	-62.2	-	-23.2	-8.8	-	24.0
	6	quartz	-66.4	-	-23.2	-	133	-
	7	quartz	-64	-	-12.2	-7.8	119	22.9
	8	quartz	-70.2	-	-19.4	-5.0	162	20.0

	9	quartz	-63.3	-	-24.0	-8.3	-	23.4
	10	quartz	-63.2	-	-22.4	-	-	
	11	quartz	-66.8	-	-22.7	-8.6	-	23.8
	12	quartz	-78.7	-	-19.1	-	129	
	12	quartz	-	-	-21.0	-	309	
	14	quartz	-62.9	-	-24.0	-5.7	294	20.7
10mh11Aii-9	1	quartz	-63.8	-	-20.2	-7.0	118	22.0
	2	quartz	-	-	-	-	137	
	3	quartz	-62.7	-	-22.3	-	122	
	4	quartz	-76.5	-	-24.1	-	161	

Note: "-" indicates the phase transition was not observed.

cla = clathrate, T_n = phase nucleation temperature, T_m = phase melt temperature, T_h = total homogenization temperature.

Salinity was calculated according to Diamond (1992).

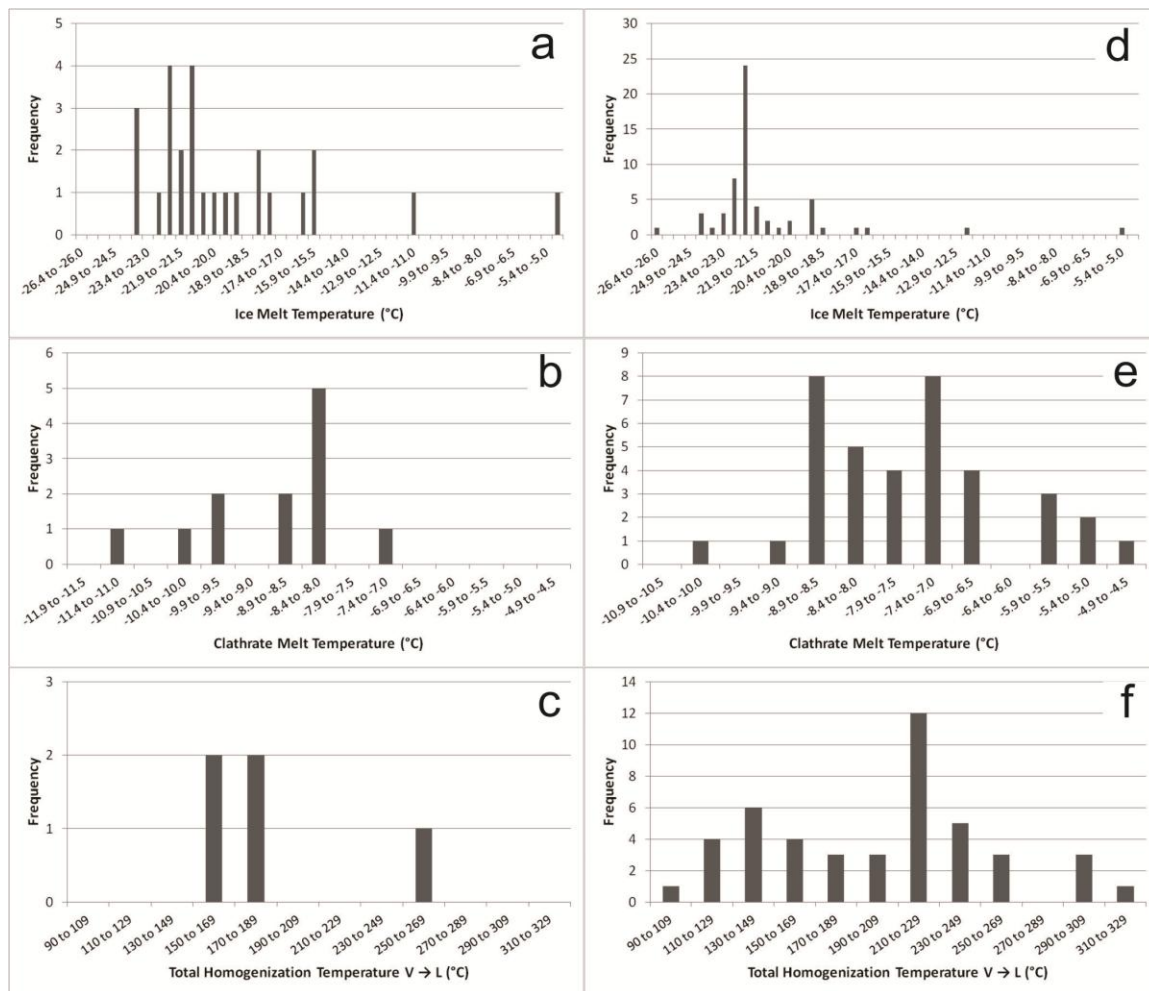


Figure 4-4. Summary of fluid inclusion microthermometry obtained from emerald (a to c) and quartz (d to f) for ice melt temperatures ($T_{m(ice)}$), clathrate melt temperatures ($T_{m(cla)}$), and total homogenisation to the liquid phase ($T_{h(total)}$).

Upon cooling of two-phase FITs in quartz, ice and clathrate normally nucleated simultaneously between -61.4 to -88.0°C. Upon heating ice melted between -26.1 to -16.9°C (Fig. 4-4d), with two outlying melt temperatures at -12.2 and -5.1°C, and clathrate melted between -10.0 and -4.8°C (Fig. 4-4e). From the clathrate melt temperatures, salinity was determined to be generally greater than 19.8 wt% NaCl equivalent (Diamond 1992). Further heating resulted in homogenisation of the inclusions to the liquid phase at temperatures of 103 to 353°C (Fig. 4-4f). Microthermometric measurements of three-phase FITs in quartz were unobtainable as these inclusions all stretched or exploded upon heating at high temperatures.

Many of the emerald-bearing veins display strained or microkinked quartz and emerald, and fractures filled by calcite that cut primary vein minerals. This overprinting texture suggests that some of the fluid inclusions measured potentially represent a secondary fluid overprint associated with deformation or fault activity that postdates mineralization. However, the constant phase ratios and degrees of fill of the inclusions, as well as the clustering of ice and clathrate melt temperatures, support the supposition that the fluid inclusion data represents only one generation of fluid inclusions that we interpret to have formed at or shortly after the time of mineralization, rather than a late secondary overprint.

4.5.2. *Stable isotopes*

Beryl is a cyclosilicate mineral composed of interconnected six-membered rings of silica tetrahedra stacked on top of one another to form structural channels parallel to the *c*-axis (Deer et al. 1997). These channels are wide enough to accommodate water and other fluids, as well as dissolved cations, which can account for several weight percent of the total mass of the crystal. The fluids within these channels, most importantly water, are a sample of the original formational fluids trapped during crystallization (Taylor et al. 1992). Extraction by step-wise heating and subsequent analysis of δD_{H_2O} (Fallick and Barros 1987; Taylor et al. 1992) has been used to distinguish between different emerald deposits around the globe (Giuliani et al. 1997). Results from stable isotope analyses are summarized in Table 4-2.

Table 4-2. *Stable isotope data of quartz, emerald, dolomite, and pyrite collected from emerald-bearing veins*

Sample	Mineral	Yield	$\delta^{18}O$ (‰ VSMOW)	Amount H ₂ O (%)	δD (‰ VSMOW)	$\delta^{13}C$ (‰ VPDB)
Brl:DM08 em80.b	emerald	16.7	16.2	1.8	-65	
10MH01A	emerald	15.2	16.9	2.4	-49	
10MH11A	emerald	16.4	17.2	2.4	-59	
Qtz:DM08 em80.b	quartz	16.8	17.9			
10MH01A	quartz	15.8	18.8			
10MH11A	quartz	17.5	18.9			
10MH11A	dolomite		18.1			-7.4
10MH19D	dolomite		19.5			-5.5
MM3A	dolomite		17.7			-7.8
10MH19D	dolomite		17.2			-6.4

		$\delta^{34}\text{S}$ (‰ CDT)	$\delta^{34}\text{S}_{\text{H}_2\text{S}}$ (‰ CDT)
10MH45A	pyrite	11.2	10.3
10MH01A	pyrite	5.1	4.2
10MH28B	grey gypsum	15.3	
10MH28B	white gypsum	15.1	

Note: $\delta^{34}\text{S}_{\text{H}_2\text{S}}$ is calculated according to Ohmoto and Rye (1979) at 400°C.

Channel water extracted from emerald was found to constitute 1.8 to 2.4 wt% of the crystals, and has $\delta\text{D}_{\text{H}_2\text{O}}$ (VSMOW) values in the range of -65 to -49‰ (Table 4-2). $\delta^{18}\text{O}_{\text{H}_2\text{O}}$ values were calculated according to the equation of Taylor et al. (1992) and determined to be 15.9 to 17.2‰. Structural $\delta^{18}\text{O}$ (VSMOW) of emerald ranges from 16.2 to 17.2‰, and quartz $\delta^{18}\text{O}$ (VSMOW) ranges between 17.9 to 18.9‰. Dolomite was determined to have $\delta^{18}\text{O}$ (VSMOW) between 17.2 to 19.5‰ and $\delta^{13}\text{C}$ (VPDB) between -7.8 to -5.5‰ (Table 4-2).

Mineral pair thermometry based on oxygen isotope partitioning was derived for three quartz-emerald mineral pairs, for a quartz-dolomite pair, and for an emerald-dolomite pair according to the equilibration equations of Zheng (1999) and of Xue et al. (2010). The quartz-emerald calibration gave equilibration temperatures of 379 to 405°C. Quartz-dolomite calibration gave a temperature of 383°C, and the emerald-dolomite calibration gave a temperature of 415°C.

Isotopic analyses of two samples of pyrite have $\delta^{34}\text{S}$ (CDT) of 5.1 and 11.2‰. Calculated $\delta^{34}\text{S}_{\text{H}_2\text{S}}$ for the samples were 4.2 and 10.3‰ respectively, assuming equilibrium fractionation of sulphur and using the isotopic fractionation factors of Ohmoto and Rye (1979) at 400°C, the proposed temperature of emerald crystallization as determined above. Isotopic analyses of gypsum from the Gypsum Formation of the Little Dal Group yield $\delta^{34}\text{S}$ values of 15.1 and 15.2‰.

4.5.3. Geochronology

A sample of quartz-carbonate-emerald vein material with intergrown disseminated dodecahedral pyrite was collected from the Mountain River emerald occurrence for Re-Os dating. In other veins pyrite has been observed within or proximal to emerald crystals. The pyrite grains are interpreted to have grown coevally with emerald. The sample is typical of emerald-bearing veins at the Mountain River occurrence (Fig. 4-5).

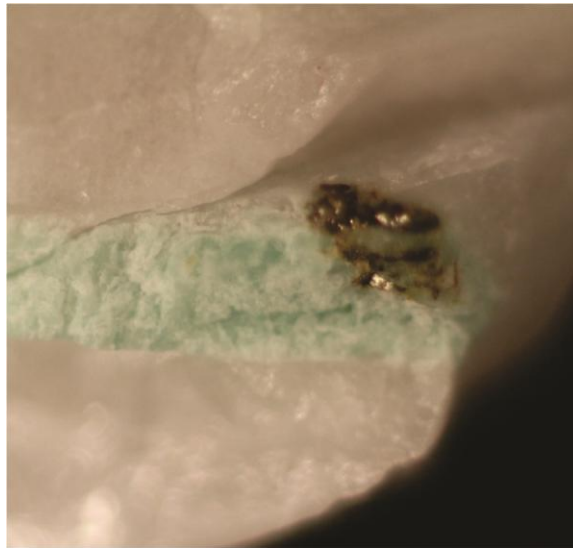


Figure 4-5. *A pyrite grain within emerald is consistent with coeval growth of the two minerals. The pyrite grain is 2 mm in diameter.*

Six Re-Os isotope analyses were performed using methods described in Appendix 1. Measured Re and total Os concentrations are elevated relative to average upper continental crust values (Peucker-Ehrenbrink and Jahn 2001) in all cases (Table 4-3), ranging from 9.4 to 19.4 ppb, and 80.6 to 155.8 ppt, respectively. The pyrite has $^{187}\text{Re}/^{188}\text{Os}$ in the range of 921 to 1739, with radiogenic $^{187}\text{Os}/^{188}\text{Os}$ isotope compositions of 8.6 to 13.6. Five of the six Re-Os analyses yield a well-defined Re-Os isochron with a slope corresponding to a Model 1 age of 345 ± 20 Ma (MSWD = 1.7; Fig. 4-6). The regression defines a reasonably precise Os_i value of 3.2 ± 0.4 .

Table 4-3. Re-Os data from pyrite taken from an emerald-bearing vein.

Sample	Re (ppb)	$\pm 2\sigma$	Total Os (ppt)	$\pm 2\sigma$	$^{187}\text{Re}/^{188}\text{Os}$	$\pm 2\sigma$	$^{187}\text{Os}/^{188}\text{Os}$	$\pm 2\sigma$	ρ
10MH01A-py1	19.42	0.09	155.80	3.90	1476	42	11.31	0.34	0.924
10MH01A-py2a	12.88	0.06	110.60	3.20	1356	45	11.00	0.37	0.989
10MH01A-py2b	13.63	0.06	115.60	2.50	1392	35	11.25	0.28	0.979
10MH01A-py3	10.54	0.05	80.58	7.02	1739	163	13.63	1.28	0.994
10MH01A-py4a	10.34	0.05	96.06	3.36	1198	50	10.18	0.43	0.986
10MH01A-py4b	9.38	0.04	103.00	2.70	921	30	8.56	0.30	0.913

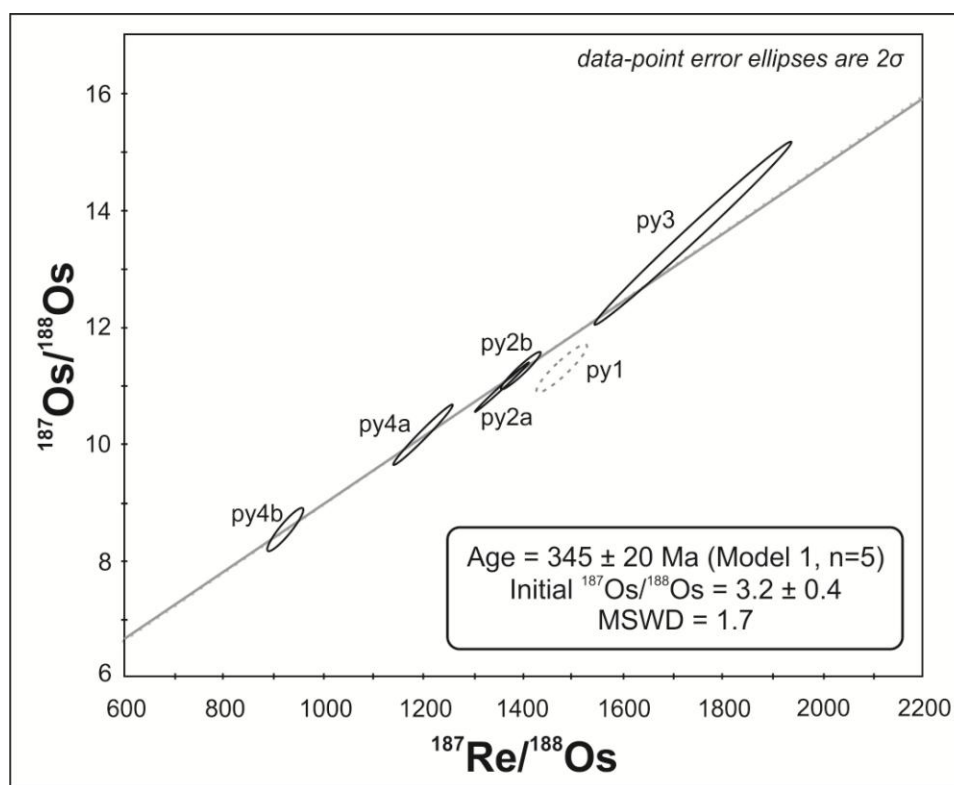


Figure 4-6. Re-Os isochrons derived from quartz-emerald vein-hosted pyrite from the Mountain River emerald occurrence. The solid line is the model 1 isochron using 5 of 6 points reflecting an age of 345 ± 20 Ma ($Os_i = 3.2 \pm 0.4$; MSWD = 1.7). The dashed line is the model 3 isochron of 6 points reflecting an age of 349 ± 80 Ma ($Os_i = 3.1 \pm 1.8$; MSWD = 6.9).

Sample 10MH01A-py1 was excluded from the Model 1 regression as it is not linearly consistent with the other samples. This sample was analysed earlier than the others in a different run and from a different mineral fraction. However, including this sample in the regression results in a Model 3 isochron solution (Fig. 4-6) that is Early Carboniferous in age (349 ± 80 Ma), gives an Os_i value of 3.1 ± 1.8 , and has a large MSWD of 6.9. This is consistent with the more precise five-point regression, indicating a Mississippian age for emerald mineralization.

4.6. Discussion

4.6.1. *Constraints on fluid conditions and source*

The ice nucleation, ice melt, and clathrate melt temperatures were consistent between analyses of quartz and emerald. Two-phase FITs indicate that fluids responsible for emerald mineralization were highly saline (>19.8 wt% NaCl equivalent) CO₂-N₂-bearing brines which homogenised over a wide range of temperatures (103 to 353°C). This wide range could reflect the presence of two or more generations of fluid inclusions, or it could reflect fluid mixing during vein mineralization. These fluid compositions are markedly different than those determined for the other two northern Cordilleran emerald occurrences (Marshall et al. 2003; Marshall et al. 2004). The Mountain River fluid inclusion microthermometric data are comparable to that reported by Gleeson (2006) for quartz-hosted fluid inclusions from the nearby Bear-Twit carbonate-hosted Zn-Pb showing (Fig. 4-7), and may indicate similar fluid conditions between the two occurrences, if not a shared fluid source. However, Gleeson (2006) did not report on the composition of the vapour phase in the fluid inclusions studied, so it is difficult to accurately compare the data from Bear-Twit to Mountain River fluid inclusions.

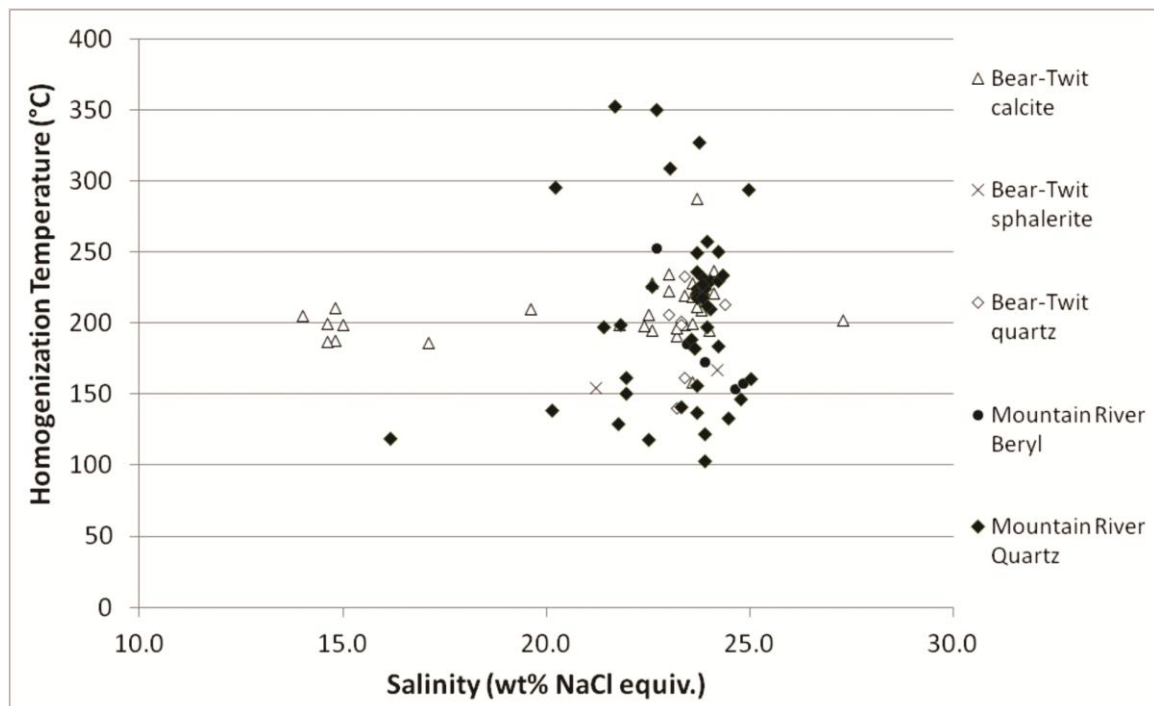


Figure 4-7. Homogenisation temperature versus salinity for calcite-, sphalerite-, quartz-, and emerald-hosted two-phase fluid inclusions from the Mountain River emerald occurrence and Bear-Twit carbonate-hosted Zn-Pb deposit. Bear-Twit data from Gleeson (2006).

Results from isotopic analysis of channel waters from emerald indicate moderately low δD values compared to other emerald deposits. Combined with calculated $\delta^{18}O_{H_2O}$, these values are inconsistent with the isotopic signature of magmatically-derived waters, but within the bounds of both sedimentary and metamorphic waters (Fig. 4-8), thus disqualifying a magmatic fluid source for the Mountain River emeralds. Regional metamorphism in the Mackenzie Mountains is limited and metamorphic grade is sub-greenschist, thus precluding any significant metamorphic fluid source from being involved in emerald mineralization. The most likely fluid source is highly evolved sedimentary waters derived from the greater than 20 km thick succession of sedimentary rocks that make up the Mackenzie Mountains, particularly the underlying Rapitan and Coates Lake groups and the Mackenzie Mountain Supergroup. It is notable that calculated $\delta^{18}O_{H_2O}$ from Mountain River emeralds are skewed toward heavier values, similar to that of Colombian emeralds and a sediment-hosted emerald deposit in Swat, Pakistan. This enrichment in $^{18}O_{H_2O}$ likely is due to isotopic exchange with host sedimentary rocks (Giuliani et al. 1997).

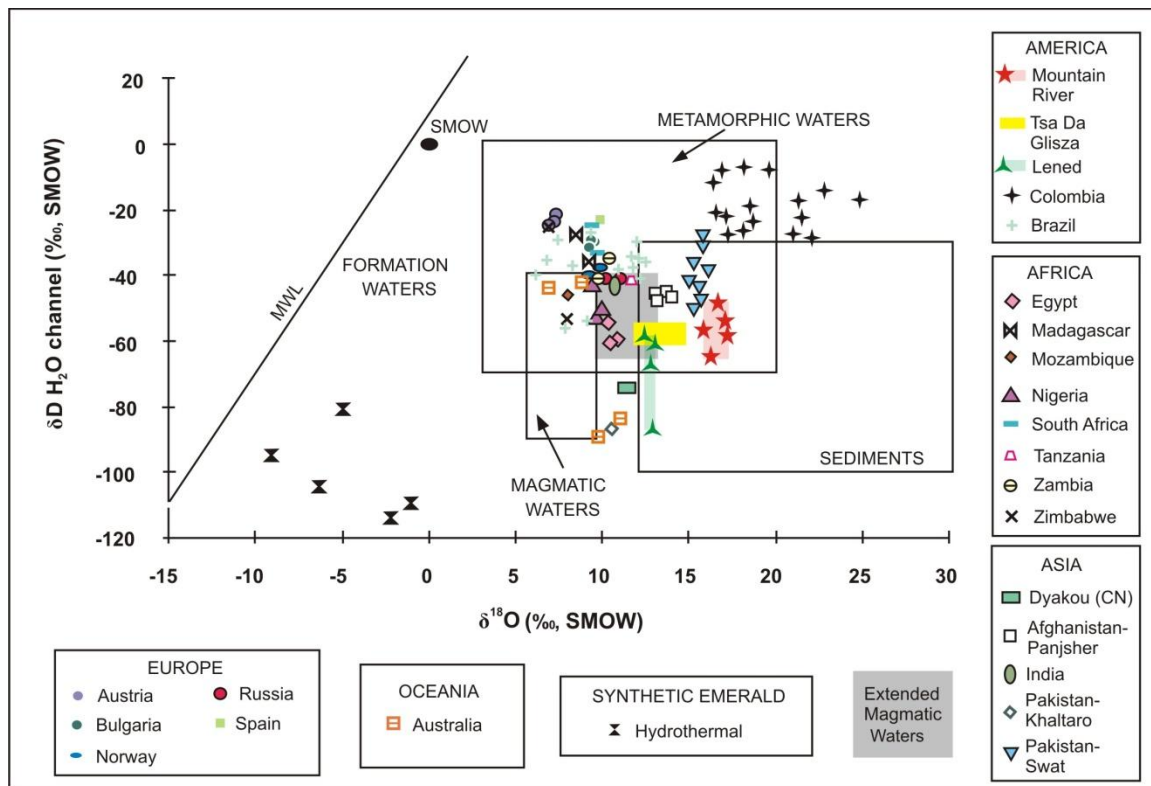


Figure 4-8. Stable isotope ($\delta^{18}\text{O}$ and $\delta^{13}\text{C}$) values from vein dolomite and calcite cogenetic with emerald mineralization from the Mountain River and east and west zones of Colombia. Modified from Giuliani et al. (1997) and Marshall et al (2004).

Cogenetic dolomite sampled from emerald-bearing veins also have $\delta^{18}\text{O}$ values that are skewed towards heavy isotope ratios with a homogenous composition range (17.2 to 19.5‰; Fig. 4-9), which indicates fluid interaction and isotope exchange with host sedimentary rocks (Giuliani et al. 2000). High dolomite $\delta^{13}\text{C}$ values also fall in a relatively narrow range (-7.8 to -5.5‰), indicating that the carbon isotopic composition of the mineralizing fluids is uniform and likely unique. Though the isotopic signature of vein dolomites does not eliminate the possibility of metamorphic fluids contributing to the mineralizing system at Mountain River, the absence of significant metamorphism indicates that metamorphism would be an unlikely source of fluids. Relatively high dolomite $\delta^{13}\text{C}$ ratios can be produced by isotope exchange with dissolved carbon species generated through dissolution of limestones, while very low $\delta^{13}\text{C}$ ratios can be produced by isotopic exchange with light organic carbon or hydrocarbons (Giuliani et al. 2000). Carbon isotope ratios from veins at Mountain River are too low to be exclusively derived from marine limestones (Fig. 4-9), so it is possible that a trace amount of

isotopically light organic matter or hydrocarbons interacted with mineralizing fluids, although no evidence for organic matter or hydrocarbons has been observed. High $\delta^{13}\text{C}$ are comparable to isotope ratios found in the western zone Colombian emerald veins (Giuliani et al. 2000). High $\delta^{13}\text{C}$ values at Mountain River, as at the Colombian deposits, may reflect interaction of mineralizing fluids with local limestone or evaporite units. However, a sedimentary source alone would result in higher $\delta^{13}\text{C}$ values than were determined for the Mountain River veins. Given the low TOC content (generally less than 0.4% TOC) of the Twitya Formation and other rocks in the Mackenzie Mountains (MacNaughton et al. 2008) and the lack of evidence for pyrobitumen or other organic material at the Mountain River occurrence, it is possible but unlikely that minor organic sources contributed a small amount of light carbon to the mineralizing fluid. High $\delta^{18}\text{O}$ values are comparable to the Manetoe facies dolomite isotope trend (Morris and Nesbitt 1998; Nelson et al. 2002), but excursions to lower $\delta^{13}\text{C}$ values as in the Swan Hills dolomite cements may be attributable to sulphate reduction (Nelson et al. 2002). Thermochemical sulphate reduction is likely the redox mechanism responsible for this isotopic character and by proxy, emerald mineralization, at Mountain River, and inorganic reduction by iron (Ohmoto and Rye 1979) may have played the dominant role, as evidence for organic matter is lacking. It is possible that minor amounts of organic matter may have been oxidized to produce H_2S and therefore played a minor role in sulphate reduction.

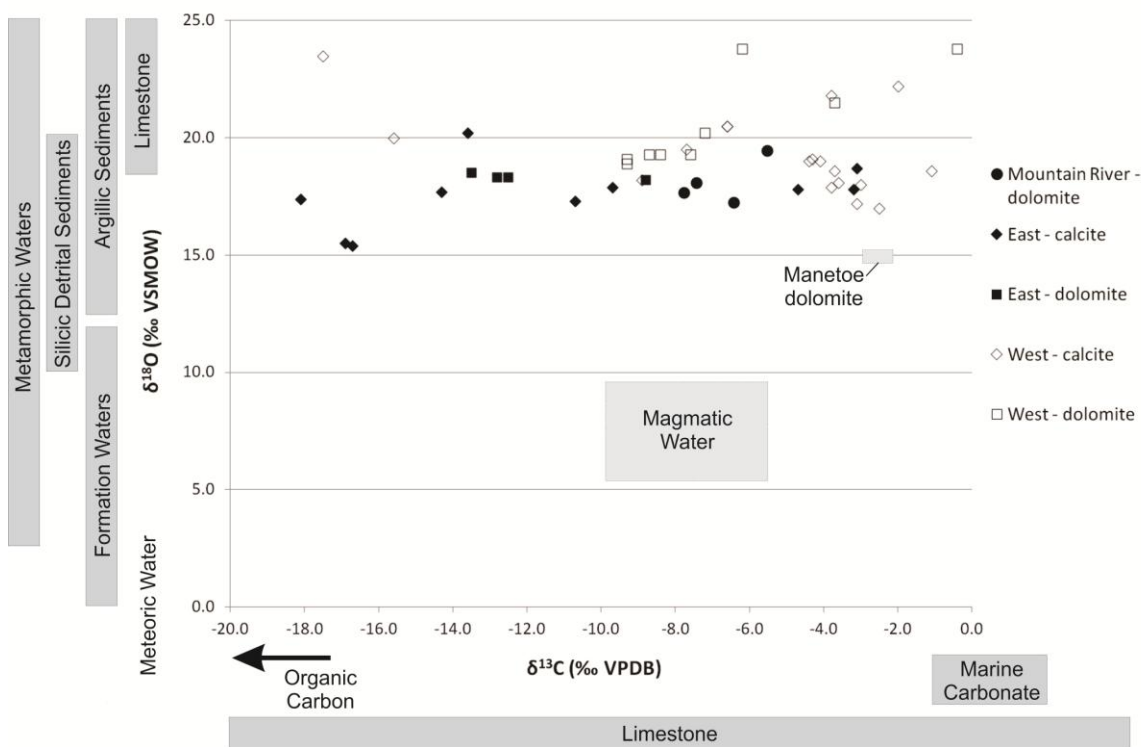


Figure 4-9. Stable isotope ($\delta^{18}\text{O}$ and $\delta^{13}\text{C}$) values from vein dolomite and calcite cogenetic with emerald mineralization from the Mountain River and east and west zones of Colombia (modified from Hunt et al. 2011). Colombian data from Giuliani et al. (2000).

Calculated $\delta^{34}\text{S}_{\text{H}_2\text{S}}$ from coeval pyrite reveal a mineralizing fluid that was enriched in the heavier isotope, characteristic of sedimentary and evaporitic sulphur sources (Giuliani et al. 1995). Evaporitic and evaporite-bearing units occur within the Little Dal and Coates Lake groups underlying the Twitya Formation (Aitken 1991; Narbonne and Aitken 1995). 500 m thick beds of the Gypsum Formation in the Little Dal Group are composed of white gypsum and anhydrite interbedded with shale, while the 1200 m thick Redstone River Formation of the Coates Lake Group is variably evaporitic, with beds of gypsum and gypsumiferous siltstone grading up into interbedded mudstone, evaporites, and carbonate rocks (Narbonne and Aitken 1995; Gordey et al. 2011a). The sulphur isotope composition of hydrothermal fluids involved in mineralization must be as heavy as or heavier than the calculated $\delta^{34}\text{S}_{\text{H}_2\text{S}}$ from pyrite (Giuliani et al. 1995). The calculated $\delta^{34}\text{S}_{\text{H}_2\text{S}}$ values at Mountain River are lighter than the evaporites indicating that the evaporites are a permissible source of sulphur.

The high initial osmium ratio (Os_i) for pyrite provides insight into the source of Os and possibly other metals, including V and Cr, for the mineralizing fluid. An elevated Os_i value obtained from Re-Os pyrite analyses reflecting a strong crustal contribution of Os and other metals to the hydrothermal system provides further evidence of the basinal source of the mineralizing fluid. The value (3.2 ± 0.4) is quite radiogenic and highly elevated above primitive upper mantle (0.1296; Meisel et al. 2001) and even above average upper continental crust $^{187}Os/^{188}Os$ (1.40; Peucker-Erhenbrink and Jahn 2001), indicating a strong crustal contribution of radiogenic Os to the hydrothermal system. This dominant crustal contribution is not surprising considering the greater than 20 km thickness of the sedimentary pile that makes up the Mackenzie Platform in the study area (Aitken 1991; Morrow 1991), the strata being derived from recycling of older Laurentian crustal terranes (e.g. Rainbird et al. 1992; Hadlari et al. 2012). Extremely radiogenic Os_i values are also reported from organic-rich black shales and crude oils (Kendall et al. 2006; Selby et al. 2007), raising the possibility that the high Os_i value of Mountain River pyrite is due to the interaction and reduction of sulphate by organic matter. However, black shale source rocks possess more radiogenic osmium ratios with increasing age, so the Os_i ratios of hydrocarbons may simply reflect source rock age and not necessarily a direct relationship to organic matter (Selby et al. 2007).

The pressure conditions of mineralization for the Mountain River veins can be determined from isochores derived from combining fluid inclusion measurements and the Bowers and Helgeson (1983) equation of state (Fig. 4-10). The light grey field represents the two-phase field or zone of boiling for the vein fluids. The dark grey field represents the intersection of the fluid inclusion isochore constraints with the stable isotope mineral pair thermometry to limit temperatures to 379 to 415°C, indicating pressures of 2.4 to 4.0 kbar which correspond to depths of 9 to 15 km, assuming an average rock density of 2.7 g/cm³. Given a modern geothermal gradient of 38°C/km and a maximum of 65°C/km during the Paleozoic (Morrow et al. 1993), the burial depths of the Twitya Formation (greater than 7 km deep in the stratigraphic package) and Little Dal Group (greater than 11 km; Narbonne and Aitken 1995; MacNaughton et al. 2008; Pyle 2008; Gordey et al. 2011b) are deep enough that fluid movement at these depths could have produced fluids of the temperature required for emerald mineralization. In this model high fluid salinities reflect basinal fluid interaction with evaporites, such as

gypsumiferous units of the Little Dal or Coates Lake groups, with scavenging of Be, V, Sc, Cr, Os, and other metals from local sedimentary rocks. Heat advection via fluid ascent along reactivated basement structures maintained the temperatures required for emerald mineralization at shallower depth in the Twitya Formation (Fig. 4-11a). This model is consistent with fluid inclusion and stable isotope results reflecting salinities, $\delta^{18}\text{O}$, δD , $\delta^{13}\text{C}$, $\delta^{34}\text{S}$, and Os_i values typical of radiogenic sedimentary-derived brines, and conditions of mineralization on the order of 379 to 415°C, 2.4 to 4.0 kbar pressure, and depths of 9 to 15 km. These fluids are similar to those attributed for emerald mineralization in Colombia (Ottaway et al. 1994; Giuliani et al. 2000; Banks et al. 2000). The carbon isotope signature and Os_i ratio hint at a possible interaction of mineralizing fluids with organic matter. However, unlike at the Colombian emerald deposits, the complete absence of pyrobitumen, methane, or any other organic material in the host rocks and veins indicates that organic matter, if present, played a very minor role in mineralizing fluid evolution. The inorganic reduction of sulphate to sulphide, and subsequent mineralization, was likely facilitated by the iron-rich host sediments of the Twitya Formation, the Rusty Shale Formation of the Little Dal Group, or iron formation of the Rapitan Group (Ohmoto and Rye 1979).

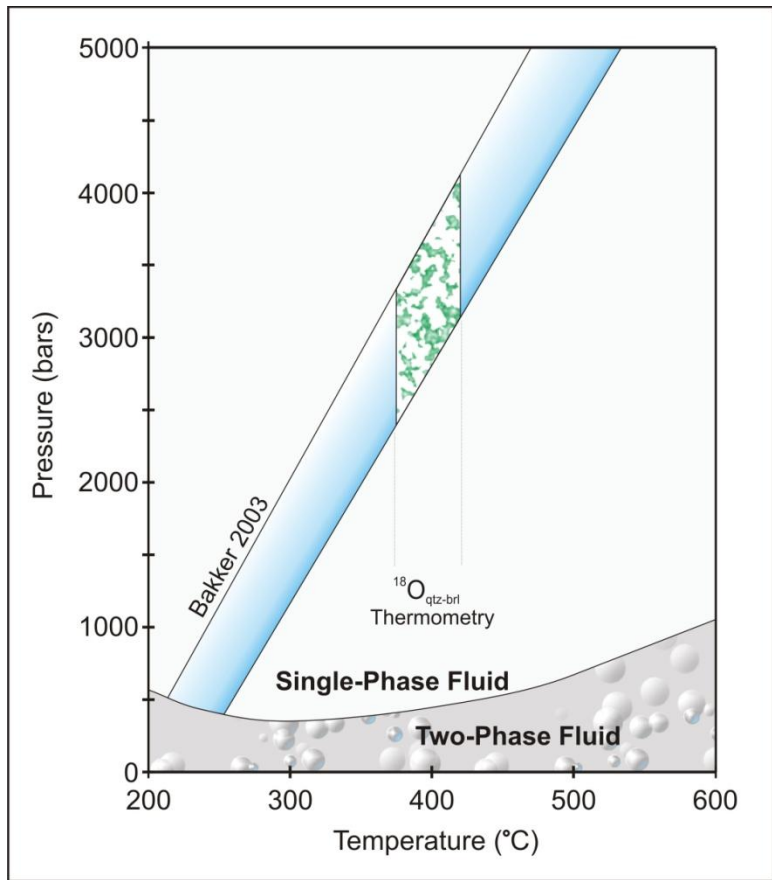


Figure 4-10. Pressure-temperature diagram showing the range of formational conditions for the Mountain River veins. The isochores (solid lines) are derived from fluid inclusion measurements and the Bowers and Helgeson (1983) equation of state via Bakker (2003). The light grey area represents the two-phase field or zone of boiling for the vein fluids. The dark grey area represents the intersection of fluid inclusion isochoric constraints with stable isotope thermometry to limit temperatures to 379 to 415°C and pressures of 2.4 to 4.0 kbar.

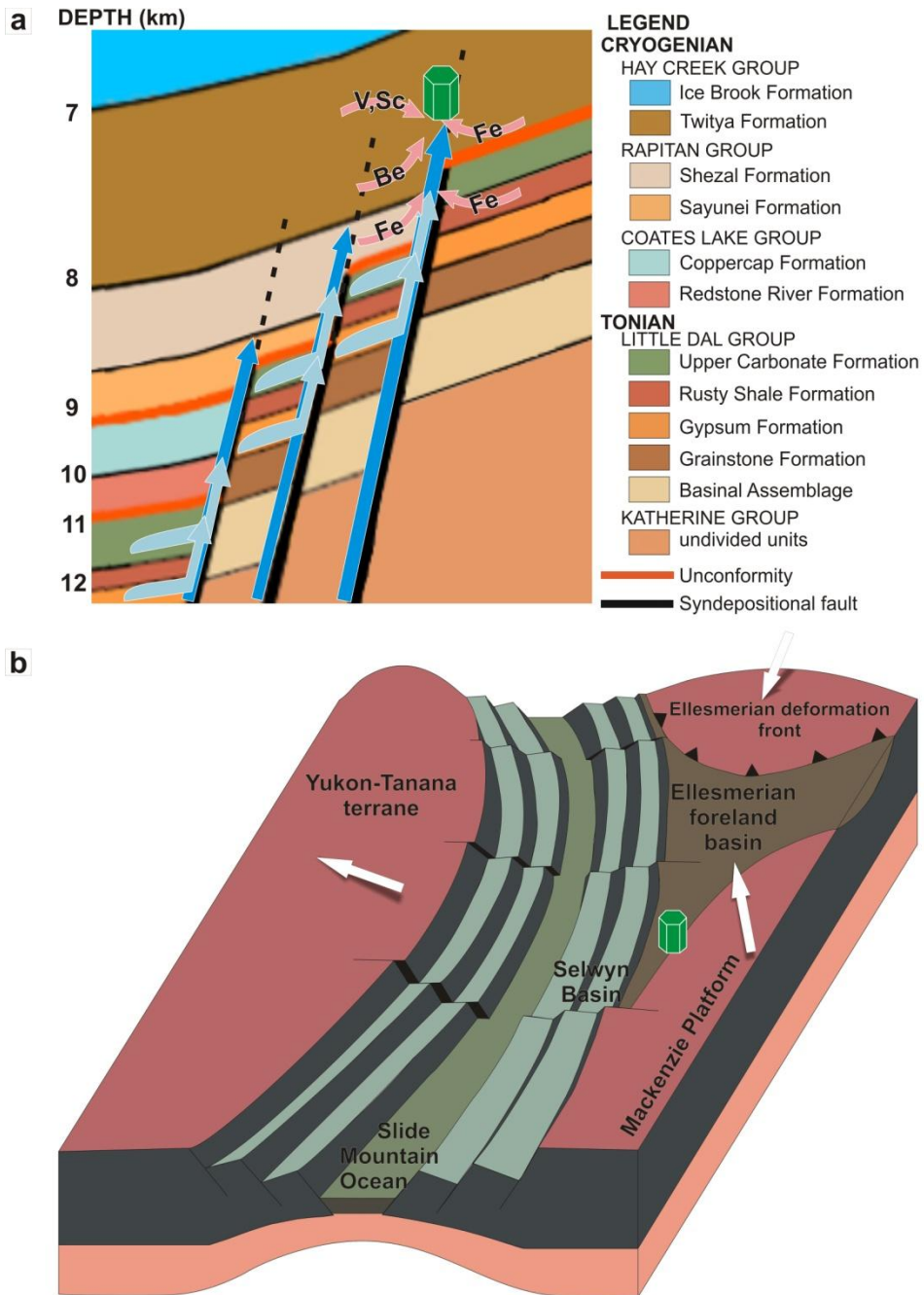


Figure 4-11. Tectonic model at the time of emerald mineralization, ca. 345 Ma. a) Fluid circulation model for the mineralization of the Mountain River emerald occurrence. Modified from Gordey et al. 2011b. b) Late Devonian to Mississippian tectonic model showing the Mackenzie Platform of Laurentia in relation to the limit of Ellesmerian deformation and the Yukon-Tanana terrane. The green emerald shows the paleo-location of the Mountain River emerald occurrence. Modified after Nelson et al. (2006), Lund (2008), Beranek et al. (2010), and Lemieux et al. (2011).

4.6.2. Constraints on the timing of mineralization

The 345 ± 20 Ma Re-Os pyrite date is considered here to record the timing of emerald mineralization. The uncertainty associated with this isochron (20 Ma, or ~5.8%, 2σ) is likely a function of the limited range of the $^{187}\text{Re}/^{188}\text{Os}$ ratios (921.3 to 1739). Despite this, the isochron interpreted to represent the age of emerald mineralization at the Mountain River showing is demonstrably Late Devonian to Middle Mississippian and indicates that the Re-Os pyrite geochronometer could be useful in determining the timing of emerald mineralization at other localities. The timing of mineralization is contemporaneous with estimated ages of the extensive Manetoe Facies dolomitization (Morrow and Aulstead 1995; Morris and Nesbitt 1998; Al-Aasm et al. 2002), a significant base metal mineralization event at the end of the Devonian to the Mississippian (including VHMS, SEDEX, and carbonate-hosted Zn-Pb deposits; Nelson et al. 2002; Nelson and Colpron 2007; Lund 2008; and references therein), and oil and gas generation to the east (Pyle 2008). It is postulated here that the Mountain River emeralds formed from the same fluids involved in some of the Zn-Pb mineralization and Manetoe Facies dolomitization.

The Mississippian age puts the timing of emerald mineralization on the stable platform side of a back-arc basin environment (Fig. 4-11b) (Colpron et al. 2007). Following the northern Cordilleran metallogenic model proposed by Nelson et al. (2002), this period of extension and high-temperature fluid flow drove brines eastward toward the platform along basement structures and reactivated faults, in this case resulting in emerald mineralization. Thrusting along the Shale Lake fault during later Cretaceous-Tertiary deformation placed the emeralds structurally above Devonian strata of the Arnica Formation and exposed them at the surface. This event resulted in the brittle deformation preserved in the crystals.

Several authors have proposed a brief period of compressional tectonic activity during the Devonian-Mississippian along the western Laurentian margin (Gordey et al. 1987; Smith et al. 1993; Root 2001) that is contemporaneous with the Antler Orogeny further to the south and the Ellesmerian Orogeny to the north-northeast (Lane 2007; Beranek et al. 2010). Their interpretations have been difficult to integrate with tectonic models that describe a purely extensional back-arc basin environment generated by the

rifting away of the Yukon-Tanana terrane and opening of the Slide Mountain Ocean beginning in the Latest Devonian (Colpron et al. 2007; Piercey and Colpron 2009). We suggest that the fluid movement responsible for emerald (and by proxy, base metal) mineralization was generated by the jostling of tectonic blocks via normal and reverse faulting in a transtensional back-arc basin combined with the far-field effects of the Ellesmerian Orogeny (Fig. 4-11b). Basement faults acted as hydraulic pumps drawing down and squeezing up hot, deep-seated, basinal fluids. These fluids may have been rich in Be, V, Sc, and other components when they were first generated from very deep in the sedimentary succession or possibly from metamorphosing basement rocks. However, considering the thickness of the sedimentary succession and the salinity of the fluid inclusions, it is more likely that the mineralizing fluids were derived from or interacted heavily with dewatering sedimentary rocks. The fluids scavenged CO₂, N₂, sulphate, metals, and salts upon ascension until they reached structurally favourable sites and reacted with iron to inorganically reduce sulphate to sulphide, causing dissolved components to precipitate out of solution in extensional veins formed by hydraulic fracturing as pyrite, carbonate, quartz, and emerald.

4.6.3. A Colombian-like mineralization model

The regional geology and location of the emeralds within largely unmetamorphosed siliciclastic rocks indicates that the Mountain River emeralds may be genetically comparable to the emerald deposits of Colombia. The Colombian emeralds are related to the thrusting and inversion of a Jura-Cretaceous back-arc basin and accompanying hydrothermal fluid circulation in the Colombian Andes during Paleogene orogenesis (Cheilletz et al. 1994). Our Re-Os pyrite date indicates that mineralization occurred during basin extension or transtension, rather than orogenesis, during the Early Mississippian. The geochemical model presented here for Mountain River emerald mineralization is similar to models proposed for Colombian emerald mineralization, except that Colombian mineralization was dependent on organic sulphate reduction, while evidence of organic matter is absent at Mountain River. The verification of the Mountain River occurrence as a Colombian-like emerald occurrence is important for gem emerald exploration in the northern Cordillera as this deposit type occurs in districts rather than as discrete individual deposits. It also sheds light on the relationship between

emerald and base metal mineralization, a point raised by Ottaway et al. (1994) who speculated on a possible relationship of nearby Pb-Zn occurrences to the Colombian emerald deposits.

4.7. Conclusions

The Mountain River emerald veins are hosted within siliciclastic strata in the hangingwall of the Shale Lake thrust fault. The strata exhibit sub-greenschist facies metamorphism, but are pervasively carbonatized and variably pyritized, and have experienced brittle deformation resultant from Cretaceous-Tertiary thrusting and folding. Mineralization occurred at temperatures of 380 to 415°C and pressures of 2.4 to 4.0 kbar, which correspond to depths of 9 to 15 km. Low δD and high $\delta^{18}O$ of water derived from emerald coupled with moderate $\delta^{18}O$ and $\delta^{13}C$ from dolomite indicate that these fluids were not derived from magmatic sources. Calculated $\delta^{34}S_{H_2S}$ from pyrite indicates that sulphur in the fluids was derived from a sedimentary or evaporitic source. The fluids responsible for mineralization were deep-seated, highly saline (>19.8 wt% NaCl equivalent) CO_2 - N_2 -bearing brines that leached the chemical components necessary for emerald mineralization from local strata. The veins have been dated by a pyrite Re-Os isochron to be Mississippian in age (345 ± 20 Ma) with a high Os_i indicating the fluids either were derived from or interacted extensively with rocks of the local sedimentary succession. Inorganic sulphate reduction by iron likely played a role in mineralization at the Mountain River occurrence, rather than sulphate reduction by organic matter as at the Colombian emerald deposits. This model of emerald mineralization is most similar to the type 3 model used to describe the emerald zones of Colombia and is a unique mineralization style in the northern Cordillera.

4.8. Acknowledgements

The authors gratefully acknowledge the contributions of M. Mercier, E. Martel, C. Ozyer, S. Gordey, H. Falck, J. Ketchum, and A. Lalonde to the project. K. Klassen, A. Vuletich, P. Alexandre, K. Kyser, and the Queen's Facility for Isotope Research are thanked for stable isotope analyses. The authors acknowledge funding and field support

provided by the Northwest Territories Geoscience Office (contribution #0061), as well as scholarships and grants to MH and DM from the Natural Sciences and Engineering Research Council of Canada, Society of Economic Geologists Canada, and the Northern Scientific Training Program.

References

- Aitken, J. D. 1991. The Ice Brook Formation and post-Rapitan, Late Proterozoic glaciation, Mackenzie Mountains, Northwest Territories. Geological Survey of Canada Bulletin, 404.
- Al-Aasm, I.S., Lonnee, J.S., and Clarke, J. 2002. Multiple fluid flow events and the formation of saddle dolomite: case studies from the Middle Devonian of the Western Canada Sedimentary Basin. *Marine and Petroleum Geology*, **19**: 209-217.
- Bakker, R.J. 2003. Adaptation of the Bowers and Helgeson (1983) equation of state for the H₂O–CO₂–CH₄–N₂–NaCl system. *Chemical Geology*, **154**: 225-236.
- Beranek, L. P., Mortensen, J. K., Lane, L. S., Allen, T. L., Fraser, T. A., Hadlari, T., and Zantvoort, W. G. 2010. Detrital zircon geochronology of the western Ellesmerian clastic wedge, northwestern Canada: on Arctic tectonics and the evolution of the northern Cordilleran miogeocline. *GSA Bulletin*, **122**(11/12): 1899-1911.
- Banks, D.A, Giuliani, G., Yardley, B.W.D., and Cheilletz, A. 2000. Emerald mineralisation in Colombia: fluid chemistry and the role of brine mixing. *Minerallium Deposita*, **35**: 699-713.
- Bowers, T. S., and Helgeson, H. C. 1983. Calculation of the thermodynamic and geochemical consequences of nonideal mixing in the system H₂O–CO₂–NaCl on phase-relations in geologic systems - equation of state for H₂O–CO₂–NaCl fluids at high-pressures and temperatures. *Geochimica et Cosmochimica Acta*, **47**(7): 1247-1275.
- Cheilletz, A., Féraud, G., Giuliani, G., and Rodriguez, C. T. 1994. Time-pressure and temperature constraints on the formation of Colombian emeralds: An ⁴⁰Ar/³⁹Ar laser microprobe and fluid inclusion study. *Economic Geology*, **89**: 361-380.
- Colpron, M., Nelson, J. L., and Murphy, D. C. 2007. Northern Cordilleran terranes and their interactions through time. *GSA Today*, **17**(4/5): 4-10.
- Deer, W.A., Howie, R.A., and Zussman, J. 1997. *Rock-forming minerals: Disilicates and Ring Silicates*, v. 1B (2nd edition). The Geological Society Publishing House, Bath, UK.
- Diamond, L.W. 1992. Stability of CO₂ clathrate hydrate + CO₂ liquid + CO₂ vapour + aqueous KCl–NaCl solutions: Experimental determination and application to salinity estimates of fluid inclusions. *Geochimica et Cosmochimica Acta*, **56**: 273-280.
- Fallick, A. E., and Barros, J. G. 1987. A stable- isotope investigation into the origin of beryl and emerald from the Porangatu deposits, Goias State, Brazil. *Chemical Geology*, **66**: 293-300.

- Giuliani, G., Cheilletz, A., Arboleda, C., Carrillo, V., Rueda, F., and Baker, J. H. 1995. An evaporitic origin of the parent brines of Colombian emeralds: fluid inclusion and sulphur isotope evidence. *European Journal of Mineralogy*, **7**: 151-165.
- Giuliani, G., France-Lanord, C., Zimmerman, J. L., Cheilletz, A., Arboleda, C., Charoy, B., Coget, P., Fontan, F., and Giard, D. 1997. Fluid composition, δD of channel H_2O , and $\delta^{18}O$ of lattice oxygen in beryls: Genetic implications for Brazilian, Colombian, and Afghanistani emerald deposits. *International Geology Reviews*, **39**: 400-424.
- Giuliani, G., France-Lanord, C., Cheilletz, A., Yannick-Branquet, P. C., and Laumonnier, B. 2000. Sulfate reduction by organic matter in Colombian emerald deposits: Chemical and stable isotope (C, O, H) evidence. *Economic Geology*, **95**: 1129-1153.
- Gleeson, S. 2006. A microthermometric study of fluid inclusions in sulphides and carbonates from Gayna River and the Bear-Twit base metal prospects, Mackenzie Mountains, NWT. Northwest Territories Geoscience Office, NWT Open Report 2006-005, 9 p.
- Goldstein, R., and Reynolds, T.J. 1994. Systematics of fluid inclusions in diagenetic minerals. SEPM short course 31, 199 p.
- Gordey, S. P., Abbott, J. G., Tempelman-Kluit, D. J., and Gabrielse, H. 1987. "Antler" clastics in the Canadian Cordillera. *Geology*, **15**: 103-107.
- Gordey, S. P., Martel, E., Fallas, K., Roots, C. F., MacNaughton, R., and MacDonald, J. 2011a. Geology of Mount Eduni, NTS 106A Southwest, Mackenzie Mountains, Northwest Territories; Northwest Territories Geoscience Office, NWT Open File 2010-11 (Edition 2). 1 map, scale 1:100,000.
- Gordey, S.P., MacDonald, J.D., Roots, C.F., Fallas, K., and Martel, E. 2011b. Regional cross-sections, detachment levels and origin of the Plateau fault, central Mackenzie Mountains, Northwest Territories; Northwest Territories Geoscience Office, NWT Open File 2010-18. 1 sheet, scale 1:100,000.
- Groat, L. A., Marshall, D. D., Giuliani, G., Murphy, D. C., Piercey, S. J., Jambor, J. L., Mortensen, J. K., Ercit, T. S., Gault, R. A., Matthey, D. P., Schwarz, D., Maluski, H., Wise, M. A., Wengzynowski, W., and Eaton, D. W. 2002. Mineralogical and geochemical study of the Regal Ridge emerald showing, Southeastern Yukon. *Canadian Mineralogist*, **40**: 1313-1338.
- Hadlari, T., Davis, W.J., Dewing, K., Heaman, L.M., Lemieux, Y., Ootes, L., Pratt, B.R., and Pyle, L.J. 2012. Two detrital zircon signatures for the Cambrian passive margin of Laurentia highlighted by new U-Pb results from northern Canada. *Geological Society of America Bulletin*, **124**: 1155-1168. doi: 10.1130/B30530.1.

- Hunt, J. A., Baker, T., Cleverly, J., Davidson, G. J., Fallick, A. E., and Thorkelson, D. J. 2011. Fluid inclusion and stable isotope constraints on the origin of Wernecke Breccia and associated iron oxide-copper-gold mineralization, Yukon. *Canadian Journal of Earth Sciences*, **48**: 1425-1445.
- Kendall, B., Creaser, R. A., and Selby, D. 2006. Re-Os geochronology of postglacial black shales in Australia: Constraints on the timing of "Sturtian" glaciation. *Geology*, 34(9): 729-732.
- Lane, L. S. 2007. Devonian-Carboniferous paleogeography and orogenesis, northern Yukon and adjacent Arctic Alaska. *Canadian Journal of Earth Sciences*, **44**: 679-694.
- Lemieux, Y., Hadlari, T., and Simonetti, A. 2011. Detrital zircon geochronology and provenance of Devonian-Mississippian strata in the northern Canadian Cordilleran miogeocline. *Canadian Journal of Earth Sciences*, **48**: 515-541.
- Lund, K. 2008. Geometry of the Neoproterozoic and Paleozoic rift margin of western Laurentia: Implications for mineral deposit settings. *Geosphere*, **4**(2): 429-444.
- Marshall D., Groat L., Giuliani G., Murphy D., Matthey D., Ercit T.S., Wise M., Wengzynowski W., and Eaton W.D. 2003. Pressure, temperature and fluid conditions during emerald precipitation, southeastern Yukon, Canada: Fluid inclusion and stable isotope evidence. *Chemical Geology*, **194**: 187-199.
- Marshall, D., Groat, L. A., Falck, H., Giuliani, G., and Neufeld, H. 2004. The Lened emerald prospect, Northwest Territories, Canada: Insights from fluid inclusions and stable isotopes, with implications for northern Cordilleran emerald. *Canadian Mineralogist*, **42**: 1523-1539.
- MacNaughton, R. B., Fallas, K., and Zantvoort, W. 2008. Qualitative assessment of the Plateau Fault (Mackenzie Mountains, NWT) as a conceptual hydrocarbon play. Geological Survey of Canada, Open File 5831, 29 p.
- Meisel, T., Walker, R. J., Anthony, J. I., and Lorand, J.-P. 2001. Osmium isotopic compositions of mantle xenoliths: A global perspective. *Geochimica et Cosmochimica Acta*, **65**(8): 1311-1323.
- Mercier, M. 2008. Geology and mineralogy of the Mountain River Beryl (variety emerald) showing, Mackenzie Mountains, Northwest Territories, Canada. B.Sc. thesis, Department of Earth Sciences, University of Ottawa, Ottawa, ON.
- Morris, G. A., and Nesbitt, B. E. 1998. Geology and timing of palaeohydrogeological events in the Mackenzie Mountains, Northwest Territories, Canada. *In* Dating and Duration of Fluid Flow and Fluid-Rock Interaction. *Edited by* J. Parnell. Geological Society, London, Special Publications, v. 144, p. 161-172.
- Morrow, D. W. 1991. The Silurian-Devonian sequence in the northern part of the Mackenzie Shelf, Northwest Territories. Geological Survey of Canada, Bulletin 413, 121 p.

- Morrow, D. W., Potter, J., Richards, B., and Goodarzi, F. 1993. Paleozoic burial and organic maturation in the Liard Basin Region, northern Canada. *Bulletin of Canadian Petroleum Geology*, **41**(1): 17-31.
- Morrow, D. W., and Aulstead, K. L. 1995. The Manetoe Dolomite – a Cretaceous-Tertiary or Paleozoic event? Fluid inclusion and isotopic evidence. *Bulletin of Petroleum Geology*, **43**(3):267-280.
- Narbonne, G. M., and Aitken, J. D. 1995. Neoproterozoic of the Mackenzie Mountains, northwestern Canada. *Precambrian Research*, **73**: 101-121.
- Nelson, J., and Colpron, M. 2007. Tectonics and metallogeny of the British Columbia, Yukon and Alaskan Cordillera, 1.8 Ga to the present. *In Mineral Deposits of Canada: A Synthesis of Major Deposit Types, District Metallogeny, the Evolution of Geological Provinces, and Exploration Methods. Edited by W. D. Goodfellow. Geological Association of Canada, Mineral Deposits Division, Special Publication No. 5, p. 755-791.*
- Nelson, J., Paradis, S., Christensen, J., and Gabites, J. 2002. Canadian Cordilleran Mississippi Valley-Type deposits: A case for Devonian-Mississippian back-arc hydrothermal origin. *Economic Geology*, **97**: 1013-1036.
- Nelson, J.L., Colpron, M., Piercey, S.J., Dusel-Bacon, C., Murphy, D.C. and Roots, C.F. 2006. Paleozoic tectonic and metallogenic evolution of the pericratonic terranes in Yukon, northern British Columbia and eastern Alaska. *In Paleozoic Evolution and Metallogeny of Pericratonic Terranes at the Ancient Pacific Margin of North America, Canadian and Alaskan Cordillera. Edited by M. Colpron and J. L. Nelson. Geological Association of Canada, Special Paper 45, p. 323-360.*
- Ohmoto, H., and Rye, R. O. 1979. Isotopes of sulfur and carbon. *In Geochemistry of Hydrothermal Ore Deposits (2nd edition). Edited by H.L. Barnes. Wiley, New York, pp. 509-561.*
- Ottaway, T. L., Wicks, F. J., Bryndzia, L. T., Kyser, T. K., and Spooner, E. T. C. 1994. Formation of the Muzo hydrothermal emerald deposit in Colombia. *Nature*, **369**(6481): 552-554.
- Piercey, S. J., and Colpron, M., 2009. Composition and provenance of the Snowcap assemblage, basement to the Yukon-Tanana Terrane, northern Cordillera: Implications for Cordilleran crustal growth. *Geosphere*, **5**(5): 439-464.
- Peucker-Ehrenbrink, B., and Jahn, B.-M. 2001. Rhenium-osmium isotope systematics and platinum group element concentrations: Loess and the upper continental crust. *Geochemistry, Geophysics, Geosystems [electronic]*, v. 2, ISSN: 1525-2027.
- Pyle, L. J. 2008. Petroleum play data for the Lower Paleozoic platform play (Ronning Group), Mackenzie Corridor. Geological Survey of Canada, Open File 5667, 1 CD-ROM.

- Rainbird, R.H., Heaman, L.M., and Young, G. 1992. Sampling Laurentia: Detrital Zircon Geochronology Offers Evidence for An Extensive Neoproterozoic River System Originating From the Grenville Orogen. *Geology*, **20**: 351-354.
- Root, K. G. 2001. Devonian Antler fold and thrust belt and foreland basin development in the southern Canadian Cordillera: implications for the Western Canada Sedimentary Basin. *Bulletin of Canadian Petroleum Geology*, **49**(1): 7-36.
- Ross, G.M. 1991. Tectonic setting of the Windermere Supergroup revisited. *Geology*, **19**: 1125-1128.
- Selby, D., Creaser, R. A., and Fowler, M. G. 2007. Re–Os elemental and isotopic systematics in crude oils. *Geochimica et Cosmochimica Acta*, **71**: 378–386.
- Schwarz, D., and Giuliani, G., 2001. Emerald deposits – A review. *Australian Gemologist*, **21**: 17-23.
- Smith, M. T., Dickinson, W. R., and Gehrels, G. E. 1993. Contractional nature of Devonian-Mississippian Antler tectonism along the North American continental margin. *Geology*, **21**: 21-24.
- Taylor, R. P., Fallick, A. E., and Breaks, F. W. 1992. Volatile evolution in Archaean rare-element granitic pegmatites: Evidence from hydrogen isotopic composition of channel H₂O in beryl. *Canadian Mineralogist*, **30**: 877-893.
- Xue, G. M., Zhang, S, Ullrich, T D, Bishop, T, Groat, L A, Thorkelson, D J, Giuliani, G., and Fallick, A. E. 2010. Conditions for Early Cretaceous emerald formation at Dyakou, China; fluid inclusion, Ar-Ar, and stable isotope studies. *Economic Geology*, **105**(2): 339-349.
- Yorath, C. J. 1991. Chapter 9: Upper Jurassic to Paleogene assemblages. In *Geology of the Cordilleran Orogen in Canada*. Edited by H. Gabrielse and C. J. Yorath. Geological Survey of Canada, *Geology of Canada*, no. 4, p. 329-371.
- Zheng, Y.-F. 1999. Oxygen isotope fractionation in carbonate and sulfate minerals. *Geochemical Journal*, **33**: 109-126.

4.9. Appendix: Analytical Procedures

Fluid inclusion petrography was carried out on emerald and quartz chips taken from emerald-bearing veins. Microthermometric measurements were made using a Linkam THMSG 600 heating and freezing stage, calibrated at -56.6°C, 0°C, and 374.1°C using synthetic fluid inclusion standards. Reported temperature measurements have a precision of $\pm 0.2^\circ\text{C}$ below 30°C, and 1.0°C at higher temperatures. Raman spectra of

the vapour phase of two inclusions in emerald were collected on a laser-excited Dilor LabRam Raman spectrometer using the 514.2 nm radiation of an Ar ion laser. The presence of CO₂, N₂, H₂S, and CH₄ in two-phase inclusions in emerald was checked referencing the lines 1388, 2325, 2612, and 2910 cm⁻¹, respectively.

Mineral separates of coeval emerald (n = 5), quartz (n = 5), and dolomite (n = 4) were hand-picked and analysed for hydrogen, oxygen, and carbon isotopes. Samples were chosen from emerald-bearing veins in order to identify a possible fluid source and to determine the temperature of mineralization. Dodecahedral pyrite grains from emerald-bearing quartz and carbonate veins were hand-picked and analysed for sulphur isotopes in order to determine a possible source of sulphur and the method of sulphate reduction. Analyses were conducted at the Facility for Isotope Research at Queen's University in Kingston, Ontario. Errors are better than 5.0‰ for δD, 0.2‰ for δ¹⁸O, 0.2‰ for δ¹³C, and 0.3‰ for δ³⁴S.

The quartz-beryl mineral pair equilibrium calculation of Xue et al. (2010) gives temperatures of 379°C, 405°C, and 405°C for three mineral pairs according to the equation:

$$1000\ln\alpha = 1.153 \cdot \left(\frac{10^6}{T^2}\right) - 0.81$$

The quartz-dolomite mineral pair equilibrium calculation of Zheng (1999) gave a temperature of 383°C according to the equation:

$$1000\ln\alpha = 0.420 \cdot \left(\frac{10^6}{T^2}\right) - 0.12 \cdot \left(\frac{10^3}{T}\right) + 0.01$$

The beryl-dolomite mineral pair equilibrium calculation of Zheng (1999) gave a temperature of 415°C by combining the equations of Xue et al. (2010) and Zheng (1999).

For Re-Os geochronology a sample of quartz-carbonate-emerald vein material bearing dodecahedral pyrite was wrapped in cloth, broken with a hammer, crushed in a

ceramic mortar, and sieved to 0.2 mm. Clean pyrite grains were then picked by hand using stainless steel tweezers. The pyrite recovered from the original sample was divided into 6 separate fractions. Procedures for sulphide digestion, Re and Os separation and purification, mass spectrometry and error propagation are identical to that described by Morelli et al. (2010). Data were regressed with Isoplot 3 (Ludwig 2003) using a decay constant of $1.666 \times 10^{-11} \text{a}^{-1}$ (Smoliar et al. 1996).

Appendix: References

- Ludwig, K. 2003. Isoplot/Ex, version 3.00: A geochronological toolkit for Microsoft Excel: Berkeley Geochronology Center Special Publication No. 4. Berkeley, California.
- Morelli, R. M., Bell, C. C., Creaser, R. A., and Simonetti, A. 2010. Constraints on the genesis of gold mineralization at the Homestake Gold Deposit, Black Hills, South Dakota, from rhenium-osmium sulfide geochronology. *Mineralium Deposita*, **45**, 461-480.
- Smoliar M. I., Walker R. J., and Morgan J. W. 1996. Re-Os ages of group IIA, IIIA, IVA, and IVB iron meteorites. *Science*, **271**: 1099–1102.
- Xue, G. M., Zhang, S, Ullrich, T D, Bishop, T, Groat, L A, Thorkelson, D J, Giuliani, G., and Fallick, A. E. 2010. Conditions for Early Cretaceous emerald formation at Dyakou, China; fluid inclusion, Ar-Ar, and stable isotope studies. *Economic Geology*, **105**(2): 339-349.
- Zheng, Y.-F. 1999. Oxygen isotope fractionation in carbonate and sulfate minerals. *Geochemical Journal*, **33**: 109-126.

5. Deposit type and conclusions

The MRB occurrence is unique in the world as it occurs in Neoproterozoic organic-poor siltstones and sandstones affected by weak to moderate carbonate alteration. No evidence of granitic or significant metamorphic fluids influencing beryl mineralization has been documented at the occurrence, unlike for most of the world's emerald occurrences (Schwarz and Giuliani 2001; Turner and Groat 2007). Two phases of beryl crystallization observed in CL imaging and EMPA indicate that early beryl crystallized from a high-Al, low trace element content fluid that produced highly luminescent crystals, while the second phase of crystallization produced rims that show a trend towards lower Al content from core to rim. This pattern indicates a decrease in Al solubility over time as fluid pH was buffered by host rocks. CL activation by Al may also be distinct to beryl from the MRB, as this feature has never been reported from beryl before. Microprobe analyses also show that beryl is distinctly enriched in Sc and V relative to other emerald deposit types and utilizing EMPA data on a Sc_2O_3 - V_2O_3 - Cr_2O_3 ternary diagram (Fig. 3-8c) the Mountain River emerald data plot separately from other emerald occurrences in a distinct array on the Cr-poor, Sc-rich side of the diagram. Stable isotope equilibration temperatures from cogenetic quartz and beryl from the MRB indicate mineralization occurred on the order of 380 to 415°C at pressures of 2.4 to 4.0 kbar. These temperatures and pressures correspond to depths of 9 to 15 km. Mineralization at the MRB was largely controlled by circulating hydrothermal brines channeled along deep basement structures that may have formed by extension and normal faulting during the Proterozoic. These brines were derived from and interacted with the thick package of sedimentary rocks and evaporite beds of the Neoproterozoic Mackenzie Mountains and Windermere supergroups. The age of mineralization suggests these fluids were likely related to or directly involved in the mineralization of local carbonate-hosted Zn-Pb deposits of the Mackenzie Mountains Zn district (Nelson et al. 2002; Dewing et al. 2006) in the Early Mississippian. Fluid inclusion analyses demonstrate similar fluid salinities and homogenization temperatures from quartz and

beryl from the MRB occurrence (this study) and quartz, calcite, and sphalerite from the nearby Bear-Twit carbonate-hosted Zn-Pb deposit (Gleeson 2006). H₂O-NaCl-CO₂-N₂ dominant mineralizing fluids at the MRB in vein quartz and beryl differ from those observed at carbonate-hosted Zn-Pb deposits of the Mackenzie Platform (Carrière and Sangster 1999) in that they lack hydrocarbons and CH₄. The apparent lack of hydrocarbon- and CH₄-bearing fluids at the MRB reflects the organic-poor nature of the host and underlying strata of the Windermere and Mackenzie Mountains supergroups from which the mineralizing fluids, Be, and transition metals were likely sourced. It also indicates that the driver for reduction of the sulphate-bearing mineralizing fluids was not organic matter, but rather an inorganic reductant such as ferrous iron.

The occurrence of the MRB in sub-greenschist grade sedimentary rocks and its mineralization model related to the circulation of hydrothermal carbonic brines along a fault structure at depth is most similar to the Type 3 emerald deposit model of the Eastern Cordillera of Colombia (Cheillett and Giuliani 1996). These deposits occur in two parallel zones: the eastern zone, consisting of the mining districts of Chivor, Macanal, and Gachalà, and the western zone, consisting of the mining districts of Coscuez, Muzo, Yacopi, and Peñas Blancas. These deposits are hosted in sub-greenschist grade Early Cretaceous black shales of the Llanos and Magdalena basins which were deformed and inverted in the Cenozoic. Colombian emerald mineralization is contained in miarolitic cavities, veins, and hydrothermal breccia in metasomatized black shales affected by albite, calcite, and pyrite alteration (Giuliani et al. 1990). The Eocene and Early Oligocene ages of the deposits for the eastern and western zones, respectively (Cheillett et al. 1994), indicate that emeralds are synorogenic and formed during compression and thrusting of the Eastern Cordillera. This tectonic activity drove deep basal hydrothermal brines along thrust faults and breccia where the injected fluids interacted with the thick sedimentary pile and evaporitic beds (Giuliani et al. 1995). Multistage brecciation and episodic hydraulic fracturing resulted in vein formation and emerald mineralization (Branquet et al. 1999). The mineralizing fluids are H₂O-NaCl-KCl-CaCl₂-CO₂-N₂-SO₄ brines (Cheillett et al. 1994), and mineralization occurred at temperatures of 290 to 360°C and pressures of 1.06 to 1.12 kbar (Cheillett et al. 1994; Giuliani et al. 1995). Many authors have attributed the geologically unique emerald deposits to the process of organic thermochemical sulphate reduction (TSR) wherein

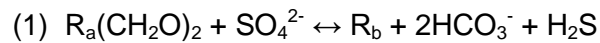
reduction of marine sedimentary evaporitic sulphate by organic matter drove the precipitation of pyrite, carbonate, and emerald (Ottaway et al. 1994; Cheilletz and Giuliani 1996).

5.1. Similarities with Type 3 Colombian systems

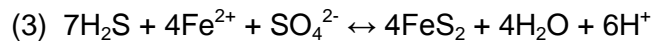
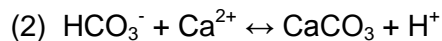
The MRB shares many geological and geochemical similarities with the emerald deposits of Colombia. Both occur in sub-greenschist grade sedimentary host rocks and formed at relatively low to moderate temperatures. Saline carbonic-nitrogenous brines derived from sedimentary sulphate units leached Be, V, Sc, Cr, and other metals from the host sedimentary successions as the fluids circulated along fault structures at depth. The brines involved in mineralization were generally dominated by the system H₂O-NaCl-CO₂-N₂. In addition, KCl, CaCl₂, and sulphate salts have also been identified as important in the mineralizing fluids of the Colombian emerald deposits. However, due to the lower salinities of fluid inclusions from quartz and beryl from the MRB, daughter crystals are not present and therefore the abundances of these salts at the MRB occurrence have not been verified. Emerald mineralization was initiated when high fluid pressures in the fault caused the failure of overlying siliciclastics by hydraulic fracturing which allowed for the formation of extensional veins in the hangingwall (Giuliani et al. 1990; Giuliani et al. 2012). Evaporitic sulphate in the fluids was then exposed to the hangingwall rocks and thermochemically reduced, producing pyrite and iron carbonate. In both deposits, emerald and beryl were byproducts of sulphate reduction during hydraulic fracturing in the hangingwall, however, with important differences in the processes of sulphate reduction and mechanism of tectonic activity driving fault and fluid movement.

5.2. Differences from Type 3 Colombian systems

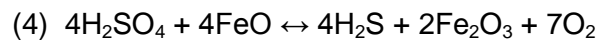
The lithologies and bulk chemistries of host rocks to the MRB and Colombian emerald deposits appear to have the greatest control on the mineralogical expressions of these emerald occurrences. The black shales hosting the Colombian emerald deposits are rich in organic matter. This organic matter was oxidized in the process of TSR by the reaction



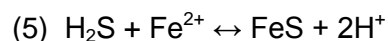
where R_a and R_b represent long-chain hydrocarbons. This reaction led to the byproduct reactions



(Cheilletz and Giuliani 1996). However, the siliciclastic host rocks to beryl-bearing veins at the MRB are devoid of organic material, and no evidence of CH_4 or any other product of the oxidation of organic matter has been observed in thin section or in fluid inclusions. Another means of sulphate reduction must be considered in order to accommodate this lack of organic matter (Fig. 5-1). Warm sulphate-bearing brines involved in emerald mineralization at MRB may have been sourced from deeply buried gypsumiferous units of the Little Dal Group or the Coates Lake Group and were driven up extensional or transfer faults via halokinetic ascent (Giuliani et al. 1995) during Mississippian tectonic activity. Inorganic sulphate reduction is possible by conversion of H_2SO_4 to H_2S or HS^- in warm, oxygen-poor fluids in the presence of abundant iron (in this case, the iron formation beds of the Rapitan Group) according to the equation



H_2S may then react with iron oxides in sediments to form pyrite or may react with metal-rich (or ferrous), oxygen-poor fluid to form base metal sulphides (Ohmoto and Goldhaber 1997)



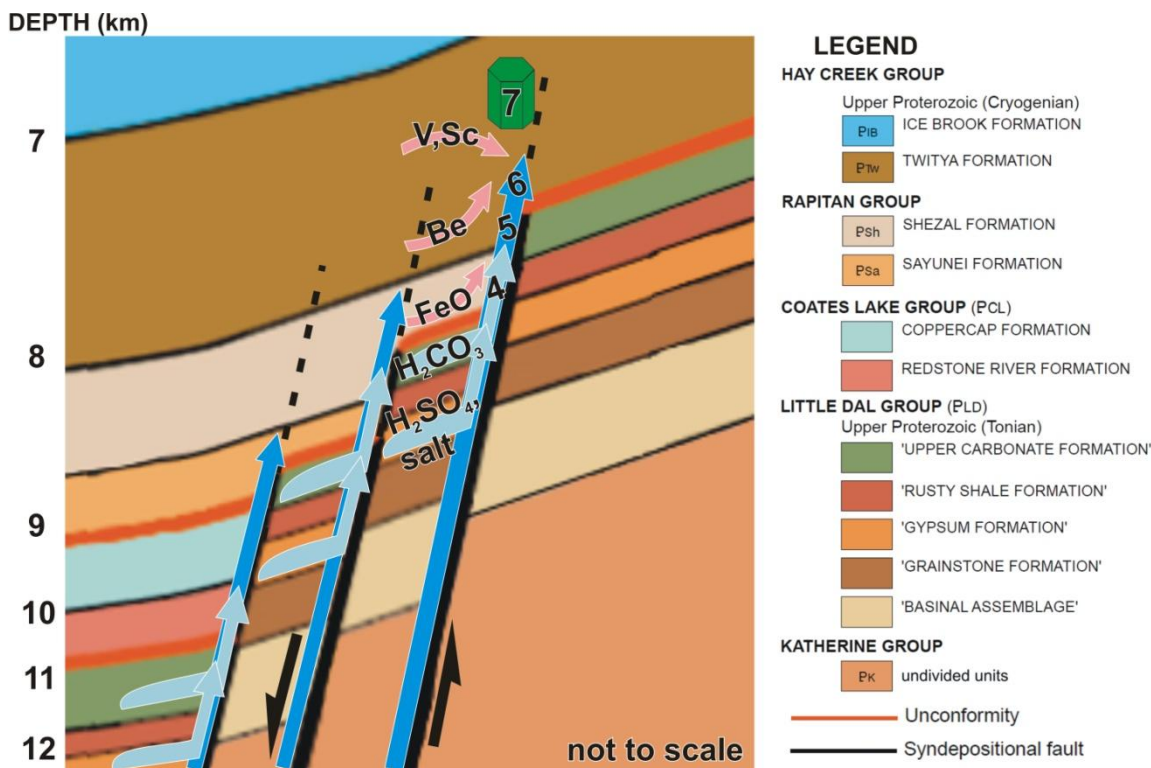
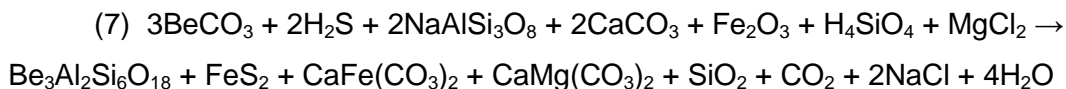


Figure 5-1. Schematic representation of emerald mineralization at MRB. H_2SO_4 -bearing brines were sourced from gypsumiferous beds of the Little Dal or Coates Lake groups and ascended along extensional or transfer faults. H_2CO_3 was sourced from carbonate units of the Little Dal or Coates Lake groups. Numbers correspond to chemical reactions discussed in the text. Be, V, and Sc (and other metals) were leached from host rocks.

These reactions consume H^+ , causing pH to rise, as was interpreted from observations of Al zonation in beryl (Chapter 3). Beryllium was likely leached from host sedimentary rocks, where it may have resided in feldspars, clays, and micas (Ryan 2002), by dissolved bicarbonate, which can increase the solubility of Be and its fractionation into hydrothermal fluids at higher temperatures and circum-neutral pH (Wood 1992). Alternatively, the beryllium may have been leached from host sedimentary rocks by Cl^- , which is more effective at increasing Be solubility at pH less than 4 than bicarbonate (Wood 1992; Ryan 2002). The trace amounts of pyrite at the MRB occurrence also are consistent with lower S fugacity than involved in Colombian emerald mineralization. The lower S fugacity of mineralizing fluids meant that pyrite crystallization

could not soak up Fe from the fluids. Excess Fe²⁺ was then incorporated into ankerite and beryl, which may be the cause of the milkiness (Giuliani et al. 2012) of the emerald crystals from MRB.

It is proposed here that beryl and vein mineralization at MRB proceeded in a fluid dominated system according to the composite reaction



This reaction produces beryl, pyrite, ankerite, dolomite, and quartz, present in veins at MRB, and CO₂, NaCl, and H₂O which are the dominant phases in fluid inclusions.

The alteration and vein mineralogy at the MRB and the Colombian emerald deposits are also dramatically different and likely result from differences in S fugacity and reduction mechanism. In the emerald deposits of Colombia, albitites (metasomatized black shale horizons) are the product of fluid flow alteration marked by epigenetic growth of albite, calcite, dolomite, pyrite, mica, quartz, fluorite, and parasite (Ca(Ce,La)₂(CO₃)₃F₂), and are associated with emerald mineralization. Stratiform hydrothermal breccias (cenicero zones) are polygenetic breccias composed of fragmented shale and albitite, cemented by pyrite, albite, and crushed shale, and were likely the conduits for mineralizing fluids to flow (Cheilletz and Giuliani 1996). At the MRB, evidence of such intense alteration is absent and host rock alteration is restricted to pervasive low- to moderate-intensity carbonate alteration dominated by rhombic and interstitial dolomite (Chapter 2). MRB vein mineralogy is much simpler as well, consisting largely of beryl, quartz, carbonate, and pyrite. Albite is rarely observed in beryl-bearing veins and is likely the stable aluminous phase when insufficient Be is present to form beryl.

Age determinations of mineralization at the Colombian deposits and at MRB also indicate differences in tectonic environments of mineralization, as discussed in Chapter 4 (Fig. 4-11, Fig. 5-2). Whereas the Colombian emerald deposits formed from fluids flushed through the sedimentary pile by compression and transpression along thrust

faults, the fluids involved in mineralization at MRB were driven by complex hydraulics in an extensional and locally transtensional back-arc basin.

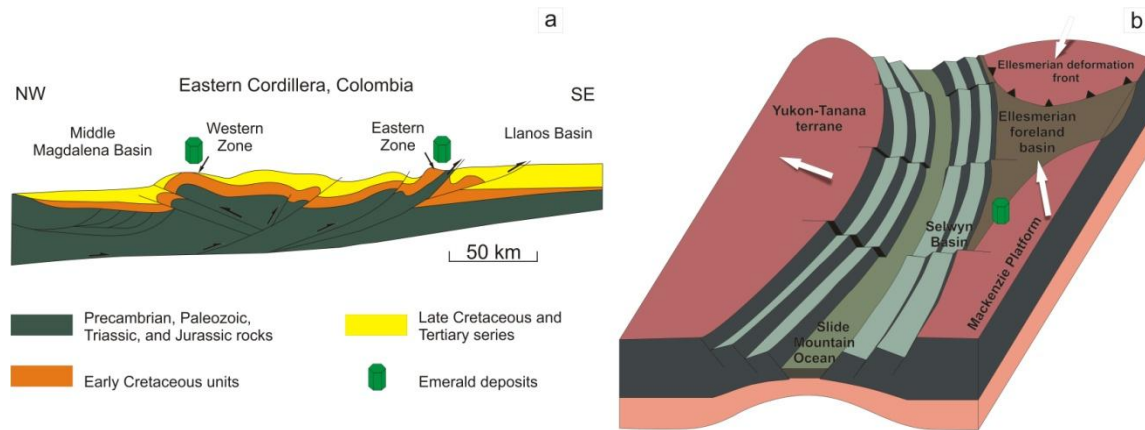


Figure 5-2. *Tectonic environments of emerald mineralization in (a) Colombia (ca. 38-31.5 Ma) and (b) MRB (ca. 345 Ma). Figure (a) is modified from Branquet et al. (1999). Figure (b) is modified after Nelson et al. (2006), Lund (2008), Colpron and Nelson (2009), and Lemieux et al. (2011). White arrows indicate plate motion vectors.*

5.3. Summary

It is important to understand how the MRB is similar to and different from the typical Colombian deposit model. The emerald deposits of Colombia were formed in large, compressed and inverted basins which resulted in the formation of several emerald mining districts. Similar to the MVT-like carbonate-hosted Mackenzie Mountains Zn-Pb district, the Colombian emerald mineralization model does not form individual, discrete deposits, but rather districts of numerous small deposits. The MRB may very well be a single occurrence in a district of other Colombian-like emerald occurrences in the Mackenzie Mountains. The finding that emerald mineralization is possible by inorganic sulphate reduction in sedimentary rocks may also be relevant for global emerald exploration in other sedimentary basins.

References

- Branquet, Y., Laumonier, B., Cheilletz, A., and Giuliani, G. 1999. Emeralds in the Eastern Cordillera of Colombia: Two tectonic settings for one mineralization. *Geology*, **27** (7): 597-600.
- Carrière, J.J., and Sangster, D.F. 1999. Multidisciplinary study of carbonate-hosted zinc-lead mineralization in the Mackenzie Platform (a.k.a. Blackwater and Lac de Bois platforms), Yukon and Northwest Territories, Canada. Geological Survey of Canada, Open File 3700, 145 p.
- Cheilletz, A., Féraud, G., Giuliani, G., and Rodriguez, C. T. 1994. Time-pressure and temperature constraints on the formation of Colombian emeralds: An $^{40}\text{Ar}/^{39}\text{Ar}$ laser microprobe and fluid inclusion study. *Economic Geology*, **89**: 361-380.
- Cheilletz, A., and Giuliani, G. 1996. The genesis of Colombian emeralds: A restatement. *Mineralium Deposita*, **31**: 359-364.
- Colpron, M., and Nelson, J.L. 2009. A Palaeozoic Northwest Passage: incursion of Caledonian, Baltican and Siberian terranes into eastern Panthalassa, and the early evolution of the North American Cordillera. Geological Society, London, Special Publications 2009, v. 318, p. 273-307.
- Dewing, K., Sharp, R.J., Ootes, L., Turner, E.C., and Gleeson, S. 2006. Geological assessment of known Zn-Pb showings, Mackenzie Mountains, Northwest Territories. Geological Survey of Canada, Current Research 2006-A4, 12 p.
- Giuliani, G., Cheilletz, A., Arboleda, C., Carrillo, V., Rueda, F., and Baker, J. H. 1995. An evaporitic origin of the parent brines of Colombian emeralds: fluid inclusion and sulphur isotope evidence. *European Journal of Mineralogy*, **7**: 151-165.
- Giuliani, G., Ohnenstetter, D., Fallick, A.E., Groat, L.A., and Feneyrol, J. 2012. Geographic origin of gems linked to their geological history. *InColor*, **19**: 16-27.
- Giuliani, G., Rodriguez, R.T., and Rueda, F. 1990. Les gisements d'émeraude de la Cordillère Orientale de la Colombie: Nouvelles données métallogéniques. *Mineralium Deposita*, **25**: 105-111.
- Gleeson, S. 2006. A microthermometric study of fluid inclusions in sulphides and carbonates from Gayna River and the Bear-Twit base metal prospects, Mackenzie Mountains, NWT. Northwest Territories Geoscience Office, NWT Open Report 2006-005, 9 p.
- Lemieux, Y., Hadlari, T., and Simonetti, A. 2011. Detrital zircon geochronology and provenance of Devonian-Mississippian strata in the northern Canadian Cordilleran miogeocline. *Canadian Journal of Earth Sciences*, **48**: 515-541.
- Lund, K. 2008. Geometry of the Neoproterozoic and Paleozoic rift margin of western Laurentia: Implications for mineral deposit settings. *Geosphere*, **4**(2): 429-444.

- Nelson, J., Paradis, S., Christensen, J., and Gabites, J. 2002. Canadian Cordilleran Mississippi Valley-Type deposits: A case for Devonian-Mississippian back-arc hydrothermal origin. *Economic Geology*, **97**: 1013-1036.
- Nelson, J.L., Colpron, M., Piercey, S.J., Dusel-Bacon, C., Murphy, D.C., and Roots, C.F. 2006. Paleozoic tectonic and metallogenic evolution of the pericratonic terranes in Yukon, northern British Columbia and eastern Alaska. *In* Paleozoic Evolution and Metallogeny of Pericratonic Terranes at the Ancient Pacific Margin of North America, Canadian and Alaskan Cordillera. *Edited by* M. Colpron and J. L. Nelson. Geological Association of Canada, Special Paper 45, p. 323-360.
- Ohmoto, H., and Goldhaber, M.B. 1997. Sulfur and Carbon Isotopes. *In* Geochemistry of Hydrothermal Ore Deposits (3rd edition). *Edited by* H.L. Barnes. John Wiley & Sons, Inc., New York, pp. 517-611.
- Ottaway, T. L., Wicks, F. J., Bryndzia, L. T., Kyser, T. K., and Spooner, E. T. C. 1994. Formation of the Muzo hydrothermal emerald deposit in Colombia. *Nature*, **369**(6481): 552-554.
- Ryan, J. G. 2002. Trace-element Systematics of Beryllium in Terrestrial Materials. *In* Beryllium: Mineralogy, Petrology, and Geochemistry. *Edited by* E.S. Grew. *Reviews in Mineral Geochemistry*, **50**: 121-145.
- Schwarz, D., and Giuliani, G. 2001. Emerald deposits – A review. *Australian Gemologist*, **21**: 17-23.
- Turner, D., and Groat, L.A. 2007. Chapter 4: Non-emerald gem beryl. *In* Geology of Gem Deposits, Short Course 37, *Edited by* L.A. Groat. Mineralogical Association of Canada, Yellowknife, Northwest Territories, p. 79-109.
- Wood, S.A. 1992. Theoretical prediction of speciation and solubility of beryllium in hydrothermal solution to 300°C at saturated vapor pressure: Application to bertrandite/phenakite deposits. *Ore Geology Reviews*, **7**: 249-278.

Appendices

Appendix A: Sample locations.

Table A-1. Listed locations, descriptions, samples, and measured structures from field stations.

Station	UTM E	UTM N	Unit	Station Description	Sample Number	Sample Description	Structure	Measurement
10MH01	477204	7141163	Twitya Fm	extensive quartz-carbonate veining (mm to 5 cm thick) with pyrite and beryl in medium grey, massive bedded dolomitic sandstone host rock (weathers buff to brown)	10MH01A 10MH01B	beryl-pyrite in quartz vein vuggy beryl and quartz in carbonate vein with host dolomitic sandstone	extensional quartz veins	075 60°
10MH02	477369	7141149	Icebrook Fm	medium- to thick-bedded dolomite, weathers buff to brown; fractures filled by calcite	10MH02A	host rock with thin carbonate veining	bedding	145 56°
10MH03	477321	7141074	Twitya Fm	thinly bedded (1-2mm) brown siltstone interbedded with green-grey-brown siltstone ; weathers to orange and rusty brown; first sign of beryl in extensive quartz-carbonate veins	10MH03A	host rock with carbonate-beryl veining, 2.5 cm thick, plus minor pyrite	vein	280 45°

Table A-1. Continued.

10MH04	477255	7141061	Twitya Fm	thinly bedded sideritic sandstone with minor quartz-carbonate veins (6-10 mm), minor pyrite	10MH04A	bedded sideritic sandstone	bedding	090 75°
10MH05	477286	7141002	Twitya Fm	finely laminated to thinly bedded calcareous siltstone, iron staining; minor carbonate-quartz veins with pyrite				
10MH06	477198	7141058	Twitya Fm	finely bedded buff-coloured siltstone with interbedded laminae of reddish brown silty mud; cut by abundant quartz-carbonate veins that weather brown			fold hinge	120 15°
10MH07	477247	7141093	Twitya Fm	massive pyritic quartzite with ubiquitous quartz-carbonate veins (5-7 mm diameter) with minor beryl	10MH07A	host sandstone with carbonate-beryl veining	carbonate-quartz vein	110 80°
10MH08	477163	7141051	Twitya Fm	thick shaley sandstone beds few mm to up to 15 cm thick; 2 cm wide barren carbonate veins			bedding	296 45°

Table A-1. Continued.

10MH09	477240	7141113	Twitya Fm	massive pinkish-grey sandstone cut by quartz-beryl veins	10MH09A 10MH09B	host sandstone with quartz-carbonate-beryl veining, minor pyrite taken from float; host sandstone with quartz-carbonate-beryl veins, minor chalcopyrite	quartz-carbonate-beryl vein	250 40°
10MH10	477291	7141157	Icebrook Fm	massive bedded grey dolostone with shaly interbeds; dolostone beds up to 30 cm, shaly beds are several mm thick			bedding	310 85°
10MH11	477252	7141139	Twitya Fm	coarse pink-grey sandstone containing large grey sandstone clasts; carbonate-quartz beryl veins up to 7cm thick, where beryl is locally highly concentrated	10MH11A	host sandstone, carbonate-quartz-beryl veins	quartz-carbonate-beryl vein	250 71°
10MH12	477236	7141177	Icebrook Fm	large outcrop of grey dolostone weathering to buff with multiple thin quartz-carbonate-beryl veins which trend parallel to reverse fault	10MH12A	host dolostone with quartz-carbonate-beryl vein	reverse fault	250 55°

Table A-1. Continued.

10MH13	477215	7141191	Icebrook Fm	massive white-grey dolostone; large scale fault contact			reverse fault	270 32°
10MH14	477191	7141202	Icebrook Franklin Mountain Fm?	or massive white-grey dolostone -looks like fault contact to west and north				
10MH15	477211	7141135	Twitya Fm	host sandstone riddled with quartz-carbonate veins with minor beryl in vein; carbonate is a deep reddish-brown colour	10MH15A	host sandstone with radiating beryl in quartz-carbonate vein	carbonate vein	263 63°
10MH16	477204	7141113	Twitya Fm	rusty pyritic sandstone with minor interbedded mudstone			bedding	135 40°
10MH17	477218	7141116	Twitya Fm	fine- to medium-grained pinkish-grey pyritic sandstone cut by carbonate-quartz-beryl veins up to 0.5 cm thick; sandstone brecciated by 3 cm thick carbonate vein, then cut by 5 mm thick quartz vein, again cut by 1 cm thick quartz-carbonate-beryl vein	10MH17A	host sandstone, quartz-carbonate-beryl(-pyrite) vein	vein	270 50°
					10MH17B	host sandstone, carbonate vein		

Table A-1. Continued.

10MH18	477198	7141139	Twitya Fm	thinly bedded fine- to medium-grained sandstone weathering rusty brown with minor pyrite; cut by fractures filled with ubiquitous thin green mica (possibly fuchsite) veins and thicker carbonate veins	10MH18A	host sandstone with thin green mica veinlet	fracture with mica vein	080 15°
10MH19	477149	7141150	Twitya Fm	very fine-grained shaly siltstone, greenish brown on unweathered surfaces, weathering to greyish-brown and reddish-brown beds; outcrop cut by quartz-carbonate-beryl veins; one vein about 1 cm wide of blue beryl (aquamarine), in addition to several quartz-carbonate veins containing unidentified purple and blue minerals	10MH19A	siltstone, quartz-carbonate vein		
					10MH19B	purple and blue unidentified mineral vein cut by quartz-carbonate vein		
					10MH19C	aquamarine taken from vein	fold hinge	136 10°
					10MH19D	quartz-carbonate-beryl vein		
10MH20	477173	7141171	Twitya Fm	reddish brown siltstone with thin laminations of darker red-brown mudstone; ubiquitous red carbonate-quartz veining and lesser thin green mica veinlets				

Table A-1. Continued.

10MH21	477162	7141197	Icebrook Fm	folded and heavily faulted tan to grey dolostone with thin dolomite laminae (algal layers?); minor beryl veins where beryl is heavily fractured and smeared in fault plane; light green amorphous stain on weathered surface of dolostone may be Cu		fold axis	350 22°
10MH22	476509	7123475	Marmot Fm (Mountain diatreme)	diatreme pipe on hillside in valley; soft, very fine-grained green-grey matrix with large (1 to 9 mm) phenocrysts of phlogopite, pyrite and carbonate (possibly also ilmenite), as well as limestone and chert xenoliths; matrix contains minor carbonate	10MH22A	soft, very fine-grained green-grey matrix with phenocrysts of phlogopite, pyrite and carbonate (possibly also ilmenite), as well as limestone and chert xenoliths; matrix weathers orange	
10MH23	478076	7133731	Twitya Fm	rubble near Golden diatreme dyke within Twitya Fm	10MH23A	quartz-carbonate vein from float	
					10MH23B	soft, very fine grained dark grey-green matrix with phlogopite and pyrite phenocrysts	

Table A-1. Continued.

10MH24	478059	7133717	Marmot Fm (Golden dyke)	near Golden diatreme dyke within Twitya Fm	10MH24A	soft, very fine grained dark grey-green matrix with phlogopite and pyrite phenocrysts		
					10MH24B	quartz-carbonate- galena veins		
10MH25	477965	7133724	Twitya Fm	diamicite float found in creek	10MH25B	found in float; semi- massive galena in quartz vein		
10MH26	477944	7133594	Twitya Fm	Golden diatreme dyke about 1m wide cutting Twitya Fm at 160°	10MH26A	phlogopite phenocrysts within soft, very fine-grained dark grey matrix	dyke	160 89°
10MH27	477862	7133670	Twitya Fm	diatreme boulders and quartz boulders with malachite	10MH27A	rusty vuggy quartz vein with abundant Cu staining		
10MH28	488890	7150674	Little Dal Gp (Gypsum Fm)	gypsum beds in Little Dal Gp, right on red bed; massive white gypsum containing limestone and sandstone clasts	10MH28A	white-grey beds of soft, massive gypsum with grey laminae		

Table A-1. Continued.

10MH29	465888	7168354	Little Dal Gp (Gypsum Fm)	gypsum in Little Dal Gp; massive bedded white to pale grey gypsum with green and pink staining in some places; interbedded with coherent clasts of limestone and red mudstone	10MH29A	white-grey beds of soft, massive gypsum with grey laminae		
					10MH29B	gypsum vein cutting limestone beds		
10MH30	477097	7141141	Twitya Fm	finely bedded pinkish-brown sandstone with minor quartz-carb veins which weather to orange-red; outcrop is heavily fractured	10MH30A	bedded sandstone		
					10MH30B	sandstone	bedding	352 61°
10MH31	477023	7141104	Twitya Fm	finely bedded pinkish-brown sandstone with extensive quartz-carbonate veins with minor pyrite and trace chalcopyrite; abundant green mica within most fractures	10MH31A	sandstone with green mica veinlet	normal fault	160 85°
10MH32	476668	7140992	Twitya Fm	coarse pinkish white sandstone with rounded clasts; about 20% clasts, pebble to cobble size; cut by extensive quartz-carbonate veins which weather to red-orange			quartz-carbonate vein	295 80°, 060 42°

Table A-1. Continued.

10MH33	476695	7141866	Twitya Fm	diatreme boulders in creek bed; soft, very fine-grained green-grey matrix with biotite phenocrysts		
10MH34	476702	7141086	Twitya Fm	sandy conglomerate above very fine-grained dark grey pyritic silty mudstone, separated by fault gouge in which conglomerate was thrust up		reverse fault 340 65°
10MH35	476758	7141202	Twitya Fm	diatreme boulder 1.5 x 1 m diameter in creek bed	10MH35A	soft, fine-grained grey matrix with biotite phenocrysts and limestone xenoliths
10MH36	476798	7141229	Ice Brook or Franklin Mountain Fm?	dark grey breccia with angular clasts of limestone and sandstone up to fist size	10MH36A	breccia with angular clasts of limestone and sandstone
10MH37	468027	7143106	Marmot Fm (Dino dyke)	small diatreme dyke - not much outcrop, but boulders present	10MH37A	diatreme boulder in float, found between Dino diatreme dyke and Clark diatreme pipe

Table A-1. Continued.

10MH38	460142	7140729	Marmot Fm (Clergy dyke)	Clergy dyke/sill cutting across carbonate breccia wall rock, approximately 3 m wide; dyke contains xenoliths of host carbonate (massive and bedded limestone clasts)	10MH38A	fine-grained grey-green matrix with phlogopite and pyrite phenocrysts, with trace chalcopyrite	dyke	094 20°
10MH39	472459	7163926	Coates Lake Gp (Redstone River Fm)	Coates Lake gypsum; white-grey massive gypsum beds, weathering to buff and grey, with some dissolution pockets in outcrop	10MH39A	Coates Lake Group gypsum		
10MH40	476642	7140878	Twitya Fm	poorly sorted massive conglomerate with limestone and sandstone clasts roughly pebble to cobble size; cut by quartz-carbonate veins which weather to red-orange				
10MH41	476774	7141190	Twitya Fm	finely bedded dark grey shaly sandstone				
10MH42	477081	7141453	Franklin Mountain Fm	orange sandstone boulder in stream cut extensively by quartz-carbonate-beryl veins; the highest occurrence of beryl in the stream				

Table A-1. Continued.

10MH43	477199	7141507	Franklin Mountain Fm	thick bedded dark grey limestone cut by calcite veins	10MH43A	diatrema boulder found in creek bed	bedding	115 75°
10MH44	477306	7141657	Franklin Mountain Fm	limestone beds dipping west			bedding	118 32°

Appendix B: Bulk rock geochemistry.

Five samples of Twitya Formation host rock and two samples of evaporite rocks from the Little Dal and Coates Lake groups were submitted for bulk rock geochemical analyses (Table B-1). Quality control data is presented in Table B-2. Samples selected for bulk rock geochemical analyses were chosen based on the absence of veins, significant alteration, and weathering. Samples were cleaned with water and a scrub brush and had any oxidation staining or vein material removed by rock saw. Approximately 50 g of fresh sample was sent to Activation Laboratories Ltd. in Ancaster, Ontario, and analyzed for total carbon and total sulphur, major oxides, and minor and trace elements. Total carbon and sulphur concentrations were obtained by infrared (IR) according to the method of Code 4F-C,S, where the sample was combusted in the presence of an accelerator and oxygen to produce CO, CO₂, and SO₂. Carbon is measured as CO₂ in the IR cell. An Eltra CS-2000 was used for the analysis. Major oxide and some minor and trace element concentrations were obtained by fusion inductively-coupled plasma mass spectrometry (FUS-ICP) according to the method of Code 4E-Research. Samples were mixed with a mixture of lithium metaborate and lithium tetraborate and fused in a graphite crucible. The molten mixture was poured into a 5% nitric acid solution and shaken until dissolved (30 minutes). The samples were run for major oxides and selected traces on a combination simultaneous/sequential Thermo Jarrell-Ash Enviro II ICP-MS. A variety of international reference materials and independent control standards were used for calibration. Certain minor and trace element concentrations were obtained by instrumental neutron activation analysis (INAA) according to the method of Code 4E-Research, in which a 1 g aliquot of sample was encapsulated in a polyethylene vial and irradiated with flux wires at a thermal neutron flux of $7 \times 10^{12} \text{ n cm}^{-2} \text{ s}^{-1}$. After a seven day period, the samples were counted on a high purity Ge detector with resolution of better than 1.7 KeV for the 1332 KeV Co-60 photopeak. Using the flux wires, the decay-corrected activities were compared to a calibration developed from multiple certified international reference materials. One standard and one blank were analyzed. Some minor and trace elements were analysed by total digestion ICP-MS (TD-ICP-MS) according to the method of Code 4E-Research. The samples were digested with four acids beginning with hydrofluoric, followed by a

mixture of nitric and perchloric acids, and heated to dry the samples. The samples were brought back into solution using hydrochloric acid. Samples are analyzed using a Varian Vista ICP-MS. An internal standard or certified reference material was used for quality control. Lithium concentration was analysed by sodium peroxide fusion ICP-MS (FUS- Na_2O_2) according to the method of Code 8-peroxide fusion ICP-MS. Fused samples were diluted and analyzed by Perkin Elmer Sciex ELAN 6000, 6100 or 9000 ICPMS. One control, one blank, and one standard were fused with samples (<http://www.actlabs.com/page.aspx?page=531&app=226&cat1=549&tp=12&lk=no&menu=64>).

Table B-1. Major, minor, and trace element compositions of whole rock samples.

		C_{Total}	S_{Total}	SiO₂	Al₂O₃	Fe₂O₃	MnO	MgO	CaO	Na₂O	K₂O	TiO₂	P₂O₅	LOI	Total
		%	%	%	%	%	%	%	%	%	%	%	%	%	%
Detection Limit		0.01	0.01	0.01	0.01	0.01	0.001	0.01	0.01	0.01	0.01	0.001	0.01		0.01
Analysis Method		IR	IR	FUS-ICP	FUS-ICP	FUS-ICP	FUS-ICP	FUS-ICP	FUS-ICP	FUS-ICP	FUS-ICP	FUS-ICP	FUS-ICP	FUS-ICP	FUS-ICP
Sample	Description														
DM09-04	emerald			61.89	14.93	1.24	0.034	1.78	0.25	1.55	0.13	0.068	<0.01		81.86
Host Rock	Twitya Formation														
10MH04A	planar bedded siltstone	<0.01	<0.01	58.87	18.12	6.35	0.036	1.7	0.64	5.01	3.29	1.051	0.08	4.75	99.89
10MH12A	dolomitized limestone	9.6	0.02	14.65	3.28	4.4	0.095	16.18	23.68	1.95	0.02	0.251	0.1	35.34	99.95
10MH31A	sandstone	2.24	0.18	50.01	17.14	9.02	0.108	3.21	1.9	7	1.94	1.166	0.11	8.77	100.4
10MH09C	sandstone	1.99	0.16	74.4	3.82	3.11	0.078	2.37	4.94	2.24	0.03	1.146	0.07	7.37	99.58
09HS-MRB	sandstone			20.3	5.69	3.45	0.076	13.45	20.47	3.28	0.12	0.421	0.09	32.33	99.67
Evaporites	Little Dal Gypsum Fm														
10MH28B	Coates Lake Group	2.68	11	14.96	1.15	0.6	0.01	5.02	26.4	0.13	0.36	0.122	0.02	23.15	71.92
10MH39A		11.7	0.03	4.27	0.13	0.13	0.006	22.84	28.6	0.01	0.03	0.005	0.01	43.29	99.31
Continental Crust*				61.6	15.0	6.2	0.09	3.7	5.5	3.2	3.2	0.67	0.17		
Greywacke*				69.1	13.5	5.9	0.10	2.3	2.6	3.0	2.0	0.72	0.13		
Shale*				58.4	15.1	6.7	0.11	2.5	3.1	1.3	2.6	0.77	0.16		

Table B-1. Continued.

		Ag	Au	As	B	Ba	Be	Bi	Br	Cd	Ce	Co	Cr	Cs	Cu
		ppm	ppb	ppm	ppm	ppm	ppm	ppm	ppm	ppm	ppm	ppm	ppm	ppm	ppm
Detection Limit		0.5	1	5	0.5	3	1	0.4	0.5	0.5	0.1	1	20	0.5	10
Analysis Method		INAA/ TD- ICP	INAA	FUS- MS/ INAA	PGNAA	FUS- ICP	FUS- ICP	FUS- MS/ TD- ICP	INAA	TD- ICP	FUS- MS/ INAA	FUS- MS/ INAA	FUS- MS/ INAA	FUS- MS/ INAA	FUS- MS/ TD- ICP
Sample	Description														
DM09-04	emerald	< 0.5		< 5		44	40930	< 0.4			274	13	1430	69.3	470
Host Rock	Twitya Formation														
10MH04A	planar bedded siltstone	< 0.5	< 1	2	69	175	6	2	< 0.5	<0.5	54	25.8	97.9	2.8	4
10MH12A	dolomitized limestone	< 0.5	2	< 1	< 2	4	20	< 2	< 0.5	<0.5	20	2.6	20.2	< 0.2	< 1
10MH31A	sandstone	< 0.5	< 1	15	26	119	5	< 2	< 0.5	<0.5	80	30	117	< 0.2	5
10MH09C	sandstone	< 0.5	< 1	11	2	6	10	< 2	0.9	<0.5	9	15.4	64.7	< 0.2	15
09HS-MRB	sandstone	< 0.5	< 1	< 1		11	14	< 2	< 0.5	<0.5	52	1.9	< 0.5	< 0.2	4
Evaporites															
10MH28B	Little Dal Gypsum Fm	< 0.5	< 1	< 1	50	31	< 1	< 2	1.4	<0.5	9	1.9	6.4	0.6	< 1
10MH39A	Coates Lake Group	< 0.5	< 1	< 1	10	134	< 1	< 2	0.5	<0.5	1	1	< 0.5	< 0.2	< 1
Continental Crust*		0.07	0.003	1.7	11	584	2.4	0.09	1	0.1	60	24	126	3.4	25
Greywacke* Shale*		nd 0.07	0.005 0.003	nd 1.3	37 100	426 580	nd 3	nd 0.4	nd 4	nd 0.3	58 50	15 19	88 90	2.2 5	24 45

Table B-1. Continued.

		Dy	Eu	Er	Ga	Gd	Ge	Hf	Hg	Ho	In	La	Li	Lu	Mo
Detection Limit		ppm 0.1	ppm 0.05	ppm 0.1	ppm 1	ppm 0.1	ppm 1	ppm 0.2	ppm 1	ppm 0.1	ppm 0.2	ppm 0.1	ppm 2	ppm 0.04	ppm 2
Analysis Method		FUS-MS	FUS-MS/ INAA	FUS-MS	FUS-MS	FUS-MS	FUS-MS	FUS-MS/ INAA	INAA	FUS-MS	FUS-MS	FUS-MS/ INAA	FUS- Na ₂ O ₂	FUS-MS/ INAA	FUS-MS/TD- ICP
Sample	Description														
DM09-04	emerald	1	0.19	0.5	19	0.9	< 1	0.3		0.2	< 0.2	7	167	0.05	10
Host Rock	Twitya Formation														
10MH04A	planar bedded siltstone		1.09					5.1	< 1			28.6	<0.01	0.39	< 2
10MH12A	dolomitized limestone		2.85					0.8	< 1			4.69	<0.01	1.56	< 2
10MH31A	sandstone		1.78					4.8	< 1			42.4	<0.01	0.37	< 2
10MH09C	sandstone		1.51					4.5	< 1			2.36	<0.01	0.83	< 2
09HS-MRB	sandstone		5.8					1.3	< 1			25.7		2.97	< 2
Evaporites															
10MH28B	Little Dal Gypsum Fm		0.16					1.4	< 1			4.18	<0.01	0.07	< 2
10MH39A	Coates Lake Group		0.07					< 0.2	< 1			0.61	<0.01	<0.01	< 2
Continental Crust*		3.8	1.3	2.1	15	4	1.4	4.9	0.04	0.8	0.05	30	18	0.35	1.1
Greywacke*		3.4	1.2	2.2	16	4	nd	3.5	nd	0.78	nd	34	nd	0.37	nd
Shale*		4.3	1.1	2.7	19	5.2	1.6	2.8	0.4	1.2	0.1	24	66	0.6	2.6

Table B-1. Continued.

		Nb	Nd	Ni	Pb	Pr	Rb	Sb	Sc	Se	Sm	Sn	Sr	Ta	Tb
		ppm	ppm	ppm	ppm	ppm	ppm	ppm	ppm	ppm	ppm	ppm	ppm	ppm	ppm
Detection Limit		1	0.1	20	5	0.05	2	0.5	1	0.5	0.1	1	2	0.1	0.1
Analysis Method		FUS-MS	FUS-MS/ INAA	FUS-MS/ TD-ICP	FUS-MS/ TD-ICP	FUS-MS	FUS-MS/ INAA	FUS-MS/ INAA	FUS-MS/ INAA	INAA	FUS-MS/ INAA	FUS-MS	FUS-ICP	FUS-MS/ INAA	FUS-MS/ INAA
Sample	Description														
DM09-04	emerald	2	3.1	850	75	1	12	< 0.5	1355		0.5	1	11	0.1	0.2
Host Rock	Twitya Formation														
10MH04A	planar bedded siltstone		23	43	< 5		90	1.2	22.3	< 0.5	5.24		29	1.6	1.1
10MH12A	dolomitized limestone		3	2	< 5		< 10	0.8	125	< 0.5	3.45		373	1.3	4.6
10MH31A	sandstone		30	57	< 5		70	0.8	44.9	< 0.5	7.33		52	2.7	< 0.1
10MH09C	sandstone		< 1	12	< 5		< 10	0.7	26.1	< 0.5	1.95		53	1.6	3.3
09HS-MRB	sandstone		< 1	8	< 5		< 10	2.7	126	< 0.5	7.85		298	1.5	8.5
Evaporites															
10MH28B	Little Dal Gypsum Fm		4	2	< 5		< 10	< 0.1	1.88	< 0.5	0.91		239	1	< 0.1
10MH39A	Coates Lake Group		< 1	< 1	< 5		< 10	< 0.1	0.25	< 0.5	0.12		247	1.4	< 0.1
Continental Crust*			27	56	14.8		78	0.3	16		5.3		333	1.1	0.65
Greywacke*			25	24	14.2		72	nd	16		4.6		201	nd	0.63
Shale*			24	68	20		140	1.5	13		5.8		300	0.8	0.9

Table B-1. Continued.

		Th ppm 0.1	Tl ppm 0.1	Tm ppm 0.05	U ppm 0.1	V ppm 5	W ppm 1	Y ppm 2	Yb ppm 0.1	Zn ppm 30	Zr ppm 4
Detection Limit											
Analysis Method		FUS-MS/ INAA	FUS-MS	FUS-MS	FUS-MS/ INAA	FUS-ICP	FUS-MS/ INAA	FUS-ICP	FUS-MS/ INAA	FUS-MS/ TD-ICP	FUS-ICP
Sample	Description										
DM09-04	emerald	4	0.1	0.07	0.6	2846	2	4	0.4	>10000	10
Host Rock	Twitya Formation										
10MH04A	planar bedded siltstone	13.6			2.9	160	7	28	2.81	6	192
10MH12A	dolomitized limestone	5.3			1.6	271	< 1	178	11.6	21	43
10MH31A	sandstone	12.7			2.4	252	11	26	2.48	19	181
10MH09C	sandstone	5.4			0.8	135	20	127	6.59	7	161
09HS-MRB	sandstone	30.6			< 0.1	240	< 1	372	22.9	15	49
Evaporites											
10MH28B	Little Dal Gypsum Fm	1.4			0.5	6	< 1	4	0.5	5	46
10MH39A	Coates Lake Group	< 0.1			0.3	< 5	< 1	1	0.07	3	5
Continental Crust*		8.5	0.52	0.3	1.7	98	1.0	24	2	65	203
Greywacke*		9	nd	nd	2.0	98	nd	26	2.1	76	302
Shale*		12	1	0.5	3.7	130	1.8	26	2.2	95	160

Note: nd – no data.

* Data from Lentz 2003.

Table B-2. Quality control data for whole rock geochemical standards and blanks.

Analyte Symbol	Total C	Total S	Total S	SiO ₂	Al ₂ O ₃	Fe ₂ O ₃	MnO	MgO	CaO	Na ₂ O	K ₂ O	TiO ₂	P ₂ O ₅
Unit Symbol	%	%	%	%	%	%	%	%	%	%	%	%	%
Detection Limit	0.01	0.01	0.001	0.01	0.01	0.01	0.001	0.01	0.01	0.01	0.01	0.001	0.01
Analysis Method	IR	IR	TD-ICP	FUS-ICP	FUS-ICP	FUS-ICP	FUS-ICP	FUS-ICP	FUS-ICP	FUS-ICP	FUS-ICP	FUS-ICP	FUS-ICP
GXR-1 Meas			0.256										
GXR-1 Cert			0.257										
NIST 694 Meas				11.35	1.9	0.75	0.011	0.37	44.67	0.9	0.56	0.119	30.22
NIST 694 Cert				11.2	1.8	0.79	0.0116	0.33	43.6	0.86	0.51	0.11	30.2
DNC-1 Meas				47.19	18.75	9.59	0.146	10.13	10.93	1.9	0.24	0.483	0.07
DNC-1 Cert				47.15	18.34	9.97	0.15	10.13	11.49	1.89	0.234	0.48	0.07
GBW 07113 Meas				71.56	13	3.18	0.138	0.14	0.55	2.36	5.36	0.28	0.02
GBW 07113 Cert				72.8	13	3.21	0.14	0.16	0.59	2.57	5.43	0.3	0.05
GXR-4 Meas			1.76										
GXR-4 Cert			1.77										
SDC-1 Meas			0.064										
SDC-1 Cert			0.065										
SCO-1 Meas													
SCO-1 Cert													
GXR-6 Meas			0.016										
GXR-6 Cert			0.016										
LKSD-4 Meas	18.5												
LKSD-4 Cert	17.7												
SY-2 Meas													
SY-2 Cert													
SY-3 Meas													
SY-3 Cert													
W-2a Meas				53.2	15.28	10.86	0.17	6.53	10.8	2.2	0.64	1.106	0.12
W-2a Cert				52.4	15.4	10.7	0.163	6.37	10.9	2.14	0.626	1.06	0.13
SY-4 Meas				49.72	20.5	6.27	0.107	0.53	7.88	7.09	1.7	0.29	0.12
SY-4 Cert				49.9	20.69	6.21	0.108	0.54	8.05	7.1	1.66	0.287	0.131

Note: Meas – measured value
Cert – certified value

Table B-2. Continued.

Analyte Symbol	C- Total	Total S	Total S	SiO₂	Al₂O₃	Fe₂O₃	MnO	MgO	CaO	Na₂O	K₂O	TiO₂	P₂O₅
Unit Symbol	%	%	%	%	%	%	%	%	%	%	%	%	%
Detection Limit	0.01	0.01	0.001	0.01	0.01	0.01	0.001	0.01	0.01	0.01	0.01	0.001	0.01
Analysis Method	IR	IR	TD-ICP	FUS- ICP	FUS- ICP	FUS- ICP	FUS- ICP	FUS- ICP	FUS- ICP	FUS- ICP	FUS- ICP	FUS- ICP	FUS- ICP
BIR-1a Meas				47.97	15.88	10.97	0.172	9.6	12.94	1.77	0.02	0.958	< 0.01
BIR-1a Cert				47.96	15.5	11.3	0.175	9.7	13.3	1.82	0.03	0.96	0.021
ZW-C Meas													
ZW-C Cert													
SGR-1b Meas	27	1.55											
SGR-1b Cert	28	1.53											
DNC-1a Meas													
DNC-1a Cert													
OREAS 13b (4-Acid) Meas			1.16										
OREAS 13b (4-Acid) Cert			1.2										
NCS DC86303 Meas													
NCS DC86303 Cert													
NCS DC86304 Meas													
NCS DC86304 Cert													
NCS DC86314 Meas													
NCS DC86314 Cert													
BCR-2 Meas				53.79	13.39	13.43		3.53	6.98	3.01	1.79	2.218	0.35
BCR-2 Cert				54.1	13.5	13.8		3.59	7.12	3.16	1.79	2.26	0.35
Method Blank													
Method Blank			< 0.001										
Method Blank			0.001										
Method Blank													
Method Blank													

Note: Meas – measured value
 Cert – certified value

Table B-2. Continued.

Analyte Symbol	Au	Ag	Ag	As	B	Ba	Be	Bi	Br	Cd	Ce	Co
Unit Symbol	ppb	ppm	ppm	ppm	ppm	ppm	ppm	ppm	ppm	ppm	ppm	ppm
Detection Limit	1	0.5	5	1	2	1	1	2	0.5	0.5	1	0.1
Analysis Method	INAA	TD-ICP	INAA	INAA	PGNA A	FUS- ICP	FUS- ICP	TD-ICP	INAA	TD-ICP	INAA	INAA
GXR-1 Meas		30.8						1380		3.3		
GXR-1 Cert		31						1380		3.3		
NIST 694 Meas												
NIST 694 Cert												
DNC-1 Meas						107						
DNC-1 Cert						118						
GBW 07113 Meas						497	4					
GBW 07113 Cert						506	4					
GXR-4 Meas		3.1						14		< 0.5		
GXR-4 Cert		4						19		0.86		
SDC-1 Meas		< 0.5						< 2		< 0.5		
SDC-1 Cert		0.041						2.6		0.08		
SCO-1 Meas		< 0.5						< 2		< 0.5		
SCO-1 Cert		0.134						0.37		0.14		
GXR-6 Meas		0.5						< 2		0.8		
GXR-6 Cert		1.3						0.29		1		
LKSD-4 Meas												
LKSD-4 Cert												
SY-2 Meas					88							
SY-2 Cert					88							
SY-3 Meas					108							
SY-3 Cert					107							
W-2a Meas			< 5	2		178	< 1				25	43.4
W-2a Cert			0.046	1.2		182	1.3				23	43
SY-4 Meas						351	3					
SY-4 Cert						340	2.6					

Note: Meas – measured value
 Cert – certified value

Table B-2. Continued.

Analyte Symbol	Au	Ag	Ag	As	B	Ba	Be	Bi	Br	Cd	Ce	Co
Unit Symbol	ppb	ppm	ppm	ppm	ppm	ppm	ppm	ppm	ppm	ppm	ppm	ppm
Detection Limit	1	0.5	5	1	2	1	1	2	0.5	0.5	1	0.1
Analysis Method	INAA	TD-ICP	INAA	INAA	PGNA A	FUS- ICP	FUS- ICP	TD-ICP	INAA	TD-ICP	INAA	INAA
BIR-1a Meas						4	< 1					
BIR-1a Cert						6	0.58					
ZW-C Meas												
ZW-C Cert												
SGR-1b Meas												
SGR-1b Cert												
DNC-1a Meas												
DNC-1a Cert												
OREAS 13b (4-Acid) Meas		0.8										
OREAS 13b (4-Acid) Cert		0.86										
NCS DC86303 Meas												
NCS DC86303 Cert												
NCS DC86304 Meas												
NCS DC86304 Cert												
NCS DC86314 Meas												
NCS DC86314 Cert												
BCR-2 Meas						692						
BCR-2 Cert						683						
Method Blank	< 1		< 5	< 1					< 0.5		< 1	< 0.1
Method Blank		< 0.5						< 2		< 0.5		
Method Blank		< 0.5						< 2		< 0.5		
Method Blank												
Method Blank					< 2							

Note: Meas – measured value
 Cert – certified value

Table B-2. Continued.

Analyte Symbol	Cr	Cs	Cu	Eu	Hf	Hg	Ir	La	Li	Lu	Mo	Nd
Unit Symbol	ppm	ppm	ppm	ppm	ppm	ppm	ppb	ppm	%	ppm	ppm	ppm
Detection Limit	0.5	0.2	1	0.05	0.2	1	1	0.05	0.01	0.01	2	1
Analysis Method	INAA	INAA	TD-ICP	INAA	INAA	INAA	INAA	INAA	FUS- Na ₂ O ₂	INAA	TD-ICP	INAA
GXR-1 Meas			1190								16	
GXR-1 Cert			1110								18	
NIST 694 Meas												
NIST 694 Cert												
DNC-1 Meas												
DNC-1 Cert												
GBW 07113 Meas												
GBW 07113 Cert												
GXR-4 Meas			6440						< 0.01		312	
GXR-4 Cert			6520						0.00111		310	
SDC-1 Meas			30								< 2	
SDC-1 Cert			30								0.25	
SCO-1 Meas			28								< 2	
SCO-1 Cert			28.7								1.37	
GXR-6 Meas			70								< 2	
GXR-6 Cert			66								2.4	
LKSD-4 Meas												
LKSD-4 Cert												
SY-2 Meas												
SY-2 Cert												
SY-3 Meas												
SY-3 Cert												
W-2a Meas	96.8	< 0.2		1.08	2.7			11	< 0.01	0.33		11
W-2a Cert	92	0.99		1	2.6			10	0.00096	0.33		13
SY-4 Meas												
SY-4 Cert												

Note: Meas – measured value
 Cert – certified value

Table B-2. Continued.

Analyte Symbol	Cr	Cs	Cu	Eu	Hf	Hg	Ir	La	Li	Lu	Mo	Nd
Unit Symbol	ppm	ppm	ppm	ppm	ppm	ppm	ppb	ppm	%	ppm	ppm	ppm
Detection Limit	0.5	0.2	1	0.05	0.2	1	1	0.05	0.01	0.01	2	1
Analysis Method	INAA	INAA	TD-ICP	INAA	INAA	INAA	INAA	INAA	FUS- Na2O2	INAA	TD-ICP	INAA
BIR-1a Meas												
BIR-1a Cert												
ZW-C Meas									1.16			
ZW-C Cert									1.13			
SGR-1b Meas												
SGR-1b Cert												
DNC-1a Meas			105									
DNC-1a Cert			100									
OREAS 13b (4-Acid) Meas			2240								7	
OREAS 13b (4-Acid) Cert			2300								9	
NCS DC86303 Meas									0.23			
NCS DC86303 Cert									0.21			
NCS DC86304 Meas									1.05			
NCS DC86304 Cert									1.06			
NCS DC86314 Meas									1.66			
NCS DC86314 Cert									1.81			
BCR-2 Meas												
BCR-2 Cert												
Method Blank	< 0.5	< 0.2		< 0.05	< 0.2	< 1	< 1	< 0.05		< 0.01		< 1
Method Blank			< 1								< 2	
Method Blank			< 1								< 2	
Method Blank									< 0.01			
Method Blank												

Note: Meas – measured value
 Cert – certified value

Table B-2. Continued.

Analyte Symbol	Ni	Pb	Rb	Sb	Sc	Se	Sm	Sr	Ta	Tb	Th	U
Unit Symbol	ppm	ppm										
Detection Limit	1	5	10	0.1	0.01	0.5	0.01	2	0.3	0.1	0.1	0.1
Analysis Method	TD-ICP	TD-ICP	INAA	INAA	INAA	INAA	INAA	FUS-ICP	INAA	INAA	INAA	INAA
GXR-1 Meas	44	741										
GXR-1 Cert	41	730										
NIST 694 Meas												
NIST 694 Cert												
DNC-1 Meas								145				
DNC-1 Cert								144				
GBW 07113 Meas								38				
GBW 07113 Cert								43				
GXR-4 Meas	41	42										
GXR-4 Cert	42	52										
SDC-1 Meas	36	24										
SDC-1 Cert	38	25										
SCO-1 Meas	29	27										
SCO-1 Cert	27	31										
GXR-6 Meas	28	94										
GXR-6 Cert	27	101										
LKSD-4 Meas												
LKSD-4 Cert												
SY-2 Meas												
SY-2 Cert												
SY-3 Meas												
SY-3 Cert												
W-2a Meas			20	0.8	36.4		3.33	196	< 0.3	0.7	2.4	0.7
W-2a Cert			21	0.79	36		3.3	190	0.5	0.63	2.4	0.53
SY-4 Meas								1211				
SY-4 Cert								1191				

Note: Meas – measured value
 Cert – certified value

Table B-2. Continued.

Analyte Symbol	Ni	Pb	Rb	Sb	Sc	Se	Sm	Sr	Ta	Tb	Th	U
Unit Symbol	ppm	ppm										
Detection Limit	1	5	10	0.1	0.01	0.5	0.01	2	0.3	0.1	0.1	0.1
Analysis Method	TD-ICP	TD-ICP	INAA	INAA	INAA	INAA	INAA	FUS-ICP	INAA	INAA	INAA	INAA
BIR-1a Meas								105				
BIR-1a Cert								110				
ZW-C Meas												
ZW-C Cert												
SGR-1b Meas												
SGR-1b Cert												
DNC-1a Meas	253											
DNC-1a Cert	247											
OREAS 13b (4-Acid) Meas	2200											
OREAS 13b (4-Acid) Cert	2247											
NCS DC86303 Meas												
NCS DC86303 Cert												
NCS DC86304 Meas												
NCS DC86304 Cert												
NCS DC86314 Meas												
NCS DC86314 Cert												
BCR-2 Meas								332				
BCR-2 Cert								346				
Method Blank			< 10	< 0.1	< 0.01	< 0.5	< 0.01		< 0.3	< 0.1	< 0.1	< 0.1
Method Blank	< 1	< 5										
Method Blank	< 1	< 5										
Method Blank												
Method Blank												

Note: Meas – measured value
 Cert – certified value

Table B-2. Continued.

Analyte Symbol	V	W	Y	Yb	Zn	Zn	Zr
Unit Symbol	ppm	ppm	ppm	ppm	ppm	ppm	ppm
Detection Limit	5	1	1	0.05	1	50	2
Analysis Method	FUS-ICP	INAA	FUS-ICP	INAA	TD-ICP	INAA	FUS-ICP
GXR-1 Meas					734		
GXR-1 Cert					760		
NIST 694 Meas	1688						
NIST 694 Cert	1740						
DNC-1 Meas	153		17				43
DNC-1 Cert	148		18				38
GBW 07113 Meas	< 5		45				394
GBW 07113 Cert	5		43				403
GXR-4 Meas					75		
GXR-4 Cert					73		
SDC-1 Meas					103		
SDC-1 Cert					103		
SCO-1 Meas					98		
SCO-1 Cert					103		
GXR-6 Meas					134		
GXR-6 Cert					118		
LKSD-4 Meas							
LKSD-4 Cert							
SY-2 Meas							
SY-2 Cert							
SY-3 Meas							
SY-3 Cert							
W-2a Meas	276	< 1	19	2.1		150	87
W-2a Cert	262	0.3	24	2.1		80	94
SY-4 Meas	< 5		117				537
SY-4 Cert	8		119				517

Note: Meas – measured value
 Cert – certified value

Table B-2. Continued.

Analyte Symbol	V	W	Y	Yb	Zn	Zn	Zr
Unit Symbol	ppm	ppm	ppm	ppm	ppm	ppm	ppm
Detection Limit	5	1	1	0.05	1	50	2
Analysis Method	FUS-ICP	INAA	FUS-ICP	INAA	TD-ICP	INAA	FUS-ICP
BIR-1a Meas	330		13				12
BIR-1a Cert	310		16				18
ZW-C Meas							
ZW-C Cert							
SGR-1b Meas							
SGR-1b Cert							
DNC-1a Meas					59		
DNC-1a Cert					70		
OREAS 13b (4-Acid) Meas					107		
OREAS 13b (4-Acid) Cert					133		
NCS DC86303 Meas							
NCS DC86303 Cert							
NCS DC86304 Meas							
NCS DC86304 Cert							
NCS DC86314 Meas							
NCS DC86314 Cert							
BCR-2 Meas	429		33				170
BCR-2 Cert	416		37				188
Method Blank		< 1		< 0.05		< 50	
Method Blank					< 1		
Method Blank					2		
Method Blank							
Method Blank							

Note: Meas – measured value
 Cert – certified value

